Title: Molecular mechanism of the ischemia-induced regulatory switch in mammalian complex I

Authors: Daniel N. Grba[1]†, John J. Wright[1]†, Zhan Yin[1,2], William Fisher[1] & Judy Hirst[1]*

Affiliations:

[1]Medical Research Council Mitochondrial Biology Unit, University of Cambridge; Keith Peters Building, Cambridge Biomedical Campus, Hills Road, Cambridge CB2 0XY, UK

[2]Current address: Department of Biochemistry, University of Cambridge; Tennis Court Road, Cambridge, CB2 1GA, UK

† These authors contributed equally

* Author for correspondence: jh480@cam.ac.uk

Abstract: Respiratory complex I is an efficient driver for oxidative phosphorylation in mammalian mitochondria but its uncontrolled catalysis under challenging conditions leads to oxidative stress and cellular damage. Ischemic conditions switch complex I from rapid, reversible catalysis into a dormant state that protects upon reoxygenation, but the molecular basis for the switch is unknown. We combine precise biochemical definition of complex I catalysis with high-resolution electron cryomicroscopy structures in the phospholipid bilayer of coupled vesicles to reveal the mechanism of the transition into the dormant state, modulated by membrane interactions. By implementing a versatile membrane system to unite structure and function, attributing catalytic and regulatory properties to specific structural states, we define how a conformational switch in complex I controls its physiological roles.

Main Text:

Respiratory complex I (NADH:ubiquinone oxidoreductase) (*1–3*), one of the largest membrane-bound enzymes in mammalian cells, powers ATP synthesis in mitochondria. Under physiologically favorable conditions, complex I captures the free energy from electron transfer from NADH to ubiquinone to drive protons across the mitochondrial inner membrane in an efficient energy-converting reaction. However, when forward catalysis is blocked the same efficient mechanisms run in reverse or along different routes, leading to reactive oxygen species production and cellular damage (*4*, *5*). Regulatory mechanisms that switch the enzyme off under unfavorable conditions therefore protect the cell (*6–8*). During ischemia, when lack of oxygen prevents catalysis, the 'deactive transition' converts complex I to a dormant state (*9–11*), minimizing oxidative damage when oxygen returns during reperfusion and catalysis resumes. Mammalian complex I therefore exists in different catalytic and regulatory states, either on or off the catalytic cycle, depending on the mitochondrial conditions. Single-particle electron cryomicroscopy (cryoEM) (*12*, *13*) has revolutionized our ability to determine high-resolution structures of complex I and its homologues from multiple species, and to isolate multiple distinct states from heterogeneous mixtures (*14–26*). However, structures observed for complex I in different states, without accompanying biochemical, biophysical or physiological data to support their assignments, have been interpreted as both catalytic and regulatory species, creating a wide variety of contradictory models (*14–16*, *19*, *20*, *27*) and leaving fundamental questions unanswered. To develop our understanding of complex I further it is crucial to integrate structural and functional information into a single coherent and robust picture.

Here, we present high-resolution structures of mammalian (*Bos taurus*, bovine) complex I, isolated from ischemic heart tissue then embedded into phospholipid vesicle membranes containing ubiquinone-10 (Fig. 1). In these complex I-containing proteoliposomes (CI-PLs) the enzyme can be characterized in detail and switched between different regulatory states to investigate the transitions. The catalytic capability of the CI-PLs can be demonstrated by adding a partner ubiquinol-10 oxidase (the alternative oxidase, AOX) to enable rapid and reversible catalysis (*28*) with rates that match the maximum rates observed in native membranes (Fig. 2A) (*29*). By using different combinations of partner enzymes, the system can be set to catalyze NADH-driven ATP synthesis or NAD^+ reduction by reverse electron transfer (RET), both mediated by a substantial proton-motive force (*30*, *31*). Here, we combine biochemical, biophysical and cryoEM data on CI-PLs (Fig. S1) to identify the structural states that occur in the deactive transition of mammalian complex I, underpinning its role in ischemia–reperfusion injury (*5–8*), and to determine the mechanisms of the transitions between them. Through the reconstitution of highly active CI into CI-PLs suitable for cryoEM, comprehensive biochemical definition of the enzyme states present, and advanced application of single-particle cryoEM methods, we establish a quality threshold for structure-focused studies of complex I catalysis and regulation.

Closed and open states in the membrane

CryoEM images of CI in CI-PLs, flash frozen onto graphene oxide grids, were collected and separated into distinct populations (Fig. 1). The first classification separated CI molecules embedded in the membrane with their large hydrophilic domain, which extends into the mitochondrial matrix in vivo, facing either out of the PL lumen (CI-out) or into the PL lumen (CI-in) (Fig. 1A–B). The proportion of CI-out is ~65%, determined by both cryoEM classification

encompassing the surrounding bilayer and by biochemical assays that rely on accessibility of the NADH-binding site (CI-out only, versus CI-total when the membrane is permeabilized) (Fig. 2B). In both orientations, density for the surrounding bilayer is clearly visible, curving away from the protein membrane domain (Fig. 1A), and allowing visualization of the complex in a typical 50 nm-diameter proteoliposome (Fig. 1B). The second classification separated both CI-out and CI-in into two major conformational states, which we term the 'closed' and 'open' states (*14*) (Fig. 1C). Further classifications indicated the closed conformation is structurally homogenous but separated the open state into two similar but distinct states termed open1 and open2. The three states (closed, open1 and open2) are related by rotation of the hydrophilic domain and 'heel' relative to the rest of the membrane domain (Fig. S2A–C). This rotation is apparent visually as opening and closing of the angle between the domains, changing the secondary domain interface between NDUFA10 (membrane domain) and NDUFA5 (hydrophilic domain) (Fig. S2D) (*14*, *32*, *33*). The highest quality map (CI-out-closed) refined to 2.5-Å resolution, and near-complete protein models were built to all six maps, together with ordered phospholipids and water molecules (Fig. 1D) (Tables S1–2, Figs. S3–6). The maps and models show how amphipathic helices at the base of the hydrophilic domain that anchor the complex to the membrane interface influence the membrane topology and how the packing of transmembrane helices (TMHs) in the membrane domain adjusts the complex to the curvature (Fig. S7). Otherwise, the maps and models for outward- and inward-facing states are essentially identical.

The homogenous closed structures determined in CI-PLs match well to equivalent closed structures determined previously in *n*-dodecyl β-D-maltoside (DDM) detergent micelles and phospholipid nanodiscs (*17*, *32*) but with observation of a new interdomain contact mediated by supernumerary subunit NDUFAB1 and a Zn^{2+} bound to ND4 (Fig. S8). However, the open structures differ markedly. The open1 (most closed-like open) state has not been observed previously, and open2 is shifted towards the closed end of the 'open spectrum' relative to the open state in DDM or nanodiscs. Having previously observed DDM molecules bound behind the ND5 C-terminal transverse helix (*25*) and inserted into the narrow ubiquinone-binding channel in the open state in nanodiscs (*17*), we have here switched the detergent used for purification to lauryl maltose neopentyl glycol (LMNG), which is equivalent to two DDM molecules joined together and expected to be too bulky to enter the channel (*15*). No detergent molecules are observed in any of our structures in proteoliposomes (see Fig. S6). However, the extreme-open 'slack' state observed previously in DDM and nanodiscs (*17*, *32*), which exhibits substantial disorder and disruption in key regions including subunit NDUFA11 and the C-terminus of ND5 and is also expected to be catalytically inactive (*17*, *34*), is absent from our CI-PLs formed from LMNG-purified CI, but present in an equivalent preparation of CI-PLs formed from DDM-purified CI (DDM-CI-PLs, Table S3, Figs. S9–11). Otherwise, the closed and open structures from the two detergents match well, showing the influence of the stabilizing PL membrane environment. We conclude that the slack state is a DDM-induced artefact. The importance of considering detergent effects was also highlighted in cryoEM analyses of complex I from the yeast *Chaetomium thermophilum* and the bacteria *Escherichia coli*, where purification in DDM or LMNG altered the distributions of states observed (*20*, *21*). In the first part of our analysis open1 and open2, which are shown below to be biochemically indistinguishable, will be treated as a single open state.

Assigning functions to structural states

Two competing models currently assign the closed and open states observed by cryoEM in samples of mammalian CI, which have all been isolated from ischemic tissue, to different frameworks. The first postulates they are an ensemble of resting states (*32*, *33*, *35*, *36*) caught undergoing the deactive transition, which began when oxygen was depleted and catalysis stopped (*9–11*). The second postulates they are an ensemble of catalytic intermediates (*14*, *20*) caught at different points on the catalytic cycle when turnover stopped. Further progress on understanding the mechanism and regulation of CI requires the correct model to be confirmed. The biochemical characteristics of the states involved in the deactive transition have long been established (*9–11*). The active (A) ready-to-go resting state can immediately begin forward (NADH:ubiquinone oxidoreduction) or reverse (RET) catalysis upon introduction of substrates so it displays linear (constant-rate) steady-state NADH oxidation. The active state is also insensitive to thiol-reactive reagents that derivatize Cys39^{ND3} on the TMH1–2^{ND3} loop adjacent to the ubiquinone-binding site (*37*, *38*). In contrast, the deactive (D) dormant resting state requires substrate-induced reactivation to catalyze in the forward direction, exhibiting an initial catalytic 'lag phase' during its reactivation, and is unable to start catalyzing in reverse (*9*, *31*), a feature that is considered protective against oxidative damage during reperfusion (*8*, *39*). In the deactive state Cys39^{ND3} is sensitive to derivatization, which prevents reactivation by locking the enzyme in an inactive state (*37*, *38*). The active state deactivates slowly and spontaneously at physiological temperatures (~38 ºC in bovine heart) in the absence of substrates for turnover (*9*).

In our 'as-prepared' CI-PLs, containing CI isolated directly from ischemic heart tissue, cryoEM classification determined that 35% of the molecules are closed (65% are open), with a slightly higher proportion closed in the outward-facing population (Figs. 1C and 2C). The cryoEM values were compared to data from three biochemical analyses for the active and deactive states. First, we used two methods that rely on Cys39^{ND3} only being accessible in the deactive state (*31*, *38*). In a standard approach, we treated the CI-PLs with a thiol-reactive reagent and used activity assays (which report only on CI-out, as only its NADH-binding site is accessible) to determine the proportion of inactivated enzyme. Three thiol-reactive reagents, *N*-ethyl maleimide (NEM), iodoacetamide (IAM), and 5,5′-dithiobis-(2-nitrobenzoic acid) (DTNB), all gave similar results (Fig. S12A). We also used a sequence of isotopic labelling and mass spectrometry to measure total (CI-out and CI-in combined) Cys39^{ND3} labelling directly (*40*) (Fig. S13). In both cases, the biochemical active/deactive proportions are equal to the cryoEM closed/open proportions (Fig. 2C), consistent with structure models that show Cys39^{ND3} occluded in the closed state, but exposed and solvent accessible in open states (Fig. 3A) (*14*, *32*, *33*, *35*, *41*). Second, we tested for the catalytic lag phase that is a well-established deactive feature, using alkaline conditions to prolong reactivation (*9*, *10*, *37*). We used DTNB to derivatize Cys39^{ND3} reversibly (the DTNB label can be removed with the disulfide-reducing agent dithiothreitol (DTT), Fig. S12B (*42*)) and a standard thermal deactivation of CI-PLs (37 ºC for 20 min without substrates, Fig. S12C) to deactivate all the enzyme (*31*, *35*). The deactivation treatment in vitro replicates the effects on CI of an extended period of tissue ischemia in vivo. The catalytic lag phase is only observed when substrates are supplied to the (underivatized) open enzyme, and catalysis is linear with no lag phase when only the closed enzyme is able to catalyze (Fig. 2D).

Deactivated CI-PLs (D-CI-PLs) show all the deactive biochemical characteristics, including full recovery of their catalytic activity following reactivation, and derivatization of Cys39^{ND3} determined by activity assays and mass spectrometry analyses (Fig. 2A–C and Figs. S12B–D). In

cryoEM analyses of D-CI-PLs all the CI molecules were in the open state (Table S4, Figs. S14–17). The open1 and open2 structures determined in D-CI-PLs were indistinguishable from those determined in as-prepared CI-PLs (Fig. S18) so the deactive enzyme generated by simulating ischemia in vitro is identical to that present (at lower levels) in as-prepared samples from ischemic tissue. Our results demonstrate that the cryoEM closed state is the ready-to-go active resting state, the cryoEM open states are the dormant, deactive resting states, and the distribution of states in as-prepared samples of CI from ischemic tissue (*43*) represents a snapshot of the resting enzyme undergoing the deactive transition in the absence of substrates .

The ubiquinone-10 binding site

Our CI-closed structures exhibit well-ordered density for ubiquinone-10, inserted fully into its active site with one of the ubiquinone carbonyls directly hydrogen bonded to Tyr108^{NDUFS2}, a proposed ligand and proton donor for ubiquinone reduction (*44*, *45*) (Fig. 3B). Focused classifications were unable to separate any substates, suggesting the site is saturated by a single ubiquinone-10 binding pose, consistent with free equilibration with the ~10 mM ubiquinone-10 in the PL bilayer (relative to K_M values of 0.5–1.5 mM for catalyzing CI-PLs (*30*, *31*, *46*)). Earlier deep-bound ubiquinone-10 structures, determined in either nanodiscs or detergent micelles, have exhibited lower occupancy levels and either been in a pre-reactive conformation lacking direct interaction with Tyr108^{NDUFS2} (*17*) or without sufficient resolution to model water molecules (*19*). Here, waters are observed around the ubiquinone headgroup, in a single hydrogen-bonding network that indirectly connects both proposed proton donors (His59^{NDUFS2} and Tyr108^{NDUFS2}) to both ubiquinone carbonyls (Fig. 3B). Otherwise, the local, detailed features (Fig. 3C, top and Table S5) and discrete networks of residues and water molecules in the E-channel and hydrophilic axis (Fig. S19) match previous closed-state mammalian structures (*17*, *25*). The tightly structured, closed ubiquinone-binding site at the hydrophilic–membrane domain interface likely determines this consistency.

In as-prepared and deactivated CI-PLs the open state was resolved into two states, open1 and open2, which differ in the status of loops at the ubiquinone-binding site and domain interface, but otherwise display all the established structural hallmarks of open, deactive states (Fig. 3C and Table S5) (*36*). In the hitherto-unknown open1 state, the TMH1–2^{ND3} loop is ordered in a closed-like conformation. At the deepest part of the ubiquinone-binding channel, the β1–β2^{NDUFS2} loop is disordered and the trigonal interaction (*22*, *25*) between Cys39^{ND3}, His55^{NDUFS2} and Tyr127^{ND1} has been lost. Importantly, while Cys39^{ND3} is solvent accessible and available for derivatization by thiol-labelling reagents, the ubiquinone-binding channel is sealed from the matrix (Fig. 3A, S20). Open1 thereby combines an open global conformation with a closed ubiquinone-binding site, breaking the previously described (*14*) correlation between the two features. Ubiquinone-10 is partially inserted into the lower section of the open1 channel, and the TMH5–6^{ND1} loop is ordered in a closed-like conformation. In contrast, in the open2 state both the TMH1–2^{ND3} and β1–β2^{NDUFS2} loops are disordered (Cys39^{ND3} remains accessible) and the ubiquinone-binding channel is open to the matrix (Fig. 3A). Although only a poorly defined density hinting at ubiquinone-10 is observed, the TMH5–6^{ND1} loop remains in its closed-like conformation albeit with increased disorder at residues 208–209. Local disorder is also observed nearby in the TMH3–4^{ND6} loop (residues 79–85) and NDUFA9 C-terminal domain (residues 325–332). The ordered status of the TMH5–6^{ND1} loop in both open1 and open2 in CI-PLs (and conserved in DDM-CI-PLs) is in

striking contrast to the extended disorder observed previously in open states in detergent micelles and nanodiscs (*14*, *17*, *32*, *33*, *35*, *36*) (Table S5). Finally, the presence of two distinct open states in CI-PLs raises the question of whether they are both canonically deactive: both states are sensitive to thiol-derivatizing reagents (Fig. S20), but because we cannot control their formation independently, we cannot confirm whether both or just one cause the open-state-dependent catalytic lag phase. Therefore, we exploited the fact that deactive CI is unable to catalyze RET and assessed the ability of our CI-PLs to catalyze RET in a co-reconstituted system (*31*) that uses F_1F_O ATP synthase to create a proton-motive force (Fig. S21). As-prepared CI-ATPase-PLs exhibited 35% of the maximum RET rate (achieved following a pre-reaction activation step), which matches the proportion found in the closed state by the NEM assay. Furthermore, no RET could be observed for deactivated CI-ATPase-PLs, which contain only the open1 and open2 states. Although we cannot exclude that the proton-motive force and/or reduction of the ubiquinone pool for RET change the balance between open1 and open2, or even promote the closure of open1, these results suggest strongly that open1 and open2 are both deactive states.

Structural basis for deactivation

The spontaneous but slow nature of the deactive transition indicates deactivation is an exergonic process with a high activation energy, but how the structural changes that occur define the energy landscape for the transition and confer these properties is not understood. Here, we show how the membrane environment influences the stabilities of the states and the transition between them. Comparing the membrane-bound closed and open states, the hydrophilic domain rotates about an axis projected on subunit ND1 through the membrane domain (Fig. 4A and Fig. S2A–B), with ND1 and surrounding supernumerary subunits as a pivot point. TMH2–8^{ND1}, supported underneath by NDUFA8, NDUFA1 and NDUFA13, bend on closing or extend on opening (Fig. 4A–B). The long, curved NDUFA13 helix bends or extends alongside, whereas NDUFA8 and NDUFA1 are fixed and appear to brace the pivoting of NDUFA13 at its helix-breaking Pro-72 residue. We propose TMH2–8^{ND1} extending and straightening provide the primary driving force for deactivation, with their bending and deformation back into closed, catalytically active states demanding energization. Opposing straightening of these loaded helical 'springs', interaction of the amphipathic NDUFA9 C-terminal domain with the lipid bilayer creates a counterbalance (Fig. 4C). In the closed state, an abundance of well-ordered NDUFA9-associated lipids embed and anchor it to the bilayer whereas, in open states, rotation of the hydrophilic domain lifts NDUFA9 away from the bilayer. On the opposite side of the domain, amphipathic helices on NDUFS8 and NDUFA12 are pushed into the bilayer in open states, creating an intrinsic stabilizing 'buoyancy'. Amphipathic helices in the hydrophilic-domain core subunits likely perform the same role in enzymes, such as *E. coli* complex I, which lack both NDUFA9 and the biochemical characteristics of mammalian-type active/deactive transitions, although they may adopt less altered resting states. Additional protein interactions stabilizing the mammalian closed state (*47*) include the greater buried NDUFA5/NDUFA10 interface (Fig. S2D) and the N-terminus of NDUFS2 that runs across the matrix surface of the membrane domain, where it is ordered in the closed state but disordered in open states.

Ubiquinone-10 fully inserted into its binding channel in the closed state stabilizes the β1–β2^{NDUFS2} loop that carries the essential His59 (*48*), as well as the closed position of Arg77^{NDUFS7}. Upon deactivation, Arg77^{NDUFS7} moves into the channel, blocking substrate entry. Excluding substrate

allows the β1–β2^{NDUFS2} loop to escape its closed conformation, encouraging His55^{NDUFS2} to break its trigonal interaction with Cys39^{ND3} and TMH4-Tyr127^{ND1} as the latter straightens (Fig. 4C). Asp71 on the β1–β2^{NDUFS2} loop retains its ion-pair interaction with TMH4-Arg134^{ND1} as the straightening ND1-TMHs drive rotation of the hydrophilic domain, generating the matrix-exposed Cys39^{ND3} cavity in open1. Further destabilization of the TMH1–2^{ND3} loop, which crosses the rotation interface, occurs on conversion to open2 (Fig. 3A and Fig. 4B–D). Both straightening of the ND1-TMHs and rotation-induced displacement of NDUFA9 destroy the closed-state packing site for TMH3-Phe68^{ND6}, and destabilize interactions between TMH3–4-loop-Tyr79^{ND6} and Tyr324–Arg325^{NDUFA9}, promoting the helical rotation of TMH3^{ND6} that generates the hallmark π-bulge of the open states (Figs. 3C and 4C–D). The π-bulge (with unfavorable dihedrals, decreased hydrogen bonding and decreased packing) has an intrinsic driving force to return to an α-helical conformation, aiding reactivation. Prolonged absence of the deep-bound substrate from the closed state thereby promotes the coordinated, exergonic opening transition of a network of interacting structural elements, which are otherwise finely counterbalanced to maintain the metastable closed states in which catalysis occurs. Returning deactive open states to catalysis is determined by the mitochondrial conditions as it requires energy input from NADH-driven ubiquinone-10 reduction: to refold and reform local elements and drive domain rotation; regenerate the strained, loaded helical springs in ND1; and re-anchor NDUFA9 to the lipid bilayer, re-poising the system for energy transduction (Fig. 4D).

Discussion

The closed resting state in CI-PLs contains ubiquinone-10 fully loaded into the catalytic site, reflecting its ready-to-go nature. We propose the open1 and open2 states that form during ischemia are deactive, dormant states that must be re-activated to return to catalysis, with their off-cycle status suggested by their inability to initiate reverse catalysis — the reaction that produces reactive oxidative species during reperfusion. Specifically, the open-state π bulge in ND6-TMH3 disengages the proton-pumping reactions in the membrane arm from the redox machinery (*49*), and energy input from repeated NADH oxidation events is needed to re-engage the two. Our assignment of the open conformations to the deactive, dormant states that form during ischemia is not consistent with a competing proposal that they are catalytic intermediates (*14*), which was based on the presence of heterogeneous open states in ovine complex I (including the artefactual slack state) prepared from ischemic heart tissue. The inability of slack-type states to reactivate (*34*) explains their presence in ice-cold samples of the ovine enzyme in the presence of substrates (*14*), alongside deactive open states that persist due to their slow and temperature-dependent reactivation. Consistent with our model, the closed state appeared on addition of substrates to all-open preparations of *E. coli* complex I (*20*), and slow closing may explain the delay in proton pumping observed for the *E. coli* enzyme after the onset of redox catalysis (*50*). Finally, our data confirm that purposeful deactivation (under conditions that simulate tissue ischemia) of mammalian CI-PLs merely converts the closed/active enzyme into the same open/deactive enzyme already there at lower levels, completing the deactivation process that began in the tissue. Our data are not consistent with the alternate 'deactive' structure created by heat-treating the ovine enzyme in detergent micelles and characterized by the tilting of TMH4^{ND6} (*14*), which was presented without substantive biochemical data to confirm its identity or ability to return to catalysis, and which exhibited considerable structural disorder and alteration reminiscent of the bovine slack state (*17*).

Although cryoEM analyses provide no evidence that complex I opens and closes during catalysis, the coordinated changes of the deactive transition may provide clues to its catalytic mechanism. The same local elements that change conformation together during deactivation may change individually during catalysis, but in a local and constrained fashion (*51*), without breaking open the ubiquinone-binding site (and thereby incurring the energy costs of de-solvation, refolding and resealing) or globally opening the enzyme. Open1, a globally open state with a sealed ubiquinone-binding site, is between the closed and open2 states on the opening spectrum, and we suggest it forms first during deactivation, is the dominant open state in vivo, and is an intermediate in reactivation of open2 formed when substrate entry begins to restructure the channel. Ubiquinone-10 binding is essential for reactivation, but substrate exchange for catalysis occurs within closed-only states. Our model is consistent with observations of quinone partly or fully inserted into the closed channel in mycobacterial complex I (*26*), and with molecular dynamics simulations that have illustrated its transit through the closed channel on physiologically relevant timescales (*52*, *53*). We thus disagree that it is necessary to form open2-like states for solvent-assisted substrate exchange during catalysis (*14*, *20*). The conflicting interpretations of structural data discussed here underline the need for robust functional analyses to be employed alongside structural analyses in membrane environments in future mechanistic studies, as enabled by our CI-PLs.

The methods we have developed for structure-focused studies of catalysis and regulation in respiratory complex I offer possibilities for mechanistically challenging systems that require membrane environments for their function and/or suffer from poor cryoEM particle distribution and orientation biases in their detergent-solubilized forms. CryoEM on proteoliposomes has already been demonstrated by Yao and coworkers (*54*), who reported a 3.8-Å resolution structure of the AcrB multidrug resistant transporter embedded in liposomes on graphene grids. Several ion channels have now also been determined in liposomes and separated into different states (*55*), and a 2.7-Å resolution structure of a high conductance Ca^{2+}-activated K^+ channel has recently been determined in native membrane vesicles (*56*). Here, we demonstrate high-resolution structures and discrete states for a non-symmetrical protein, using standard grid preparation methods. The native-like environment and ubiquinone-10 substrate provided in CI-PLs, combined with the exquisite biochemical control that the system allows, has allowed a sophisticated structural evaluation of the resting states of mammalian complex I and their functional and physiological relevance, highlighting options for therapeutic intervention (*6*, *7*). The CI-PLs system now provides opportunities to study the catalytic intermediates that are generated under catalyzing and energy-transducing conditions.

References and Notes

1. J. Hirst, Mitochondrial Complex I. *Annu. Rev. Biochem.* **82**, 551–575 (2013).
2. K. Fiedorczuk, L. A. Sazanov, Mammalian Mitochondrial Complex I Structure and Disease-Causing Mutations. *Trends Cell Biol.* **28**, 835–867 (2018).
3. K. Parey, C. Wirth, J. Vonck, V. Zickermann, Respiratory complex I — structure, mechanism and evolution. *Curr. Opin. Struct. Biol.* **63**, 1–9 (2020).
4. M. P. Murphy, How mitochondria produce reactive oxygen species. *Biochem. J.* **417**, 1–13 (2009).

5. E. T. Chouchani, V. R. Pell, A. M. James, L. M. Work, K. Saeb-Parsy, C. Frezza, T. Krieg, M. P. Murphy, A unifying mechanism for mitochondrial superoxide production during ischemia-reperfusion injury. *Cell Metab.* **23**, 254–263 (2016).

6. E. T. Chouchani, C. Methner, S. M. Nadtochiy, A. Logan, V. R. Pell, S. Ding, A. M. James, H. M. Cochemé, J. Reinhold, K. S. Lilley, L. Partridge, I. M. Fearnley, A. J. Robinson, R. C. Hartley, R. A. J. Smith, T. Krieg, P. S. Brookes, M. P. Murphy, Cardioprotection by S-nitrosation of a cysteine switch on mitochondrial complex I. *Nat. Med.* **19**, 753–759 (2013).

7. A. Galkin, S. Moncada, Modulation of the conformational state of mitochondrial complex I as a target for therapeutic intervention. *Interface Focus* **7**, 1–8 (2017).

8. Z. Yin, N. Burger, D. Kula-Alwar, D. Aksentijević, H. R. Bridges, H. A. Prag, D. N. Grba, C. Viscomi, A. M. James, A. Mottahedin, T. Krieg, M. P. Murphy, J. Hirst, Structural basis for a complex I mutation that blocks pathological ROS production. *Nat. Commun.* **12**, 707 (2021).

9. A. B. Kotlyar, A. D. Vinogradov, Slow active/inactive transition of the mitochondrial NADH-ubiquinone reductase. *Biochim. Biophys. Acta Bioenerg.* **1019**, 151–158 (1990).

10. M. Babot, A. Birch, P. Labarbuta, A. Galkin, Characterisation of the active/de-active transition of mitochondrial complex I. *Biochim. Biophys. Acta Bioenerg.* **1837**, 1083–1092 (2014).

11. S. Dröse, A. Stepanova, A. Galkin, Ischemic A/D transition of mitochondrial complex I and its role in ROS generation. *Biochim. Biophys. Acta Bioenerg.* **1857**, 946–957 (2016).

12. T. Nakane, A. Kotecha, A. Sente, G. McMullan, S. Masiulis, P. M. G. E. Brown, I. T. Grigoras, L. Malinauskaite, T. Malinauskas, J. Miehling, T. Uchański, L. Yu, D. Karia, E. V. Pechnikova, E. de Jong, J. Keizer, M. Bischoff, J. McCormack, P. Tiemeijer, S. W. Hardwick, D. Y. Chirgadze, G. Murshudov, A. R. Aricescu, S. H. W. Scheres, Single-particle cryo-EM at atomic resolution. *Nature* **587**, 152–156 (2020).

13. A. Punjani, D. J. Fleet, 3D variability analysis: Resolving continuous flexibility and discrete heterogeneity from single particle cryo-EM. *J Struct Biol* **213**, 107702 (2021).

14. D. Kampjut, L. A. Sazanov, The coupling mechanism of mammalian respiratory complex I. *Science* **370**, eabc4209 (2020).

15. K. Parey, J. Lasham, D. J. Mills, A. Djurabekova, O. Haapanen, E. G. Yoga, H. Xie, W. Kühlbrandt, V. Sharma, J. Vonck, V. Zickermann, High-resolution structure and dynamics of mitochondrial complex I—Insights into the proton pumping mechanism. *Sci. Adv.* **7**, eabj3221 (2021).

16. P. Kolata, R. G. Efremov, Structure of *Escherichia coli* respiratory complex I reconstituted into lipid nanodiscs reveals an uncoupled conformation. *Elife* **10**, 1–32 (2021).

17. I. Chung, J. J. Wright, H. R. Bridges, B. S. Ivanov, O. Biner, C. S. Pereira, G. M. Arantes, J. Hirst, Cryo-EM structures define ubiquinone-10 binding to mitochondrial complex I and conformational transitions accompanying Q-site occupancy. *Nat. Commun.* **13**, 2758 (2022).

18. L. Zhou, M. Maldonado, A. Padavannil, F. Guo, J. A. Letts, Structures of *Tetrahymena*'s respiratory chain reveal the diversity of eukaryotic core metabolism. *Science* **376**, 831–839 (2022).

19. J. Gu, T. Liu, R. Guo, L. Zhang, M. Yang, The coupling mechanism of mammalian mitochondrial complex I. *Nat. Struct. Mol. Biol.* **29**, 172–182 (2022).

20. V. Kravchuk, O. Petrova, D. Kampjut, A. Wojciechowska-Bason, Z. Breese, L. Sazanov, A universal coupling mechanism of respiratory complex I. *Nature* **609**, 808–814 (2022).

21. E. Laube, J. Meier-Credo, J. D. Langer, W. Kühlbrandt, Conformational changes in mitochondrial complex I of the thermophilic eukaryote *Chaetomium thermophilum*. *Sci. Adv.* **8**, 1–15 (2022).

22. A. N. A. Agip, I. Chung, A. Sanchez-Martinez, A. J. Whitworth, J. Hirst, Cryo-EM structures of mitochondrial respiratory complex I from *Drosophila melanogaster*. *Elife* **12**, 1–26 (2023).

23. A. Padavannil, A. Murari, S.-K. Rhooms, E. Owusu-Ansah, J. A. Letts, Resting mitochondrial complex I from *Drosophila melanogaster* adopts a helix-locked state. *Elife* **12**, 2022.11.01.514701 (2023).

24. N. Klusch, M. Dreimann, J. Senkler, N. Rugen, W. Kühlbrandt, H.-P. Braun, Cryo-EM structure of the respiratory I + III_2 supercomplex from *Arabidopsis thaliana* at 2 Å resolution. *Nat. Plants* **9**, 142–156 (2022).

25. D. N. Grba, I. Chung, H. R. Bridges, A. N. A. Agip, J. Hirst, Investigation of hydrated channels and proton pathways in a high-resolution cryo-EM structure of mammalian complex I. *Sci. Adv.* **9** (2023).

26. Y. Liang, A. Plourde, S. A. Bueler, J. Liu, P. Brzezinski, S. Vahidi, J. L. Rubinstein, Structure of mycobacterial respiratory complex I. *Proc. Natl. Acad. Sci. U.S.A.* **120**, 2017 (2023).

27. H. Kim, P. Saura, M. C. Pöverlein, A. P. Gamiz-Hernandez, V. R. I. Kaila, Quinone Catalysis Modulates Proton Transfer Reactions in the Membrane Domain of Respiratory Complex I. *J. Am. Chem. Soc.* **145**, 17075–17086 (2023).

28. A. J. Y. Jones, J. N. Blaza, H. R. Bridges, B. May, A. L. Moore, J. Hirst, A Self-Assembled Respiratory Chain that Catalyzes NADH Oxidation by Ubiquinone-10 Cycling between Complex I and the Alternative Oxidase. *Angew. Chem., Int. Ed.* **55**, 728–731 (2016).

29. K. R. Pryde, J. Hirst, Superoxide Is Produced by the Reduced Flavin in Mitochondrial Complex I. *J. Biol. Chem.* **286**, 18056–18065 (2011).

30. O. Biner, J. G. Fedor, Z. Yin, J. Hirst, Bottom-Up Construction of a Minimal System for Cellular Respiration and Energy Regeneration. *ACS Synth Biol* **9**, 1450–1459 (2020).

31. J. J. Wright, O. Biner, I. Chung, N. Burger, H. R. Bridges, J. Hirst, Reverse Electron Transfer by Respiratory Complex I Catalyzed in a Modular Proteoliposome System. *J. Am. Chem. Soc.* **144**, 6791–6801 (2022).

32. J. Zhu, K. R. Vinothkumar, J. Hirst, Structure of mammalian respiratory complex I. *Nature* **536**, 354–8 (2016).

33. A. N. A. Agip, J. N. Blaza, H. R. Bridges, C. Viscomi, S. Rawson, S. P. Muench, J. Hirst, Cryo-EM structures of complex I from mouse heart mitochondria in two biochemically defined states. *Nat. Struct. Mol. Biol.* **25**, 1–9 (2018).

34. A.-N. A. Agip, J. N. Blaza, J. G. Fedor, J. Hirst, Mammalian Respiratory Complex I Through the Lens of Cryo-EM. *Annu. Rev. Biophys.* **48**, 165–184 (2019).

35. J. N. Blaza, K. R. Vinothkumar, J. Hirst, Structure of the Deactive State of Mammalian Respiratory Complex I. *Structure* **26**, 312-319.e3 (2018).

36. I. Chung, D. N. Grba, J. J. Wright, J. Hirst, Making the leap from structure to mechanism: are the open states of mammalian complex I identified by cryoEM resting states or catalytic intermediates? *Curr. Opin. Struct. Biol.* **77**, 102447 (2022).

37. A. B. Kotlyar, V. D. Sled, A. D. Vinogradov, Effect of Ca^{2+} ions on the slow active/inactive transition of the mitochondrial NADH-ubiquinone reductase. *Biochim. Biophys. Acta Bioenerg.* **1098**, 144–150 (1992).

38. A. Galkin, B. Meyer, I. Wittig, M. Karas, H. Schägger, A. Vinogradov, U. Brandt, Identification of the mitochondrial ND3 subunit as a structural component involved in the active/deactive enzyme transition of respiratory complex I. *J. Biol. Chem.* **283**, 20907–20913 (2008).

39. E. T. Chouchani, V. R. Pell, E. Gaude, D. Aksentijević, S. Y. Sundier, E. L. Robb, A. Logan, S. M. Nadtochiy, E. N. J. Ord, A. C. Smith, F. Eyassu, R. Shirley, C. H. Hu, A. J. Dare, A. M. James, S. Rogatti, R. C. Hartley, S. Eaton, A. S. H. Costa, P. S. Brookes, S. M. Davidson, M. R. Duchen, K. Saeb-Parsy, M. J. Shattock, A. J. Robinson, L. M. Work, C. Frezza, T. Krieg, M. P. Murphy, Ischaemic accumulation of succinate controls reperfusion injury through mitochondrial ROS. *Nature* **515**, 431–435 (2014).

40. N. Burger, A. M. James, J. F. Mulvey, K. Hoogewijs, S. Ding, I. M. Fearnley, M. Loureiro-López, A. A. I. Norman, S. Arndt, A. Mottahedin, O. Sauchanka, R. C. Hartley, T. Krieg, M. P. Murphy, ND3 Cys39 in complex I is exposed during mitochondrial respiration. *Cell Chem. Biol.* **29**, 636-649.e14 (2022).

41. J. A. Letts, K. Fiedorczuk, G. Degliesposti, M. Skehel, L. A. Sazanov, Structures of Respiratory Supercomplex I+III_2 Reveal Functional and Conformational Crosstalk. *Mol. Cell* **75**, 1131-1146.e6 (2019).

42. I. S. Gostimskaya, G. Cecchini, A. D. Vinogradov, Topography and chemical reactivity of the active-inactive transition-sensitive SH-group in the mitochondrial NADH:ubiquinone oxidoreductase (Complex I). *Biochim. Biophys. Acta Bioenerg.* **1757**, 1155–1161 (2006).

43. N. Gorenkova, E. Robinson, D. J. Grieve, A. Galkin, Conformational Change of Mitochondrial Complex I Increases ROS Sensitivity During Ischemia. *Antioxid. Redox Signal* **19**, 1459–1468 (2013).

44. M. A. Tocilescu, U. Fendel, K. Zwicker, S. Dröse, S. Kerscher, U. Brandt, The role of a conserved tyrosine in the 49-kDa subunit of complex I for ubiquinone binding and reduction. *Biochim. Biophys. Acta Bioenerg.* **1797**, 625–632 (2010).

45. A. P. Gamiz-Hernandez, A. Jussupow, M. P. Johansson, V. R. I. Kaila, Terminal Electron–Proton Transfer Dynamics in the Quinone Reduction of Respiratory Complex I. *J. Am. Chem. Soc.* **139**, 16282–16288 (2017).

46. J. G. Fedor, A. J. Y. Jones, A. Di Luca, V. R. I. Kaila, J. Hirst, Correlating kinetic and structural data on ubiquinone binding and reduction by respiratory complex I. *Proc. Natl. Acad. Sci. U.S.A.* **114**, 12737–12742 (2017).

47. A. Di Luca, V. R. I. Kaila, Molecular strain in the active/deactive-transition modulates domain coupling in respiratory complex I. *Biochim. Biophys. Acta Bioenerg.* **1862**, 148382 (2021).

48. M. A. Tocilescu, U. Fendel, K. Zwicker, S. Kerscher, U. Brandt, Exploring the Ubiquinone Binding Cavity of Respiratory Complex I. *J. Biol. Chem.* **282**, 29514–29520 (2007).

49. M. Röpke, D. Riepl, P. Saura, A. Di Luca, M. E. Mühlbauer, A. Jussupow, A. P. Gamiz-Hernandez, V. R. I. Kaila, Deactivation blocks proton pathways in the mitochondrial complex I. *Proc. Natl. Acad. Sci. U.S.A.* **118**, e2019498118 (2021).

50. N. Belevich, C. von Ballmoos, M. Verkhovskaya, Activation of Proton Translocation by Respiratory Complex I. *Biochemistry* **56**, 5691–5697 (2017).

51. A. Cabrera-Orefice, E. G. Yoga, C. Wirth, K. Siegmund, K. Zwicker, S. Guerrero-Castillo, V. Zickermann, C. Hunte, U. Brandt, Locking loop movement in the ubiquinone pocket of complex I disengages the proton pumps. *Nat. Commun.* **9**, 4500 (2018).

52. J. Warnau, V. Sharma, A. P. Gamiz-Hernandez, A. Di Luca, O. Haapanen, I. Vattulainen, M. Wikström, G. Hummer, V. R. I. Kaila, Redox-coupled quinone dynamics in the respiratory complex I. *Proc. Natl. Acad. Sci. U.S.A.* **115**, E8413–E8420 (2018).

53. M. H. Teixeira, G. M. Arantes, Balanced internal hydration discriminates substrate binding to respiratory complex I. *Biochim. Biophys. Acta Bioenerg.* **1860**, 541–548 (2019).

54. X. Yao, X. Fan, N. Yan, Cryo-EM analysis of a membrane protein embedded in the liposome. *Proc. Natl. Acad. Sci. U.S.A.* **117**, 18497–18503 (2020).

55. V. S. Mandala, R. MacKinnon, Voltage-sensor movements in the Eag Kv channel under an applied electric field. *Proc. Natl. Acad. Sci. U.S.A.* **119**, 1–12 (2022).

56. X. Tao, C. Zhao, R. MacKinnon, Membrane protein isolation and structure determination in cell-derived membrane vesicles. *Proc. Natl. Acad. Sci. U.S.A.* **120**, 2017 (2023).

57. G. Daum, Lipids of mitochondria. *Biochim. Biophys. Acta* **822**, 1–42 (1985).

58. M. S. Sharpley, R. J. Shannon, F. Draghi, J. Hirst, Interactions between phospholipids and NADH:ubiquinone oxidoreductase (complex I) from bovine mitochondria. *Biochemistry* **45**, 241–8 (2006).

59. K. Naydenova, C. J. Russo, Measuring the effects of particle orientation to improve the efficiency of electron cryomicroscopy. *Nat. Commun.* **8**, 8–12 (2017).

60. D. Kimanius, L. Dong, G. Sharov, T. Nakane, S. H. W. Scheres, New tools for automated cryo-EM single-particle analysis in RELION-4.0. *Biochem. J.* **478**, 4169–4185 (2021).

61. A. Punjani, J. L. Rubinstein, D. J. Fleet, M. A. Brubaker, CryoSPARC: Algorithms for rapid unsupervised cryo-EM structure determination. *Nat. Methods* **14**, 290–296 (2017).

62. J. Zivanov, T. Nakane, S. H. W. Scheres, A Bayesian approach to beam-induced motion correction in cryo-EM single-particle analysis. *IUCrJ* **6**, 5–17 (2019).

63. S. Q. Zheng, E. Palovcak, J. P. Armache, K. A. Verba, Y. Cheng, D. A. Agard, MotionCor2: Anisotropic correction of beam-induced motion for improved cryo-electron microscopy. *Nat. Methods* **14**, 331–332 (2017).

64. A. Rohou, N. Grigorieff, CTFFIND4: Fast and accurate defocus estimation from electron micrographs. *J. Struct. Biol.* **192**, 216–221 (2015).

65. D. Tegunov, P. Cramer, Real-time cryo-electron microscopy data preprocessing with Warp. *Nat. Methods* **16**, 1146–1152 (2019).

66. T. Bepler, A. Morin, M. Rapp, J. Brasch, L. Shapiro, A. J. Noble, B. Berger, Positive-unlabeled convolutional neural networks for particle picking in cryo-electron micrographs. *Nat. Methods* **16**, 1153–1160 (2019).

67. D. Asarnow, E. Palovcak, Y. Cheng, asarnow/pyem: UCSF pyem v0.5. Zenodo (2019). https://doi.org/https://doi.org/10.5281/zenodo.3576630.

68. T. D. Goddard, C. C. Huang, E. C. Meng, E. F. Pettersen, G. S. Couch, J. H. Morris, T. E. Ferrin, UCSF ChimeraX: Meeting modern challenges in visualization and analysis. *Protein Sci.* **27**, 14–25 (2018).

69. P. B. Rosenthal, R. Henderson, Optimal determination of particle orientation, absolute hand, and contrast loss in single-particle electron cryomicroscopy. *J. Mol. Biol.* **333**, 721–745 (2003).

70. J. L. Vilas, J. Gómez-Blanco, P. Conesa, R. Melero, J. Miguel de la Rosa-Trevín, J. Otón, J. Cuenca, R. Marabini, J. M. Carazo, J. Vargas, C. O. S. Sorzano, MonoRes: Automatic and Accurate Estimation of Local Resolution for Electron Microscopy Maps. *Structure* **26**, 337-344.e4 (2018).

71. E. Ramírez-Aportela, J. L. Vilas, A. Glukhova, R. Melero, P. Conesa, M. Martínez, D. Maluenda, J. Mota, A. Jiménez, J. Vargas, R. Marabini, P. M. Sexton, J. M. Carazo, C. O. S. Sorzano, Automatic local resolution-based sharpening of cryo-EM maps. *Bioinformatics* **36**, 765–772 (2020).

72. J. M. de la Rosa-Trevín, A. Quintana, L. del Cano, A. Zaldívar, I. Foche, J. Gutiérrez, J. Gómez-Blanco, J. Burguet-Castell, J. Cuenca-Alba, V. Abrishami, J. Vargas, J. Otón, G. Sharov, J. L. Vilas, J. Navas, P. Conesa, M. Kazemi, R. Marabini, C. O. S. Sorzano, J. M. Carazo, Scipion: A software framework toward integration, reproducibility and validation in 3D electron microscopy. *J. Struct. Biol.* **195**, 93–99 (2016).

73. D. Liebschner, P. V. Afonine, M. L. Baker, G. Bunkoczi, V. B. Chen, T. I. Croll, B. Hintze, L. W. Hung, S. Jain, A. J. McCoy, N. W. Moriarty, R. D. Oeffner, B. K. Poon, M. G. Prisant, R. J. Read, J. S. Richardson, D. C. Richardson, M. D. Sammito, O. V. Sobolev, D. H. Stockwell, T. C. Terwilliger, A. G. Urzhumtsev, L. L. Videau, C. J. Williams, P. D. Adams, Macromolecular structure determination using X-rays, neutrons and electrons: Recent developments in Phenix. *Acta Crystallogr. Sect. D Struct. Biol.* **75**, 861–877 (2019).

74. Y. Z. Tan, P. R. Baldwin, J. H. Davis, J. R. Williamson, C. S. Potter, B. Carragher, D. Lyumkis, Addressing preferred specimen orientation in single-particle cryo-EM through tilting. *Nat. Methods* **14**, 793–796 (2017).

75. J. Hirst, J. Carroll, I. M. Fearnley, R. J. Shannon, J. E. Walker, The nuclear encoded subunits of complex I from bovine heart mitochondria. *Biochim. Biophys. Acta Bioenerg.* **1604**, 135–150 (2003).

76. I. M. Fearnley, M. Finel, J. M. Skehel, J. E. Walker, NADH:ubiquinone oxidoreductase from bovine heart mitochondria. cDNA sequences of the import precursors of the nuclear-encoded 39 kDa and 42 kDa subunits. *Biochem. J.* **278**, 821–829 (1991).

77. J. Carroll, I. M. Fearnley, R. J. Shannon, J. Hirst, J. E. Walker, Analysis of the subunit composition of complex I from bovine heart mitochondria. *Mol. Cell Proteomics* **2**, 117–26 (2003).

78. D. Molina-Granada, E. González-Vioque, M. G. Dibley, R. Cabrera-Pérez, A. Vallbona-Garcia, J. Torres-Torronteras, L. A. Sazanov, M. T. Ryan, Y. Cámara, R. Martí, Most mitochondrial dGTP is tightly bound to respiratory complex I through the NDUFA10 subunit. *Commun. Biol.* **5** (2022).

79. P. Emsley, B. Lohkamp, W. G. Scott, K. Cowtan, Features and development of Coot. *Acta Crystallogr. Sect. D Struct. Biol.* **66**, 486–501 (2010).

80. C. J. Williams, J. J. Headd, N. W. Moriarty, M. G. Prisant, L. L. Videau, L. N. Deis, V. Verma, D. A. Keedy, B. J. Hintze, V. B. Chen, S. Jain, S. M. Lewis, W. B. Arendall, J. Snoeyink, P. D. Adams, S. C. Lovell, J. S. Richardson, D. C. Richardson, MolProbity: More and better reference data for improved all-atom structure validation. *Protein Sci.* **27**, 293–315 (2018).

Acknowledgments: We thank D. Chirgadze and S. Hardwick (University of Cambridge CryoEM facility) for assistance with grid screening and data collections. CryoEM data for the deactivated datasets were recorded at the UK National Electron Bio-Imaging Centre at the Diamond Light Source, proposal BI22238-45, funded by the Wellcome Trust, MRC and BBSRC. D.N.G. thanks the *Becoming an 'independent' single particle data collector* training course hosted by the Astbury Biostructure Lab (University of Leeds), eBIC (Diamond light source), Scottish Centre for Macromolecular Imaging (University of Glasgow), Midlands Regional CryoEM Facility (University of Leicester) and Birkbeck college (University of London), funded by the Wellcome Trust and Medical Research Council (218785/Z/19/Z). We thank A. J. Raine, E. E. Marcus and A. J. Nelson (MRC MBU) for IT support and I. M. Fearnley, S. Ding and N. Burger (MRC MBU) for mass spectrometry analyses.

Funding: This work was supported by the Medical Research Council (MC_UU_00015/2 and MC_UU_00028/1 to J.H.).

Author contributions: D.N.G. performed all cryoEM analyses, data processing, model building and structure analysis. J.J.W. prepared CI-PLs and performed all biochemical analyses. Z.Y. optimized graphene oxide grid preparations with D.N.G. W.F. optimized CI purification in LMNG. D.N.G. and J.H. conceived the project with input from J.J.W. J.H. supervised the project, acquired the funding and wrote the first draft of the manuscript. D.N.G. and J.J.W. produced data visualizations and wrote the final manuscript with J.H.

Competing interests: The authors declare no competing interests.

Data and materials availability: The structural data accession codes for the as-prepared CI-PLs dataset are: PDB 8Q48 and EMD-18141 (CI-out-closed); PDB 8Q4A and EMD-18143 (CI-out-open1); PDB 8Q49 and EMD-18142 (CI-out-open2); PDB 8Q45 and EMD-18138 (CI-in-closed); PDB 8Q47 and EMD-18140 (CI-in-open1); PDB 8Q46 and EMD-18139 (CI-in-open2). The structural data accession codes for the DDM-CI-PLs dataset are: PDB 8Q0M and EMD-18055 (CI-out-closed); PDB 8Q0O and EMD-18057 (CI-out-open2); PDB 8Q0Q and EMD-18059 (CI-out-slack); PDB 8Q0A and EMD-18051 (CI-in-closed); PDB 8Q0F and EMD-18052 (CI-in-open2); PDB 8Q0J and EMD-18054 (CI-in-slack). The structural data accession codes for the deactivated CI-PLs datasets are: PDB 8Q25 and EMD-18069 (CI-out-open1); PDB 8Q1Y and EMD-18068 (CI-out-open2); PDB 8Q1U and EMD-18067 (CI-in-open1); PDB 8Q1P and EMD-18066 (CI-in-open2). The cryoEM raw images are available from EMPIAR with the access codes EMPIAR-11678 (as-prepared CI-PLs), EMPIAR-11638 (DDM-CI-PLs), EMPIAR-11637 (deactivated CI-PLs non-tilted) and EMPIAR-11636 (deactivated CI-PLs tilted).

Supplementary Materials

Materials and Methods

Figs. S1–S22

Tables S1–S5

References (*57–80*)

Movie S1

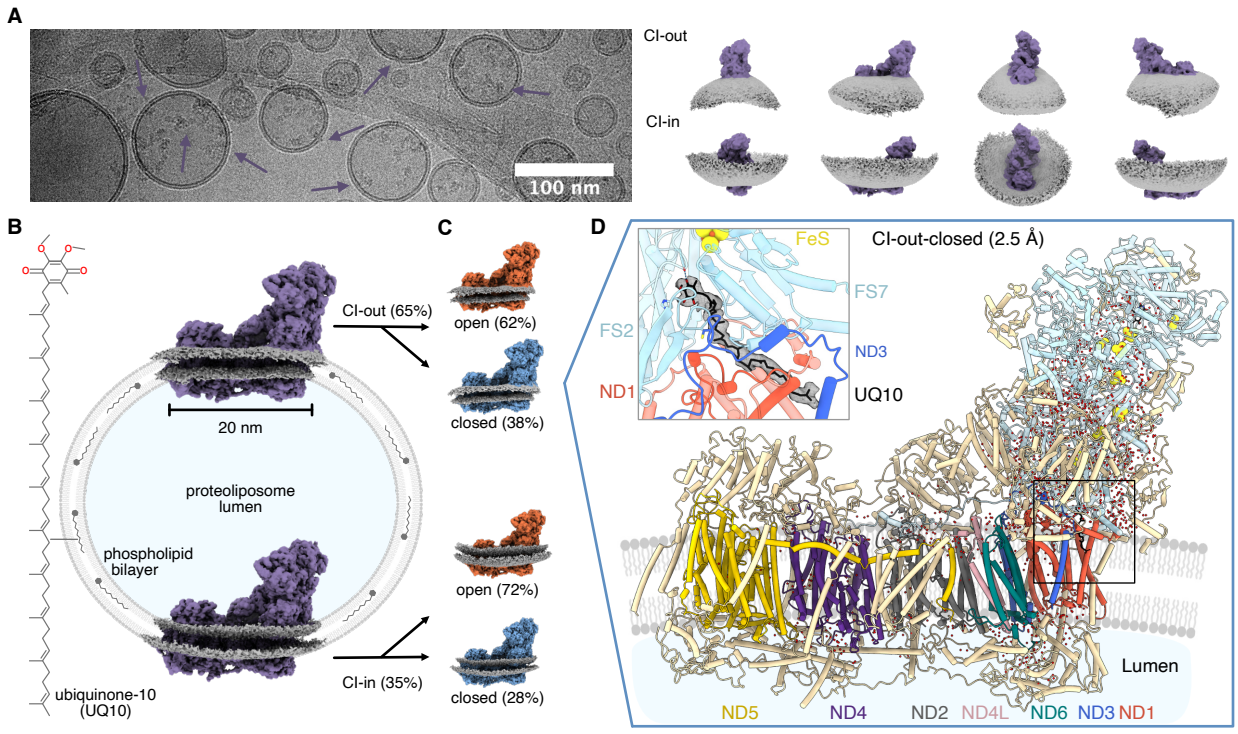


Fig. 1. Generation of high-resolution structures for complex I in proteoliposomes. A) An example micrograph (CI in CI-PLs marked with arrows) and 3D volumes for CI embedded in CI-PLs facing outwards (CI-out) and inwards (CI-in). **B)** Visualization of CI reconstituted into CI-PLs containing ubiquinone-10. The cryoEM density for the lipid bilayer (grey) around the enzyme (purple) was clipped and extrapolated to display a typical 50 nm-diameter liposome. **C)** CI-out and CI-in were classified into open (orange) and closed (blue) states and processed to generate high-resolution maps. **D)** The model for CI-out-closed (2.5 Å resolution) is shown with water molecules (spheres) and ubiquinone-10 in the substrate-binding site (inset). Conserved core subunits are in light blue (hydrophilic domain) or labelled in color (membrane domain) and supernumerary subunits are in wheat.

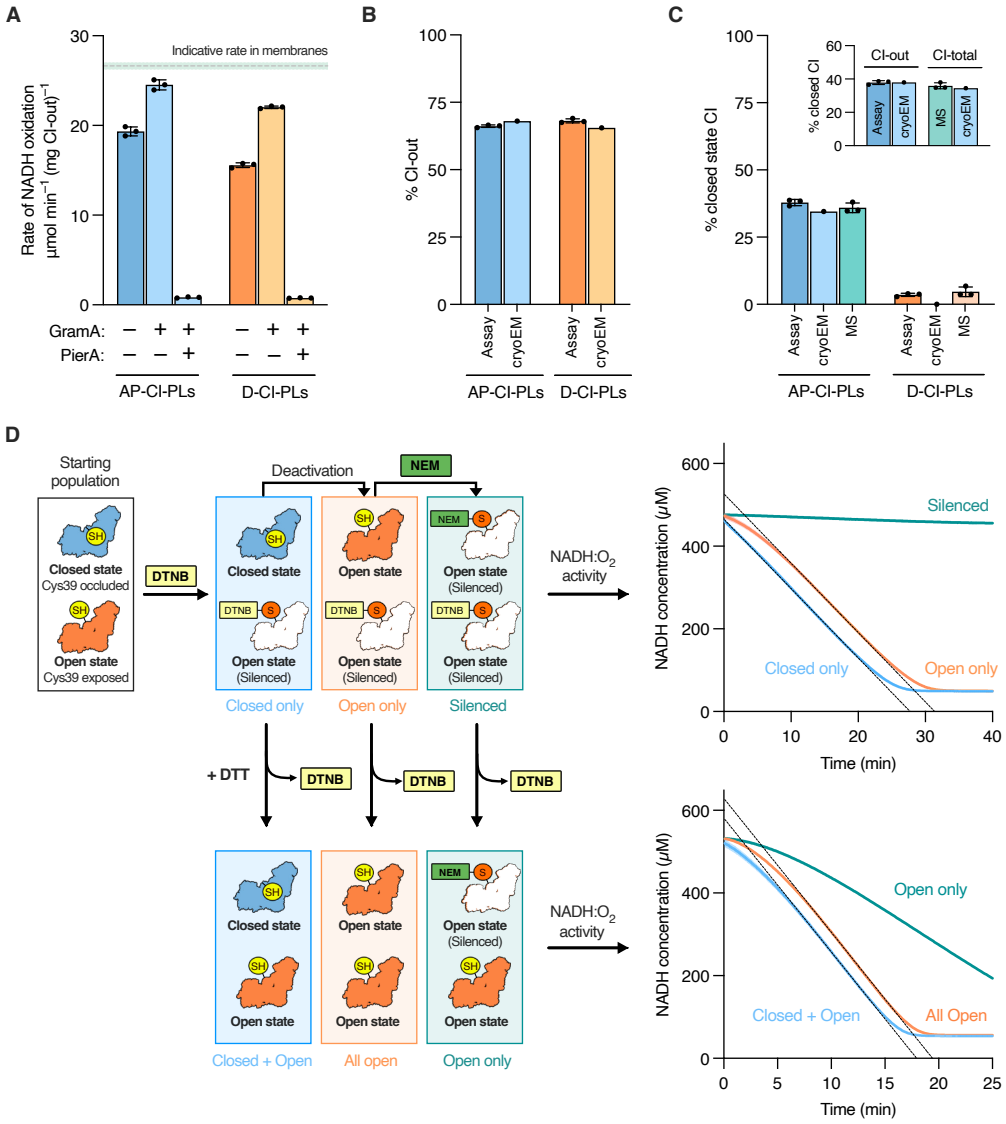


Fig. 2. Biochemical properties of complex I in CI-PLs. A) Maximal rates of NADH oxidation in as-prepared (AP) and deactivated (D) cryoEM samples of CI-PLs measured with the ubiquinol oxidase AOX in the assay buffer (n = 3, ± S.D.). Gramicidin A (GramA, to dissipate Δp, 0.5 µg mL^{-1}) and piericidin A (PierA, to inhibit CI, 1 µM) were added as indicated. An indicative value for CI in mitochondrial membranes is provided for comparison, calculated on the basis that 10% of the protein present is CI (*29*). **B)** Proportion of outward facing complex I (CI-out) in cryoEM samples determined using the NADH:APAD$^+$ oxidoreduction assay (n = 3, ± S.D.) and from the cryoEM particle distribution. **C)** The proportion of closed-state complex I in AP-CI-PLs and D-CI-PLs determined using the sensitivity of the rate of NADH:O_2 oxidoreduction to NEM (assay, n = 3, ± S.D.), by cryoEM particle classification (cryoEM), and by mass spectrometry following isotopic IAM labelling (MS, n = 3, ± S.D.). MS data are from three independent CI-PL reconstitutions. The inset figure presents the values from the cryoEM data for AP-CI-PLs to match the CI-out and CI-total populations determined by biochemical assays and MS, respectively. **D)** The lag phase observed in complex I activity assays is due to the presence of open states (n = 3, ± S.D.). A mixture of closed and open states in an as-prepared sample of CI-PLs was (i) treated with

DTNB (only the closed population catalyzes, linear catalysis), (ii) deactivated (the previously closed population opens, and catalyzes with a lag phase), then (iii) labelled with NEM (both populations are inactive). Each sample was then treated with DTT to remove the DTNB. In (i) both states catalyze and the mixture displays a lag phase; in (ii) the whole population is open and the lag phase is increased; in (iii) only the open population catalyzes, with a lag phase. See Fig. S12G for a matching experiment using only IAM.

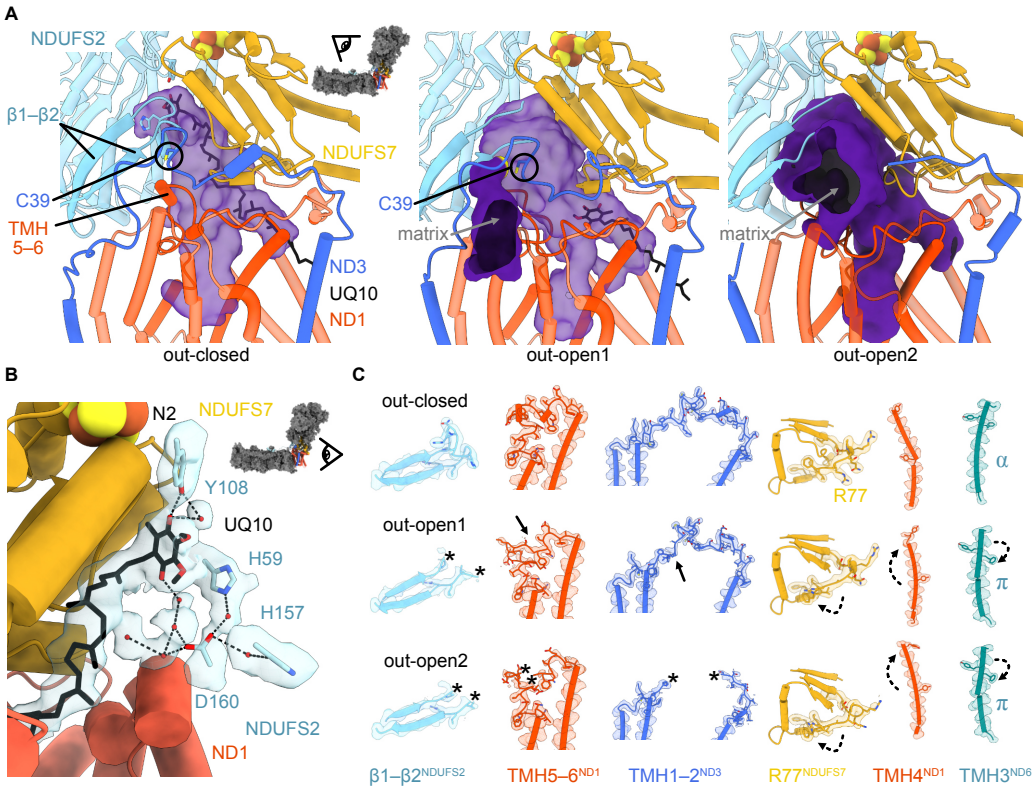


Fig. 3. Local features of complex I structures in CI-PLs. A) The ubiquinone-10 (UQ10)-binding channel in the closed, open1 and open2 states. Closed: the UQ10-binding channel (purple, semi-transparent surface) is sealed from the matrix, UQ10 is fully inserted, and C39^{ND3} is buried from the matrix. Open1: the UQ10-binding channel is sealed from the matrix, UQ10 is partly inserted, and C39^{ND3} is exposed to the matrix (purple, solid surface with yellow indicating the contribution from Cys39^{ND3}). Open2: the UQ10-binding channel is exposed to the matrix (purple, solid surface), no bound UQ10 is present, and C39^{ND3} is exposed to the matrix. **B)** The bound UQ10 in the CI-out-closed state reveals a two hydrogen-bonding networks of water molecules (red spheres) that complete its connection to the proposed ligands (His59^{NDUFS2} and Tyr108^{NDUFS2}) for protonation upon reduction by the terminal iron–sulfur cluster N2. The semi-transparent surface shows the cryoEM density (2 Å distance, threshold value 0.03). **C**) The local elements that correlate with closed and open structural states: β1–β2^{NDUFS2} loop (ordered in closed, progressively less ordered in open1 and open2); TMH5–6^{ND1} loop (ordered in closed with short α-helical features, ordered in open1 but with helical definition lost, minor disorder in open2), TMH2–3^{ND3} loop (ordered in closed, ordered and shifted in open1, disordered in open2), R77^{NDUFS7}, TMH3^{ND6} α helix/π bulge and TMH4^{ND1}. CryoEM density is shown (at thresholds 0.1, 0.1, 0.09, 0.1, 0.1, 0.09, left to right) with residues of interest shown as sticks. Solid and dashed arrows indicate localized disorder and movement, respectively, relative to the closed state. Asterisks indicate peptides not observed due to disordering. See also Fig. S20 and Table S5.

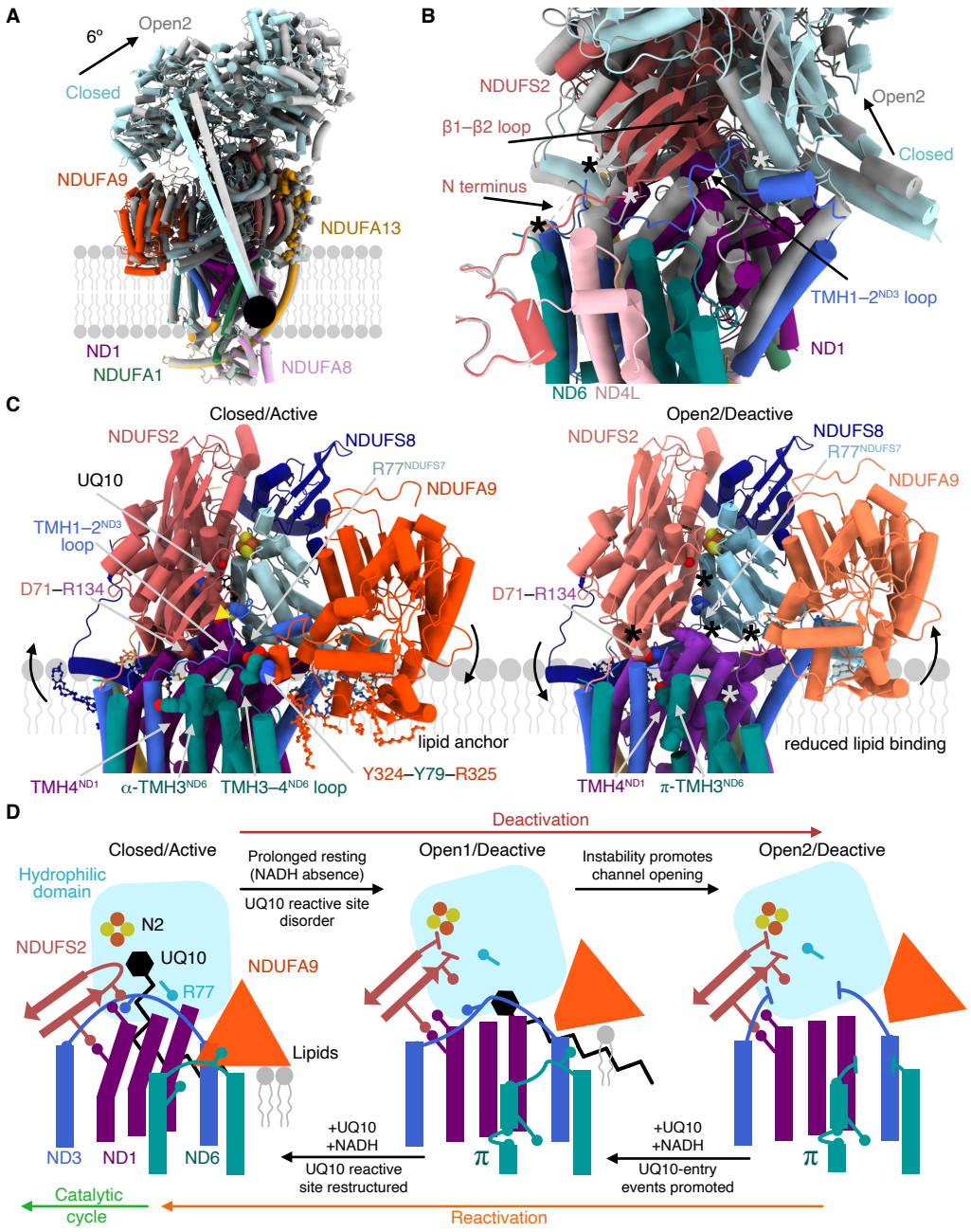


Fig. 4. Structural transition between the active/closed and deactive/open resting states. A) Global comparison of the closed/active (color) and open2/deactive (grey) structures superpositioned on their membrane domains showing relevant supernumerary subunits from behind the hydrophilic–membrane domain interface. The axis of rotation is marked as a black circle, with the rotation (6º) planes shown. The N-terminus of NDUFA13 extends up the hydrophilic domain and is shown as spheres. **B)** The same alignment as in **A** viewed from the front and focused on the hydrophilic-membrane domain interface to show the movement of the ND1 TMHs relative to ND6 and the rotation of the hydrophilic domain. Asterisks indicate disorder in the open2/deactive model, where coordinated colors link the missing residues. **C)** The same superpositioned models as in **B** with labelled subunits of interest only and the closed/active and open2/deactive states shown side by side. Lipids and ubiquinone-10 (UQ10) are shown in ball and stick representation; iron–sulfur cluster N2 and key residues are shown as spheres. The residues

of the trigonal junction are indicated by the yellow triangle. Asterisks indicate regions of loop disorder. **D)** Schematic overview of the structural elements involved in the deactivation and reactivation transitions between the closed/active and open2/deactive states corresponding to panel **C**. Circles on sticks indicate stabilizing residue interactions, such as the trigonal junction of H55^{NDUFS2}, Y127^{ND1} and C39^{ND3}; R77^{NDUFS7}, the ion pair R134^{ND1}–D71^{NDUFS2}; and the packing interactions Y324^{NDUFA9}–Y79^{ND6}–R325^{NDUFA9} and F68$^{TMH3\text{-}ND6}$ with ND1. See also Movie S1.

Supplementary Materials for

Molecular mechanism of the ischemia-induced regulatory switch in mammalian complex I

Daniel N. Grba, John J. Wright, Zhan Yin, William Fisher & Judy Hirst

Corresponding author: jh480@cam.ac.uk

The PDF file includes:

Materials and Methods
Figs. S1 to S22
Tables S1 to S5
References

Other Supplementary Materials for this manuscript include the following:

Movie S1

Materials and Methods

Purification of *Bos taurus* complex I

Mitochondrial membranes were prepared from ischemic bovine heart tissue and complex I was purified in *n*-dodecyl-β-D-maltopyranoside (DDM) according to an established procedure (*46*). This protocol was then adapted for purification in lauryl maltose neopentyl glycol (LMNG, Anatrace) as follows. Membranes (175 mg protein) were treated with one cOmplete protease inhibitor tablet (Roche) then solubilized on ice at 4.5 mg mL^{-1} by the stepwise addition of lauryl maltose neopentyl glycol (LMNG, Anatrace) from a 5% stock solution to a final concentration of 1.5%, followed by a further 20 min incubation, and centrifugation (8,500 × g, 15 min, 4 ºC). The supernatant was filtered through a 0.22 µm syringe-tip filter then loaded onto three 5 mL Q-Sepharose HP columns (Cytiva) connected in series and pre-equilibrated with Buffer A (20 mM Tris-HCl (pH 7.5 @ RT), 2 mM EDTA, 10% (v/v) ethylene glycol, 0.15% (w/v) LMNG, 0.02% asolectin (total soy lipid extract, Avanti Polar Lipids), and 0.02% 3-[(3-cholamidopropyl)-dimethylammonio]-1-propanesulfonate (CHAPS)). The columns were washed with 23% Buffer B (Buffer A + 1 M NaCl) then Buffer B was increased to 38% to elute complex I. Complex I-containing fractions were collected, pooled and concentrated using an Amicon Ultra-15 (100 MWCO) then injected onto a Superose 6 Increase column (Cytiva) pre-equilibrated with Buffer C (20 mM Tris-HCl (pH 7.5 @ RT), 150 mM NaCl, 10% (v/v) glycerol, 0.0375% LMNG). Complex I-containing fractions were concentrated as before and flash frozen in liquid N_2. The complex I concentration (according to the bicinchoninic acid (BCA) assay) and the NADH:$APAD^+$ and NADH:DQ oxidoreductase rates were determined.

Purification of AOX

AOX from *Trypanosoma brucei brucei* was expressed recombinantly in *E. coli* and purified from membranes by solubilization with octyl-glucoside and Twin-Strep tag affinity chromatography as described previously (*46*).

Preparation of CI-PLs

Complex I proteoliposomes (CI-PLs) for cryoEM and biochemical analyses were prepared using a method adapted from a previously published procedure (*31*). A synthetic phospholipid mixture optimized for maximal complex I activity in well-coupled liposomes (*28*, *30*) was used, consisting of the predominant phospholipids of the mammalian inner mitochondrial membrane (*57*) that are known to be important for complex I function (*58*). 1,2-dioleoyl-*sn*-glycero-3-phosphocholine (DOPC), 1,2-dioleoyl-*sn*-glycero-3-phosphoethanolamine (DOPE), and 18:1 cardiolipin (CDL) were mixed at an 8:1:1 weight ratio as a 25 mg mL^{-1} chloroform stock solution. 10 mg of lipids were transferred to a glass tube and supplemented with 100 nmol Q_{10}, then the chloroform was

removed using a gentle stream of N_2. The resulting lipid film was transferred to a desiccator and stored under vacuum for at least 1 hr. Lipids were rehydrated with frequent vortexing over 30 min following addition of 1 mL of Proteoliposome Buffer (10 mM MOPS-KOH (pH 7.5, 20 ºC), 50 mM KCl). Small unilamellar vesicles (< 50 nm) were formed by sonication on ice using a Q700 probe sonicator (qSonica) equipped with a 1.6 mm microtip (60% amplitude, 2.5 min, cycle of 15 s on, 30 s off) then partially solubilized by addition of 0.5% (w/v) sodium cholate and incubated on ice for 10 min. Complex I was added at a 50:1 (w/w) lipid to protein ratio and the mixture incubated on ice for a further 20 min before the detergent was removed using a PD10 desalting column (Cytiva) pre-equilibrated with Proteoliposome Buffer. CI-PLs were collected by ultracentrifugation (210,000 × g, 1 hr, 4 ºC) and resuspended in the same buffer. The resulting sample was centrifuged using a benchtop centrifuge at maximum speed (16,000 × g, 10 min, 4 ºC) to remove any larger particles, and kept on ice or at 4 °C before use. All the data reported for CI-PLs are from a single preparation of complex I to ensure that data from the different experiments can be compared. Biochemical and mass spectrometry analyses on multiple samples of CI-PLs, from different reconstitutions of the same complex I, were confirmed to be consistent.

Complex I activity assays

All activity assays were performed spectrophotometrically using a SpectraMax plus 348 or SpectraMax ABS Plus 96-well plate reader (Molecular Devices). Unless otherwise stated, assays were conducted at 32 ºC. Complex I concentration in CI-PLs was determined using the NADH:$APAD^+$ oxidoreduction reaction ($\varepsilon_{400–450}$ = 3.16 mM^{-1} cm^{-1}): the standard rate was determined for LMNG-solubilized complex I (0.5 µg mL^{-1}) in Proteoliposome Buffer with 100 µM NADH, 500 µM $APAD^+$, 500 nM piericidin A and 0.2% (w/v) DDM (*30*, *46*), and compared to the rate from CI-PLs under the same conditions but without DDM, giving the concentration of CI-out. The total CI concentration, and CI-out proportion, were determined by comparing the NADH:$APAD^+$ rates in the presence and absence of 15 µg mL^{-1} alamethicin (AlaM) to permeabilize the proteoliposomes to the substrates. NADH:O_2 oxidoreduction rates were measured as the rates of NADH oxidation ($\varepsilon_{340–380}$ = 4.81 mM^{-1} cm^{-1}) in the presence of excess AOX to continually re-oxidize the ubiquinone-10 (*28*). CI-PLs (0.5 µg mL^{-1} CI-out) were diluted into Proteoliposome Buffer and treated with 5–10 µg mL^{-1} AOX, then catalysis was initiated by addition of 200 µM NADH. The uncoupled rate ($\Delta p = 0$) was calculated following addition of 0.5 µg mL^{-1} gramicidin A (GramA). Proton pumping was assessed using the fluorescence of 9-amino-6-chloro-2-methoxyacridine (ACMA) (λ_{ex} = 410 nm, λ_{em} = 480 nm) in a RF-5301PC spectrofluorometer (Shimadzu) at 32 ºC. CI-PLs (1.0 µg mL^{-1} CI-out) were incubated in Proteoliposome Buffer with 10 µg mL^{-1} AOX, 0.5 µM ACMA and 0.1 µM valinomycin and 500 µM NADH added to initiate catalysis. When required, 1 µM piericidin A was added to inhibit complex I, or 15 µg mL^{-1} alamethicin for uncoupling. Reverse electron transfer assays were performed with proteoliposomes co-

reconstituted with both CI and *E. coli* F_1F_O ATP synthase (3 ATPase per CI) (Fig. S21), supplemented with glycerol 3-phosphate dehydrogenase (GlpD, *E. coli*) as described previously (*31*) but with minor modifications to the activation procedure. To activate complex I, CI-PLs (10 μg mL^{-1} CI-out) were incubated at 32 ºC with 60 μM NADH for 2 min, then 60 μM decylubiquinone (DQ) was added. After a further 1 min incubation, during which the NADH and DQ were consumed, RET was initiated by addition of ATP, *rac*-glycerol 3-phosphate and NAD^+ as described previously (*31*). Assay data are reported ± SD with individual data points shown.

Derivatization of Cys39 to determine active/deactive (A/D) ratios

To assess the proportion of A-state complex I relative to the total amount of (A+D) enzyme present, CI-PLs were diluted to 200 μg mL^{-1} and treated with either 1 mM *N*-ethylmaleimide (NEM, from a 100 mM stock in 25% DMSO), 20 mM iodoacetamide (IAM, from a 200 or 500 mM stock in Proteoliposome Buffer) or 0.2 mM 5,5′-dithiobis-(2-nitrobenzoic acid) (DTNB, from a 10 mM stock in DMSO). Samples were incubated on ice for 20 min (NEM), 30 min (IAM) or 1 hour (DTNB) to ensure complete labelling. Where indicated, complex I was deactivated by incubating the CI-PLs at 37 ºC for 20 min. NADH:O_2 oxidoreductase activities were determined as above, following dilution of the sample into Proteoliposome Buffer and addition of AOX and NADH. To determine the A/D states in bovine mitochondrial membranes, 2 mg mL^{-1} membranes were treated with 1 mM NEM, then the activity determined in 10 mM Tris-HCl (pH 7.5), 250 mM sucrose using 5 μg mL^{-1} membranes, 3 μM cytochrome c (equine heart) and 15 μg mL^{-1} AlaM, with catalysis initiated by 200 μM NADH. Membranes were deactivated using the same procedure as for CI-PLs.

For differential isotopic labelling for mass spectrometry studies, freshly prepared samples of CI-PLs (typically 250–350 μg mL^{-1} CI-out) were split into three: an 'as-prepared' (AP-CI) sample, a deactivated (D-CI) sample that was incubated at 37 ºC for 20 min, and a vehicle control AP-CI sample that was treated identically to the AP-CI sample but without inclusion of the labels. The samples were incubated with 30 mM H-IAM (Label 1, L1) on ice for 30 min, then the H-IAM was then quenched by addition of 50 mM GSH for 10 min on ice, and the CI-PLs were collected by centrifugation (210,000 × g, 1 hr, 4 ºC). The CI-PL pellets were each washed with 3 × 1 mL of Proteoliposome Buffer then resuspended in 100 μL of the same buffer. The NADH:O_2 oxidoreductase activity of each sample was measured, and a portion of each sample was incubated with 20 mM L-IAM and its activity checked again to confirm completion of labelling. All the samples were then incubated at 37 ºC for 20 min to deactivate them, and their activities checked to ensure that no denaturation had occurred and that no L1 had been carried over. They were then treated with 50 mM L-IAM (Label 2, L2) and incubated for 30 min on ice before the activities were recorded again. The samples were then divided into 20 μL aliquots, and each aliquot diluted

with either 100 µL MS control buffer (20 mM Tris-HCl (pH 8.0), 200 mM NaCl, 100 mM GSH) for method 1, or 100 µL MS denaturation buffer (20 mM Tris-HCl (pH 8.0), 200 mM NaCl, 8 M urea, 50 mM L-IAM) for method 2, and stored at –20 ºC. A schematic diagram of the labelling procedure is given in Fig. S13A.

For trypsin cleavage, labelled samples (20 µL) were precipitated with 20 volumes of ice-cold ethanol overnight. The pellets were then digested with 20 µL of a 1:100 dilution of trypsin in 50 mM NH_4HCO_3. 2 µL of each sample were then added to 10 µL of 0.1% TFA, 3% CH_3CN, and injected for LC/MS/MS analysis. The peptide mixtures were fractionated by liquid chromatography using a gradient of 5–40% CH_3CN, 0.1% (v/v) TFA, at a flow rate of 300 nL min^{-1} over 84 min using an Acclaim PepMap nanoViper C18 reverse-phase column in an EASY-nLC system (Thermo Scientific). Fractions were transferred to a Q-Exactive Plus Orbitrap mass spectrometer (Thermo Scientific, UK) where data were acquired for a peptide mass range of 400 to 1600 m/z for precursor ions and the ten most abundant precursor ions were fragmented by high-energy collisional dissociation (HCD) in N_2. For protein identification, the fragment patterns were compared to the UniProt database in Mascot. Relative quantitation was achieved by comparing the peak heights of extracted ion chromatograms (XICs) using Xcalibur.

To investigate catalytic lag phases, as-prepared CI-PLs (150 µL, 0.5 mg mL^{-1} CI-out) were incubated with 0.2 mM DTNB on ice for 1 h, then the sample was diluted with 1 mL Proteoliposome Buffer and centrifuged (210,000 × g, 1 h, 4 ºC). The pellet was washed with 3 × 1 mL of Proteoliposome Buffer then the DTNB-labelled CI-PLs were resuspended in 100 µL of the same buffer. Half the labelled sample was deactivated (20 min incubation, 37 ºC), and half the deactivated sample was treated with NEM (1 mM, 30 min incubation on ice). Assays to assess the lag phase were performed at room temperature in a buffer at elevated pH (10 mM Tris-HCl (pH 8.8), 50 mM KCl) to slow down reactivation and amplify the lag phase (*10*, *37*). CI-PLs containing 2.5 µg mL^{-1} CI-out were combined with 10 µg mL^{-1} AOX and incubated at room temperature for 5 min prior to addition of NADH. Where indicated, 1 mM DTT was present to remove the DTNB label. For IAM labelled experiments, reconstituted CI-PLs were split into two, with one half of the sample incubated with L-IAM (30 mM, 30 min incubation on ice) and the other half of the sample untreated. In both cases, the lag phases were compared between as-prepared and deactivated CI-PL samples, with no DTT treatment.

CryoEM grid preparation, screening and imaging

CryoEM grids [Cu grids (1.2/1.3 Quantifoil) for DDM datasets or UltrAuFoil® gold grids (0.6/1, Quantifoil) for LMNG datasets] were washed in chloroform and then ethanol, dried in air then glow discharged (20 mA, 90 s, 0.1 Bar). A solution of graphene oxide (GO, 2 mg mL^{-1}, Sigma-Aldrich) was bath sonicated to evenly resuspend

it, then 3 µL were applied to the top side of a grid and manually blotted. Grids were washed three times with water then dried at 100 ºC for 30 min. Prior to sample addition, the GO-coated grids were glow discharged (10 mA, 15 s, 0.1 Bar). CI-PLs (2.5 µL per grid, 200 µg mL^{-1} CI-total) were applied to each grid in an FEI Vitrobot Mark IV (Thermo Fisher Scientific) at 4 °C and 95% relative humidity. The sample was incubated on the grids for 30 s then blotted for 2 s under a force setting of 0, and frozen by plunging into liquid ethane. Grids were screened at the cryoEM facility at the Department of Biochemistry, University of Cambridge, using either a Talos Arctica or a Titan Krios microscope (Thermo Fischer Scientific). Grids with good GO coverage, even ice and even proteoliposomes distribution were taken forward.

As-prepared CI-PLs data collection

High-resolution images (27,014 micrographs) were recorded using a Titan Krios microscope at the cryoEM facility at the Department of Biochemistry, University of Cambridge. The instrument was operated at 300 kV using a Gatan K3 detector in super-resolution electron counting mode at a nominal sampling rate of 1.066 Å pix^{-1}. Non-gain normalized images were acquired with AFIS and a post-column imaging energy filter (Gatan BioContinuum) set to a slit width of 20 eV at a dose rate of ~17 electrons $Å^{-2}$ s^{-1}. The sample was exposed to a total dose of ~45 electrons $Å^{-2}$ in a 2.67 s exposure over 40 fractions. The C2 and objective lens apertures were set to 70 and 100 µm, respectively. Images were collected with a defocus range of −0.9 to −2.3 µm.

DDM-CI-PLs data collection

High-resolution images (5,568 micrographs) were recorded using a Titan Krios microscope at the cryoEM facility at the Department of Biochemistry, University of Cambridge. The instrument was operated at 300 kV using a Gatan K3 detector in super-resolution electron counting mode at a nominal sampling rate of 1.43 Å pix^{-1}. Non-gain normalized images were acquired with AFIS and a post-column imaging energy filter (Gatan BioContinuum) set to a slit width of 20 eV at a dose rate of ~12 electrons $Å^{-2}$ s^{-1}. The sample was exposed to a total dose of ~40 electrons $Å^{-2}$ in a 3.40 s exposure over 40 fractions. The C2 and objective lens apertures were set to 70 and 100 µm, respectively. Images were collected with a defocus range of −1.0 to −3.0 µm.

Deactivated CI-PLs data collection

High-resolution images (6,692 micrographs) were recorded using a Titan Krios microscope at the UK National electron Bio-Imaging Centre (eBIC), at the Diamond Light Source. The instrument was operated at 300 kV using a Gatan K3 detector in super-resolution electron counting mode at a nominal sampling rate of 1.072 Å pix^{-1}. Non-gain normalized images were acquired with AFIS and a post-column imaging energy filter (Gatan BioContinuum)

set to a slit width of 20 eV at a dose rate of ~ 10.5 electrons $Å^{-2}$ s^{-1}. The sample was exposed to a total dose of ~40 electrons $Å^{-2}$ in a 3.8 s exposure over 40 individual movie frames. The C2 and objective lens apertures were set to 50 and 100 µm, respectively. Images were collected with a defocus range of −0.9 to −2.3 µm. An additional dataset (4,550 micrographs) was collected on the same grid with the same conditions except the stage was tilted by 20º, as suggested by cryoEF to improve orientation distribution (*59*), and AFIS was disabled. The session reference is BI22238-45.

As-prepared CI-PLs data processing

CryoEM data processing was carried out in RELION-4.0-beta (*60*) and cryoSPARC v3.3.2 (*61*). Beam-induced motion in the gain-normalized movie frames was corrected using RELION's implementation (*62*) of MotionCor2 (*63*) and per-micrograph contrast transfer function (CTF) parameters determined from the non-dose-weighted motion-corrected movie sums with CTFFIND-4.1 (*64*). Initial particles (1,320,319) from on-the-fly processing using Warp (*65*) were imported into cryoSPARC and a 200,000 subset subjected to multiple rounds of 2D classification to generate an initial subset of particles (16,358) to train the Topaz picker (*66*) in RELION. This picker was then used on all motion-corrected, CTF-corrected micrographs and the above process was iterated until ~6 million particles were picked. Briefly, the initial subset from 2D classification (16,358) was used to train a picker that resulted in 767,618 particles being picked on all micrographs. All particles were extracted (3.75 Å pix^{-1}) and imported into cryoSPARC, split randomly and subjected to 2D classification. Protein-like particles were selected from membrane-only classes and put into *ab initio* reconstruction. The complex I-like particles (213,953) were homogeneously refined, re-extracted (1.066 Å pix^{-1}) and homogeneously refined again to generate a 3D reference for subsequent heterogeneous classification. This yielded a complex I class (178,958) that was used to train Topaz on all micrographs. The resulting particles (5,725,932) were then extracted with a figure-of-merit value of –5. These particles were processed in cryoSPARC and RELION using a mixture of 2D and 3D classification and heterogenous and *ab initio* refinements facilitated here and throughout with the *csparc2star* python script of the UCSF pyem code repository (*67*). Additional *ab initio* models for complex I, membrane-only and junk/noise classes were generated throughout the process as protein particles were taken forward and used to update the 3D references in the various refinement jobs. A final set of 315,578 particles was then used to train Topaz before 5,688,318 particles (figure-of-merit value –4) were extracted (3.75 Å pix^{-1}) and subjected to the final classification scheme (Fig. S3). Here, the large number of particles were split into random groups and processed in parallel, before being combined at checkmark points. Heterogeneous refinement with six classes separated CI-in and CI-out using low-resolution membrane curvature features. Like classes were combined in homogeneous refinement before being randomly split again and applying iterative heterogenous

refinements to remove junk particles and better sort the classes. The particles were re-extracted (1.066 Å pix^{-1}, box size of 450 pixels) and randomly split within their respective CI-in/CI-out branches before protein-masked 3D classification (10 classes) and homogeneous refinement were run on each class. Masks were auto-generated in cryoSPARC. Classes were inspected for global conformation and grouped, with heterogenous jobs used to clean out junk particles. The particles were polished and CTF refined in RELION to facilitate subsequent classification in cryoSPARC using 3D classification and heterogeneous and homogeneous refinement. The classification resulted in two major protein states for each of CI-in and CI-out, open and closed, which were combined and re-extracted in RELION. Individual classes underwent particle polishing and CTF refinement prior to 3D classification in RELION over six classes, with angular sampling decreased gradually (7.5°/3.7°/1.8°) and local searches enabled, to help remove any remaining junk particles and verify the global classification from cryoSPARC through comparison of 3D refinement volumes of each class. We attempted a focus-revert-classify method (align on the hydrophilic arm prior to classification without alignment on the membrane arm (*41*) to separate out the protein further); however, we found the result tended to identify different membrane curvatures resulting from different liposome sizes. Instead, we implemented a focus-subtract-classify-revert method. Briefly, particles were focus refined on the hydrophilic domain (to remove membrane arm-imposed limitation on alignment of the hydrophilic arm), revealing the conformational distribution at the membrane interface. The hydrophilic mask used was generated in RELION (with a binarization threshold of 0.02, an extension of three pixels and a soft cosine edge of 10 pixels) using a rigid-body fitted previous bovine complex I model (PDB 7QSL) and a volume generated using the *molmap* command in ChimeraX (*68*), with the low-pass filter set to 15 Å. Particles were subtracted using a mask that covers the membrane–hydrophilic interface region, before being classified without alignments over eight classes using a regularization parameter (T) = 100. The mask of the region was generated as for the hydrophilic mask, except it was low-pass filtered to 10 Å, with a binarization threshold of 0.1 and an extension of five pixels. Output classes were reverted to their non-subtracted states and 3D refined before being combined (CI-in/out closed, open1 or open2) where appropriate for a final consensus 3D refinement. We found this method particularly effective for complex I; for example, it was able to separate out a sub-class of ~10,000 particles from ~335,000 particles that was overlooked by all other 3D classification methods performed above. Furthermore, it enabled us to separate the open state into discrete populations, termed open1 and open2, which differ in their protein loop ordering at the membrane–hydrophilic interface. Finally, in order to test occupancy and substrate poses of the ubiquinone-binding site, we used a particle-subtracted region focusing on ND1/3/6 and NDUFS2/FS7 that compose the channel as the input volume to classification (*17*). Masks were generated using the ubiquinone-10 in the built models (fully bound and midway bound, see below), low-pass filtered to 5 Å or 8 Å with a soft cosine edge added. A series of classifications were performed in RELION with

class numbers ranging from 2 to 5, and the regularization parameter (*T*) titrated to 10, 25, 50 and 100. In each case, for the reverted and refined particles, no alternate poses or occupancy could be resolved. In cryoSPARC, we used 2–10 classes in PCA mode, with the target resolution increased to a range of 2.5–3 Å. We also attempted 3D variability analysis (3DVA) in cryoSPARC with a range of eigenvector covariance modes from 3 to 6, filtered to a resolution of 3 Å. In both cryoSPARC cases, outputs gave classes that contained ubiquinone-10 signal in the same region as the consensus input.

Global resolution was estimated in RELION from the Fourier Shell Correlation (FSC) between two independent, unfiltered half-maps, according to the FSC = 0.143 criterion (*69*), and post-processed using an automatically estimated B factor: CI-out-closed = 2.5 Å, CI-out-open1 = 2.6 Å, CI-out-open2 = 2.6 Å, CI-in-closed = 2.7 Å, CI-in-open1 = 2.9 Å, CI-in-open2 = 2.6 Å. Local resolution was estimated in RELION. Maps were locally sharpened using MonoRes (*70*) and LocalDeblur (*71*) in the Scipion v1.2.1 package (*72*) to aid in model building and model refinements. Map visualization was improved with *map_to_structure_factors* using Phenix v1.20.1-4487 (*73*). Directional resolution anisotropy was calculated using 3DFSC Program Suite v3.0 (*74*). Orientation distributions were plotted in Mollweide projections using Matplotlib and Python.

DDM-CI-PLs data processing

CryoEM data processing was carried out in RELION-4.0-beta and cryoSPARC v3.3.2. Beam-induced motion in the gain-normalized movie frames was corrected using RELION's implementation of MotionCor2 and per-micrograph contrast transfer function (CTF) parameters determined from the non-dose-weighted motion-corrected movie sums with CTFFIND-4.1. An initial manual picking was performed to train the Topaz picker in RELION and the picker was improved through the selection of good particles using 2D classification and heterogenous refinement, until a Topaz picker was trained on 410,047 particles. The picker was then used with a figure-of-merit value of −5 to select 2,313,863 particles for extraction at 4 Å pix^{-1}. The particles were split into random subsets and processed in parallel, before being combined at checkpoints. Iterative heterogeneous refinement with six classes separated the CI-in and CI-out from junk classes via low-resolution membrane curvature features. Like classes were combined and homogenously refined before re-extraction (1.43 Å pix^{-1}, box size of 360 pixels). A two-class 3D classification was performed in cryoSPARC with a mask around the membrane to better split CI-out and CI-in. Protein-masked 3D classification (six classes) was performed within the CI-out/CI-in branches. Masks were auto-generated in cryoSPARC. Classes were inspected for their global conformation and grouped, with heterogenous jobs used to clean out junk particles. A three-class 3D classification was then performed that provided three distinct classes: closed, open2 and slack. Particles were polished and CTF

refined in RELION prior to 3D classification in RELION over six classes, with angular sampling decreased gradually (7.5°/3.7°/1.8°) and local searches enabled, to help remove any remaining junk particles and verify the global classification from cryoSPARC by comparing the 3D refinement volumes of each class. The resulting non-junk classes were refined and subjected to the focus-subtract-classify-revert classification scheme outlined above, split over four classes. The output classes were refined and grouped, resulting in six classes: CI-out/in-closed, CI-out/in-open2, CI-out/in-slack. Global resolution was estimated in RELION from the FSC between two independent, unfiltered half-maps, according to the FSC = 0.143 criterion, and post-processed using an automatically estimated B factor and to a calibrated pixel size of 1.35 Å pix^{-1}, based on map–model correlation values with previous complex I models: CI-out-closed = 3.1 Å, CI-out-open2 = 3.1 Å, CI-out-slack = 3.6 Å, CI-in-closed = 3.1 Å, CI-in-open2 = 3.1 Å, CI-in-slack = 3.8 Å. Local resolution was estimated in RELION. Directional resolution anisotropy was calculated using 3DFSC Program Suite v3.0. Orientation distributions were plotted in Mollweide projections using Matplotlib and Python.

Deactivated CI-PLs data processing

CryoEM data processing was carried out in RELION-4.0-beta and cryoSPARC v3.3.2 for both tilted and non-tilted datasets. In both cases, beam-induced motion in the gain-normalized movie frames was corrected using RELION's implementation of MotionCor2 and per-micrograph contrast transfer function (CTF) parameters determined from the non-dose-weighted motion-corrected movie sums with CTFFIND-4.1. For both datasets, a previously trained Topaz picking model, using 801,932 particles from the as-prepared CI-PLs dataset, was implemented for particle picking in RELION. For the non-tilted dataset, a Topaz figure-of-merit value of 0 was used to select 878,425 particles for extraction at 2.86 Å pix^{-1}. The particles were split into random subsets and processed in parallel, before being combined at checkpoints. Iterative heterogeneous refinement with six classes separated CI-in and CI-out via low-resolution membrane curvature features. Like classes were combined in homogeneous refinement, before being randomly split again and iterative heterogenous refinements were applied to remove junk particles and better sort the classes. Like classes were combined in homogeneous refinement before a final non-junk, six-class heterogeneous refinement was performed. Like classes were combined in homogeneous refinement and re-extracted (1.072 Å pix^{-1}, box size of 480 pixels). Masks were auto-generated in cryoSPARC. No further processing in cryoSPARC was performed as no states other than the open state were detected in 3D classification or heterogeneous refinements (unlike in the as-prepared dataset). CI-in and CI-out particles were refined, polished and CTF refined in RELION prior to 3D classification in RELION over six classes, with angular sampling decreased gradually (7.5°/3.7°/1.8°) and local searches enabled, to help remove any remaining junk particles. Good classes were refined and subjected to a focus refinement and classification on

the subtracted hydrophilic–membrane interface; however, this only removed minor junk classes. At this point the CI-out-open (87,008) and CI-in-open (40,990) particles were combined with equivalent particles from the tilted dataset.

For the 20°-tilted dataset, a Topaz figure-of-merit value of −2 was used to select 932,186 particles for extraction at 2.86 Å pix^{-1}. The particles were split into random subsets and processed in parallel, before being combined at checkpoints. Iterative heterogeneous refinement with 12 classes separated CI-in and CI-out via low-resolution membrane curvature features; the class number was higher as the low resolution of the tilted data made separating empty membrane/junk particles more difficult. Good protein classes were combined in homogeneous refinement before being randomly split again and iterative heterogenous refinements were applied to remove junk particles and better sort the classes. Good protein classes were combined in homogeneous refinement and re-extracted (1.072 Å pix^{-1}, box size of 480 pixels) to improve resolution prior to a three-class heterogeneous refinement to separate CI-out and CI-in. They each underwent homogeneous refinement and a three-class heterogeneous refinement again before a final homogeneous refinement clean-up step. Masks were auto-generated in cryoSPARC. As in the non-tilted dataset, no further processing in cryoSPARC was performed as no states other than the open state were detected in 3D classification and heterogeneous refinements. CI-in and CI-out particles were refined, polished and CTF refined twice in RELION prior to 3D classification in RELION over six classes, with angular sampling decreased gradually (7.5°/3.7°/1.8°) and local searches enabled, to help remove any remaining junk particles. In each case a single good class was output then refined. At this point the CI-out-open (58,376) and CI-in-open (39,423) particles were combined with equivalent particles from the non-tilted dataset.

Prior to combining, the tilted and non-tilted particles were assessed for adjustments in orientation sampling (Fig. S22). The tilt applied appeared to have reduced the orientation preference observed in the consensus refinement, but at the cost of higher resolution. The high sphericity in the non-tilted dataset refinements suggests the orientation distribution does not suffer from a problematic lack of views. The combined CI-out-open (145,384) and CI-in-open (80,413) states underwent 3D refinement in RELION prior to 3D classification over six classes, with angular sampling decreased gradually (7.5°/3.7°/1.8°) and local searches enabled. The resulting non-junk classes [CI-out-open (142,957) and CI-in-open (76,4214)] were refined and subjected to the focus-subtract-classify-revert classification scheme outlined above, split over eight classes. The output classes were refined and grouped, with four classes resulting: CI-out/in-open1 and CI-out/in-open2. No closed states were observed. Global resolution was estimated in RELION from the FSC between two independent, unfiltered half-maps, according to the FSC = 0.143 criterion, and post-processed using an automatically estimated B factor: CI-out-

open1 = 2.8 Å, CI-out-open2 = 2.6 Å, CI-in-open1 = 3.3 Å, CI-in-open2 = 2.9 Å. Local resolution was estimated in RELION. Maps were locally sharpened using MonoRes and LocalDeblur in the Scipion v1.2.1 package to aid in model building and model refinements. Map visualization was improved with *map_to_structure_factors* using Phenix v1.20.1-4487. Directional resolution anisotropy was calculated using 3DFSC Program Suite v3.0. Orientation distributions were plotted in Mollweide projections using Matplotlib and Python.

As-prepared CI-PLs model building and refinement

Previous bovine complex I models were used as starting points for models for the closed (PDB 7QSK) and open (PDB 7QSN) states of complex I in the as-prepared CI-PLs (*17*). They include the polymorphisms at NDUFA10-255 and NDUFS2-129 modelled as Lys and Arg (*17*, *75–77*), respectively. Sequence numbering for subunits NDUFA6 and NDUFA13 were adjusted to account for N-terminal processing (*75*). The cofactor in NDUFA10 was updated to Mg^{2+}-bound 2'-deoxyguanosine 5'-triphosphate (*78*). The models were rigid-body fit into respective consensus maps using ChimeraX v1.16.1 (*68*). Subunits were all-atom refined and per-chain refined using Coot v0.9.8.1 (*79*), guided by locally sharpened maps. ND5-locally refined maps, with a mask around respective CI-in/out-open/closed ND5 regions, were generated to improve the local resolution (Fig. S7C) and used to build the variably curved ND5 regions with more confidence for each state, before reverting back to consensus maps. The ND5 region had relatively poor local resolution due to variation in liposome curvature. Previous lipid/detergent/ubiquinone-binding site molecules were removed from the starting PDB models, before lipids and substrate ubiquinone-10 molecules were built into the maps for each state. Added molecules were clipped where the cryoEM density was absent due to flexibility. Protein chains were inspected, and residues removed where cryoEM density was lacking, or added, including N-terminal acetylation, where densities not previously observed were present (see Table S2 for details of the CI-out-closed model). Water molecules were built into the CI-out-closed, CI-out-open1 and CI-out-open2 models, which have the highest resolution for each state. Water molecules were added using the *Find Waters* command in Coot with default values and a root-mean-square deviation value starting at 6.0. Subsequent additions were performed to fill in water–water contacts, and all water molecules manually inspected for good geometry and cryoEM density. A strong density at ND4, tetrahedrally coordinated by a water molecule, an Asp and two His side chains, was modelled as a Zn^{2+} ion. The addition of non-solvent hydrogen atoms and subsequent real-space refinement, with grouped ADP refinement, and validation was performed in PHEINX v1.20.1-4887. Restraints were included for metal–protein coordination and geometry. Iteratively, models were manually adjusted in Coot to improve validation statistics after PHENIX real-space refinements.

DDM-CI-PLs model building and refinement

The CI-in and CI-out open1 and open2 models from the as-prepared CI-PLs models were used as starting models. Water molecules were deleted, where present. For the CI-in and CI-out slack classes, a previous bovine slack model (PDB 7QSO) was used. The models were per-chain, rigid-body fit into respective maps using PHENIX. Residues, non-protein molecules and cryoEM densities were inspected and the models updated accordingly, guided by locally sharpened maps. Following Coot all-atom refinement and PHENIX real-space refinement, models were manually inspected and iterated through PHENIX real-space refinement to improve validation scores.

Deactivated CI-PLs model building and refinement

The CI-in and CI-out open1 and open2 models from the as-prepared CI-PLs models were used as starting models and the same modelling and refinement procedures as used for the DDM-CI-PLs were implemented.

Model validation

All model validation statistics (Tables S1, 3–4) were generated using PHENIX, including its implementation of MolProbity (*80*). Model-to-map FSC curves were generated using PHENIX.

Structural analysis and visualization

Map and model visualization and image generation were performed in UCSF ChimeraX. Map regions of interest were selected with the *volume zone* command. Structural investigations on model files were also performed with UCSF ChimeraX: hydrogen bonds were detected with default parameters of the *hbonds* command; Grotthuss-competent networks were identified using the *contacts* command, with the *distanceOnly* option set to 4 Å (center-to-center), restricted to protonatable O and N atoms of residues D, E, H, K, S, T, and Y and water molecules only; global and per-chain comparison RMSD values were calculated with either the *matchmaker* command or the *align* command when the structures were partially superpositioned; rotation and translations of aligned models were measured with the *measure rotation* command. Cavities were detected using CASTp (1.4 Å-radius solvent probe) and visualized with CASTpyMOL 3.1 plugin and UCSF ChimeraX. The angular distributions of consensus refinements were performed in RELION, recolored using python scripts and visualized in UCSF ChimeraX. Mollweide projections with inputs from the RELION consensus refinements were generated with a python script.

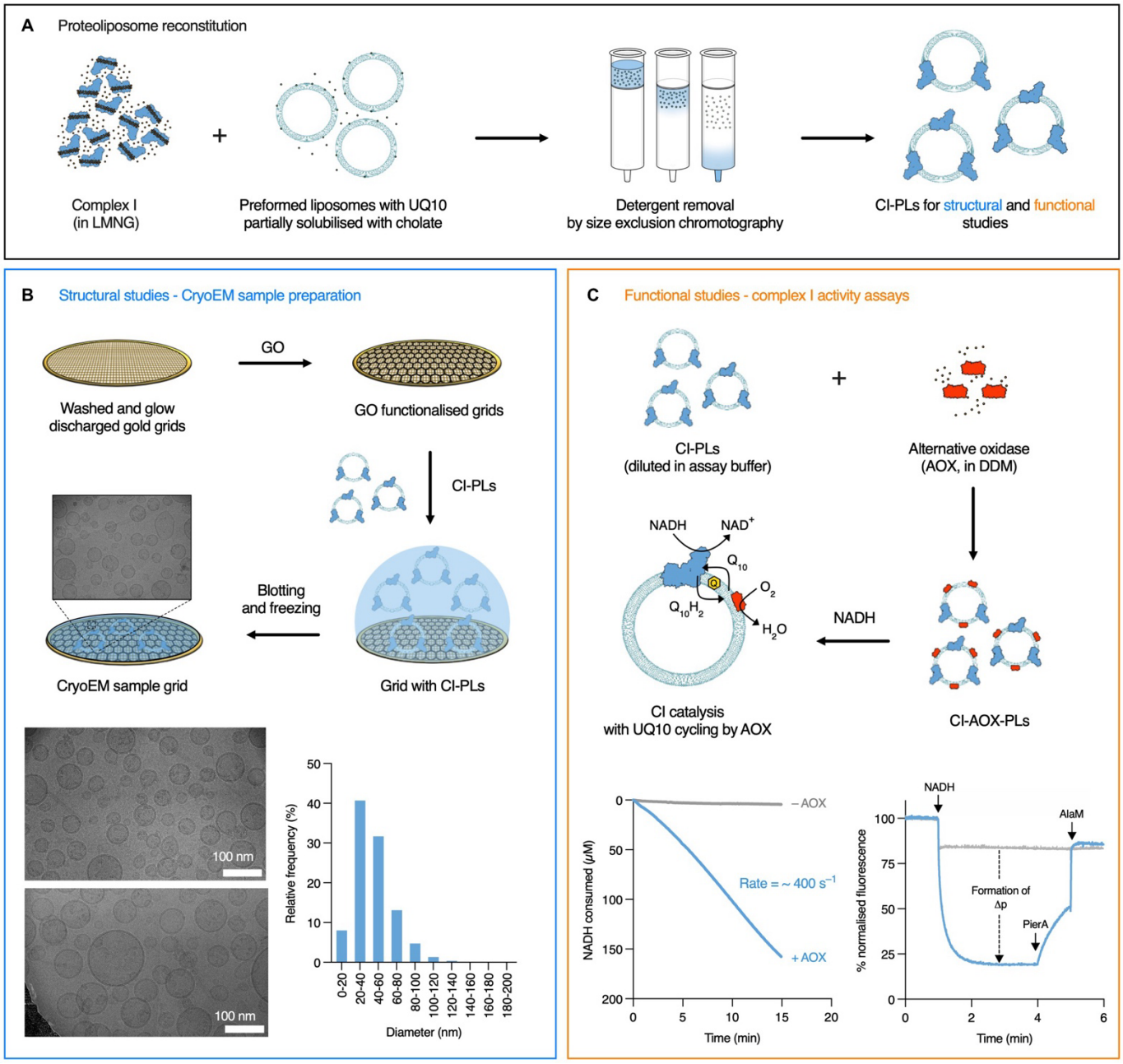


Fig. S1 | Combined biochemical, biophysical and cryoEM strategies for studying complex I-containing proteoliposomes (CI-PLs). A) Preparation of CI-PLs by cholate-mediated reconstitution of complex I into pre-formed liposomes. **B)** Preparation and freezing of functionalized graphene oxide (GO) grids with CI-PLs for cryoEM. Representative micrographs are shown, with the estimated size distribution determined from the edge-to-edge diameters of 1145 proteoliposomes observed in 20 randomly selected micrographs. **C)** Activation of CI-PLs for functional studies. Addition of the ubiquinol oxidase AOX (the alternative oxidase) enables studies of catalysis. In the examples shown, NADH oxidation was catalyzed by 1 nM complex I, and proton pumping into the CI-PL lumen observed by quenching of the fluorescence from the probe 9-amino-6-chloro-2-methoxyacridine (ACMA), with catalysis stopped by addition of piericidin A, then Δp dissipated by addition of alamethicin.

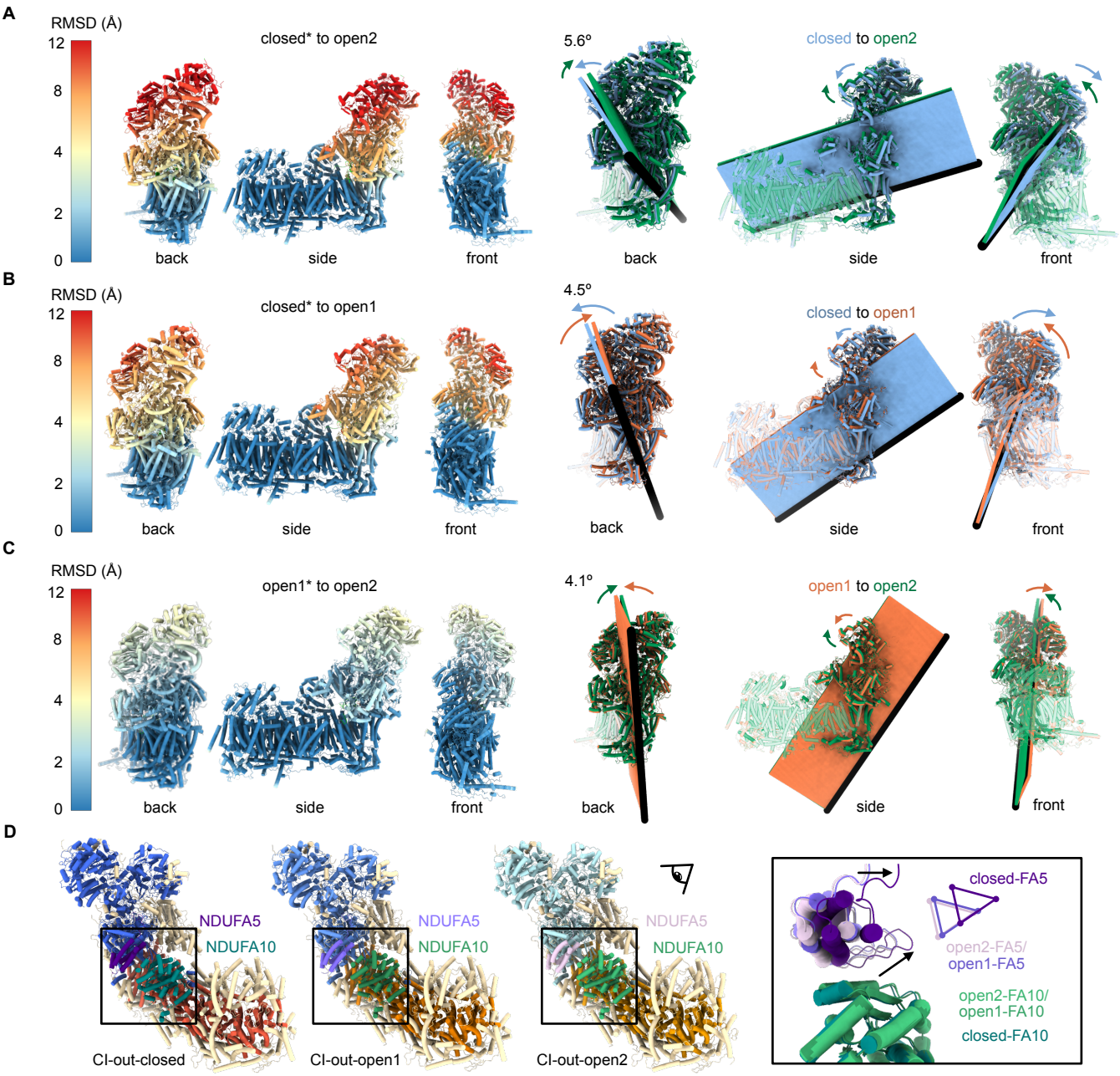


Fig. S2 | Conformational relationships between the closed, open1 and open2 states. A) Conformational relationships between the closed and open2 states. With the structures aligned on the membrane domain, the hydrophilic domains deviate increasingly from one another as the distance from the domain interface increases, approaching root-mean-square deviation (RMSD) values of 12 Å at the top of the domain. The RMSD values are plotted on the closed state structure (marked *). The motion can be described by rotation of the hydrophilic and heel domains (solid) about the axis of rotation (black bar) shown, while the majority of the membrane domain (translucent) does not move. The planes are shown to illustrate the angle of rotation. **B–C)** Conformational relationships between the closed and open1, and open1 and open2 states displayed as in panel **A**. The open1 state lies between the closed and open2 states, and while a similar axis of rotation can be identified between the two open states the extent of the relative displacement is much less. **D)** Variation in the relative positions of NDUFA5 (hydrophilic domain) and NDUFA10 (membrane domain) between the states. Non-NDUFA5/NDUFA10 supernumerary subunits are in wheat and core subunits in red/orange and light/dark blue for closed/open states, respectively. NDUFA5 and NDUFA10 are colored as labelled. Boxed regions are equivalent and highlight NDUFA5/NDUFA10 interface adjustment due to rotation of the hydrophilic arm (relative to the membrane arm) between the states. For clarity, the centers of the three shifted helices are illustrated with colored triangles also.

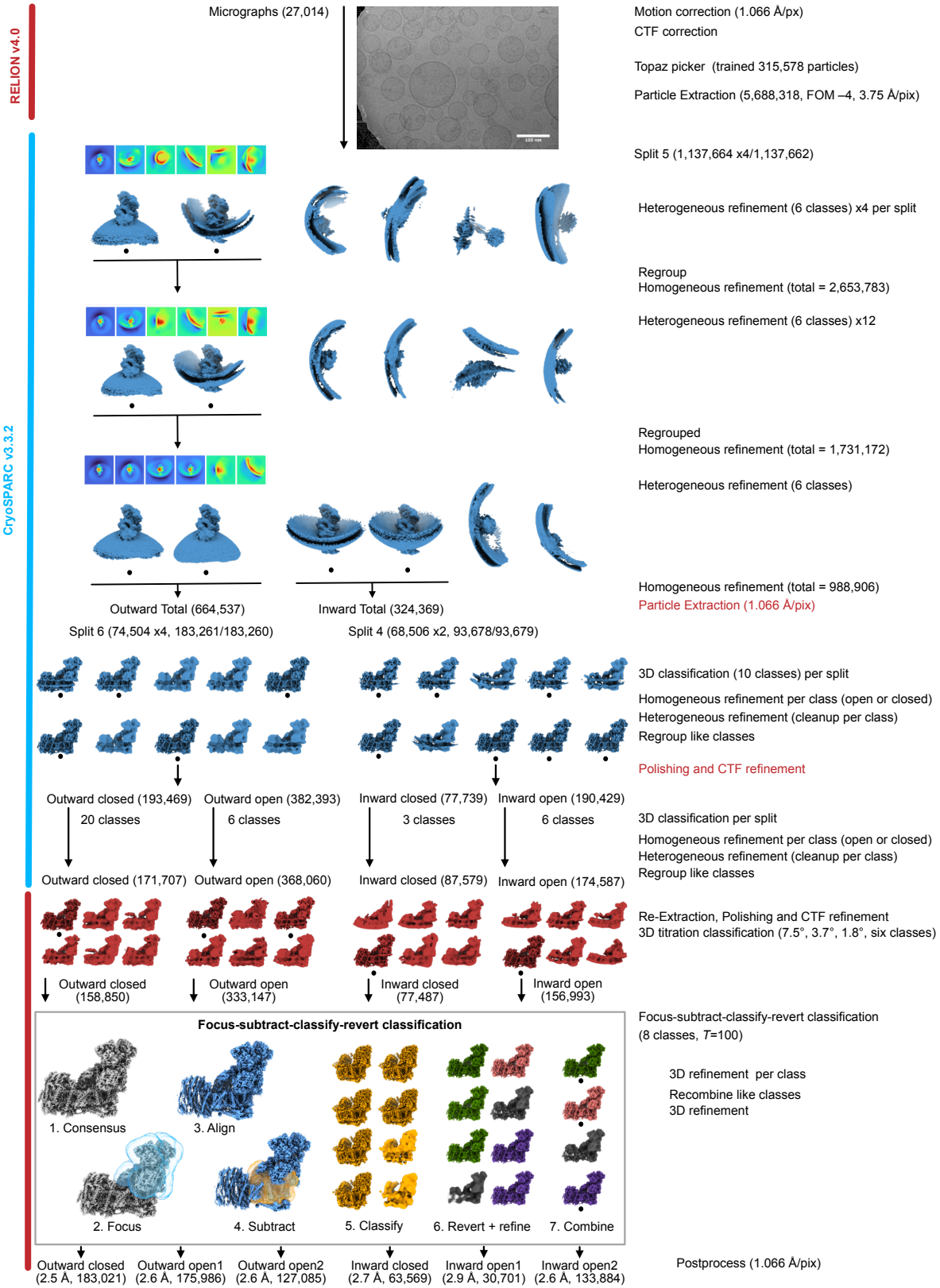


Fig. S3 | Classification scheme for the CI-PLs dataset (purified in LMNG, as prepared). An example micrograph and 3D volumes are shown along with cryoEM density heatmaps for volumes in cryoSPARC heterogeneous refinements. Volumes taken forward are indicated with a black dot. The software used to perform each step is indicated by the left-hand color bar (red text indicates RELION-specific stage exceptions). The focus-subtract-classify-revert classification method is outlined in the grey box using example volumes for the outward closed analysis.

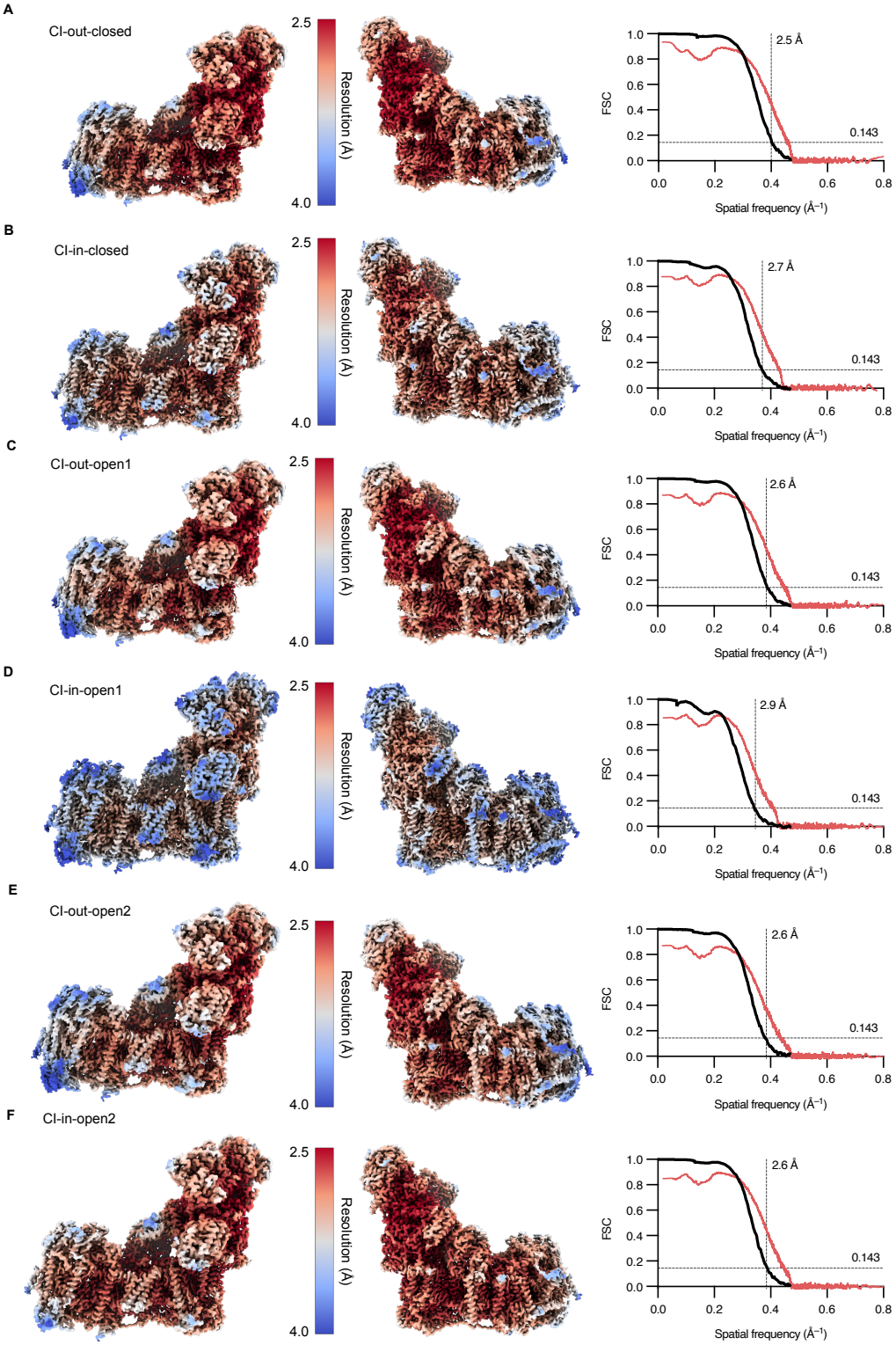


Fig. S4 | Global and local resolution of the consensus classes of the CI-PLs dataset (purified in LMNG, as prepared). The final classes **A**) CI-out-closed, **B**) CI-in-closed, **C**) CI-out-open1, **D**) CI-in-open1, **E**) CI-out-open2, and **F**) CI-in-open2 were analyzed for local resolution distribution using RELION v4.0-beta. Values are plotted according to the color key. Global Fourier Shell Correlation (FSC) scores (cutoff = 0.143) calculated in RELION v4.0-beta are plotted (black) along with model–map FSCs (red), calculated using the validation suite in PHENIX v1.20.1-4487.

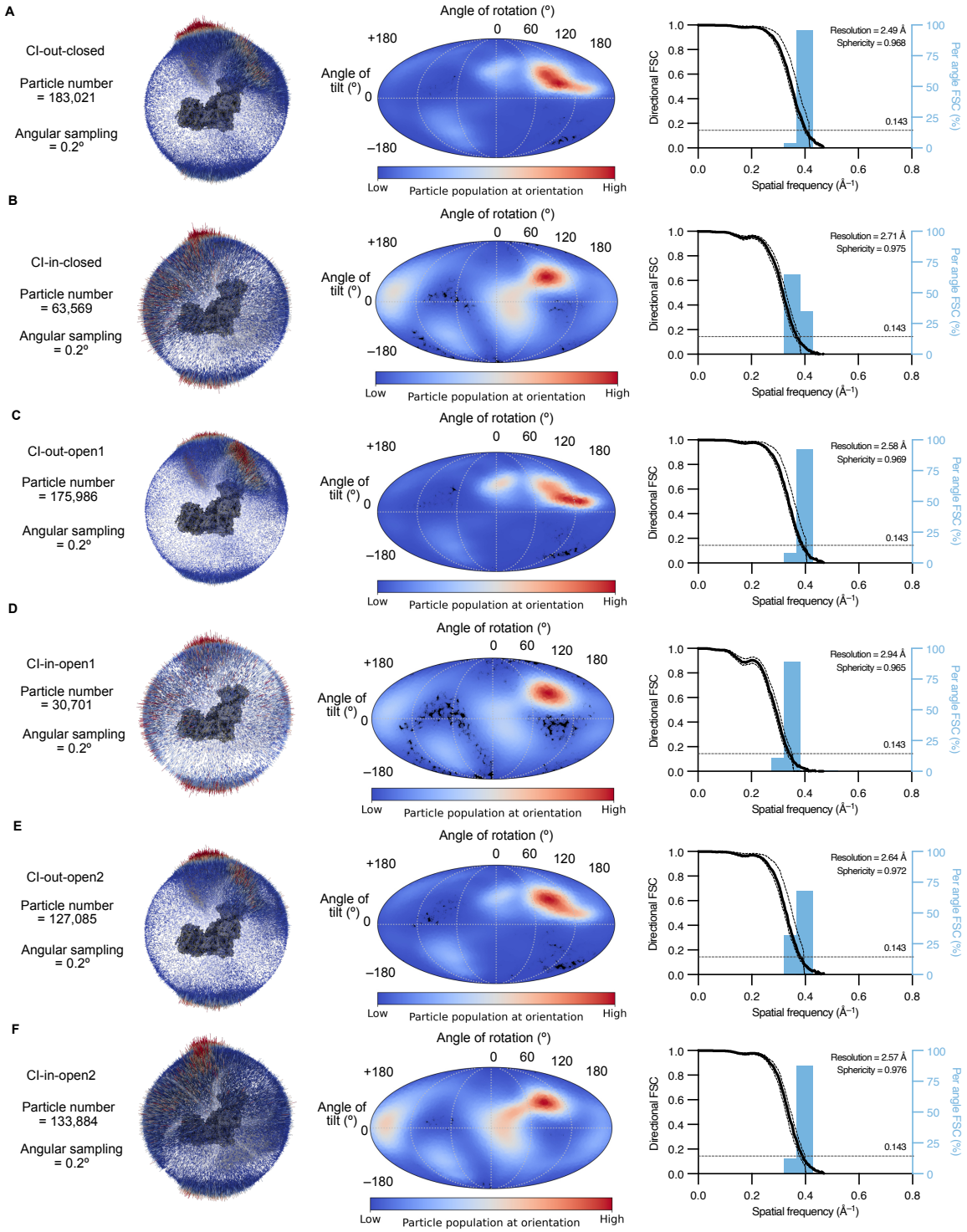
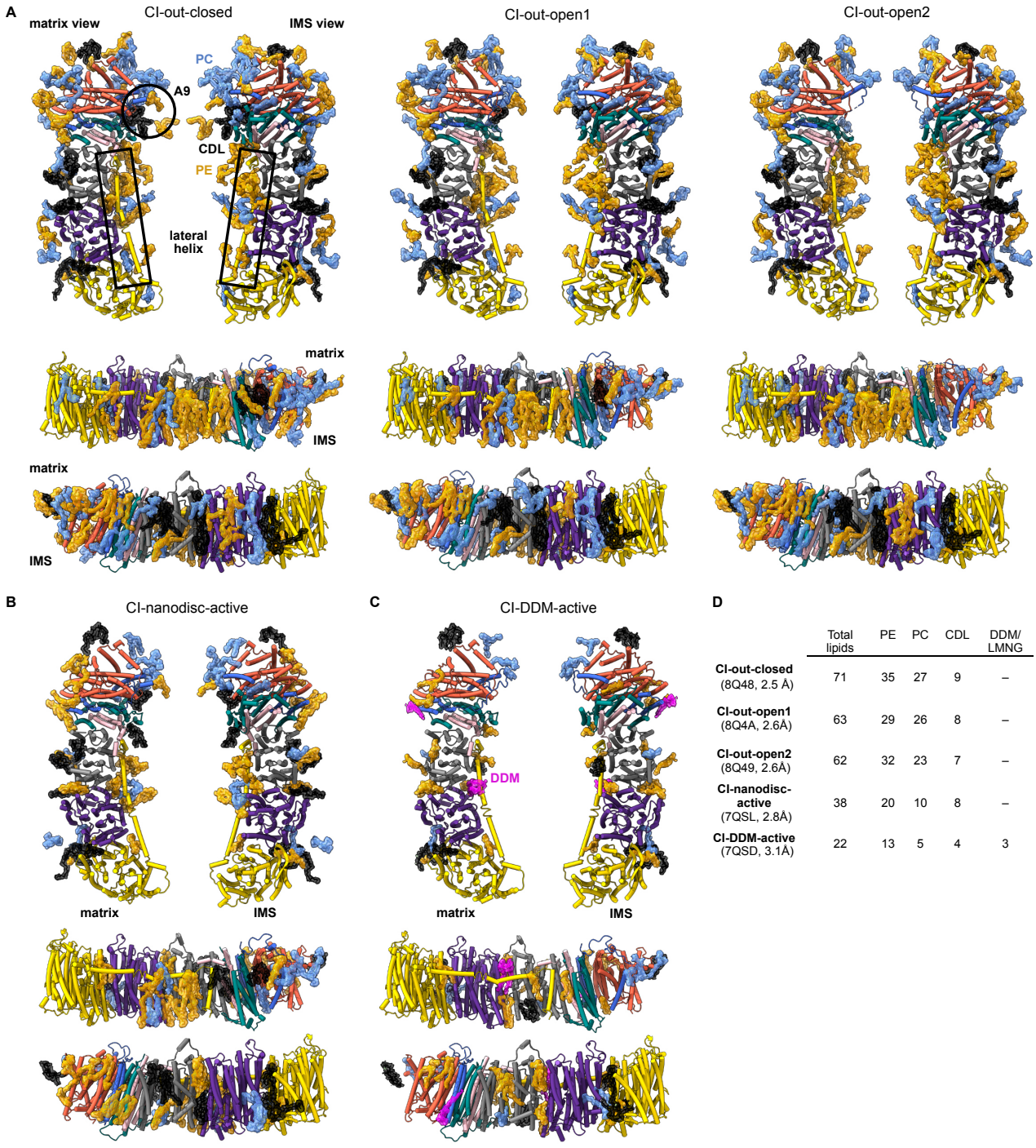


Fig. S5 | Orientation analyses of the consensus classes of the CI-PLs dataset (purified in LMNG, as prepared). The final classes **A**) CI-out-closed, **B**) CI-in-closed, **C**) CI-out-open1, **D**) CI-in-open1, **E**) CI-out-open2, and **F**) CI-in-open2 were inspected for the orientation distribution of the particles in the final consensus alignment using 3D angular and Mollweide plots. Equivalent data are shown in each case. The orientation distribution in the Mollweide plots is relative to the input reference volume, so the complex I 3D volumes (grey) in each case are shown in the 3D angular distribution spheres for reference. The assessment of uniformity of resolution in each direction (sphericity, where 1 is completely uniform) was performed by dividing the sphere up into cones and calculating directional Fourier-shell correlations (FSCs), plotted as histograms, using the 3DFSC Program Suite v3.0. The 3DFSC global FSC curve is shown in black (± S.D. of directional FSCs).



D

	Total lipids	PE	PC	CDL	DDM/ LMNG
CI-out-closed (8Q48, 2.5 Å)	71	35	27	9	–
CI-out-open1 (8Q4A, 2.6Å)	63	29	26	8	–
CI-out-open2 (8Q49, 2.6Å)	62	32	23	7	–
CI-nanodisc-active (7QSL, 2.8Å)	38	20	10	8	–
CI-DDM-active (7QSD, 3.1Å)	22	13	5	4	3

Fig. S6 | The composition and distribution of phospholipids modelled for bovine complex I in proteoliposomes, nanodiscs and detergent. **A**) The phospholipids [cardiolipin, (CDL, black), phosphatidylcholine (PC, blue) and phosphatidylethanolamine (PE, orange)] are shown (with cryoEM densities) for the different outward-facing states of complex I observed in proteoliposomes. The views are shown facing the matrix, the intermembrane space (IMS) and from each side, with the core membrane subunits shown also. The matrix lipid-binding site of NDUFA9 (A9) is indicated with a black circle. The lateral helix of ND5 is indicated with a boxed outline. **B**) The same comparison as in **A** but for bovine complex I in nanodiscs and **C**) bovine complex I in an *n*-dodecyl-β-D-maltopyranoside (DDM, pink)–lipid micelle. DDM molecules replace lipids in the detergent structure, relative to the structures in proteoliposomes (**A**) and nanodiscs (**B**). **D**) A summary of the lipid and detergent compositions for the different bovine complex I structure. We did not observe any DDM in our CI-PLs prepared with complex I purified in DDM. Overall, there is good conservation of lipid type and location, most notably for the mitochondria-specific cardiolipin that is vital for complex I activity.

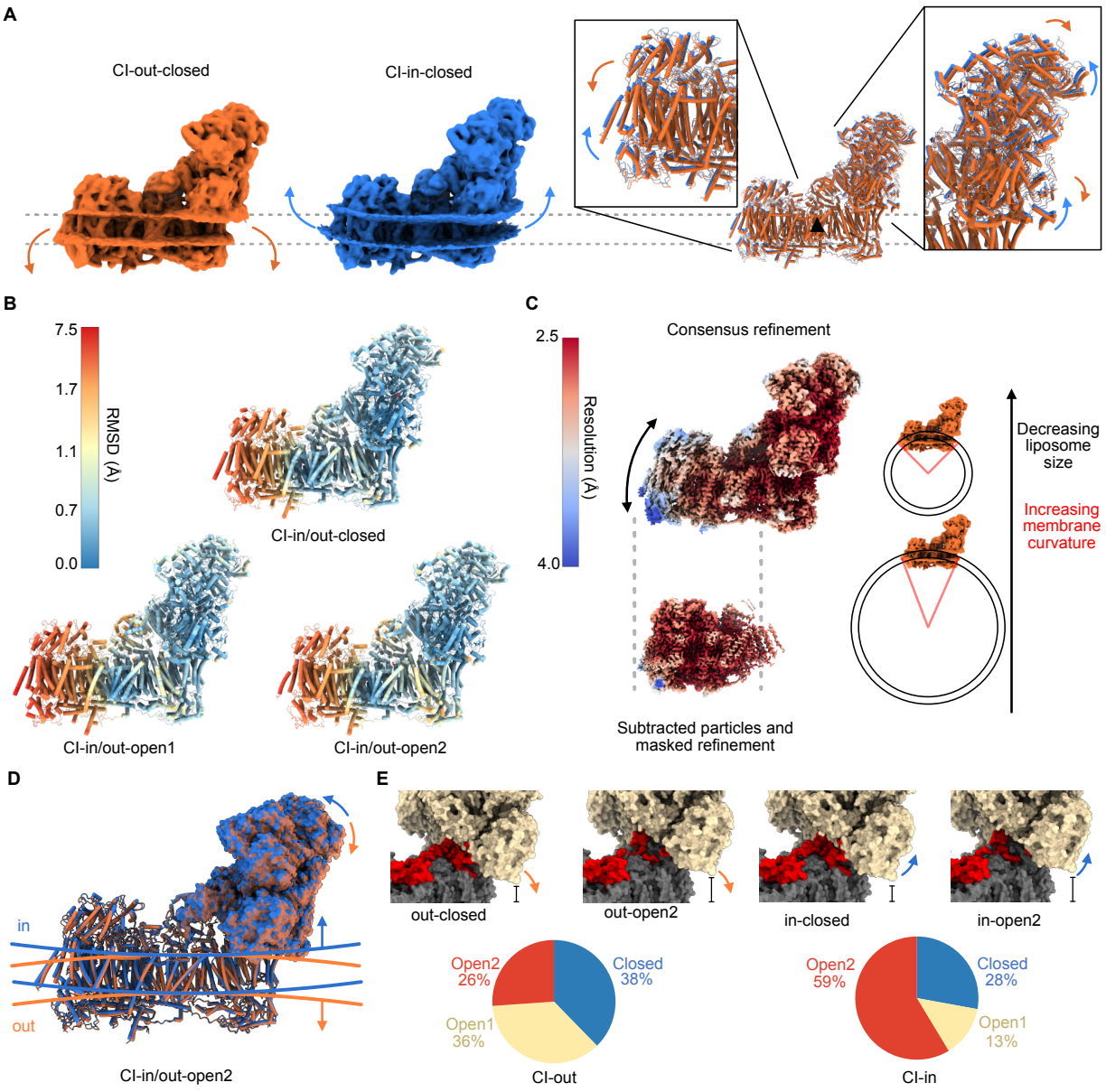


Fig. S7 | Complex I in outward-facing and inward-facing orientations and the effects of membrane curvature on its global conformation. A) The volumes of CI-out-closed and CI-in-closed shown with arrows to indicate the influence of membrane curvature on protein conformation, emphasized by alignment of the models on the membrane-central ND2 subunit (black triangle). Inset boxes show the extremities of the domains are affected most, with membrane-domain transmembrane helices following the curvature, and amphipathic helices at the base of the hydrophilic domain anchored at the varied membrane surface height. **B**) The effects of membrane curvature on each of the three states, shown as the root-mean-square deviation (RMSD, Å) plotted, according to the color bar, on the respective outward models. All polypeptide chains were included in global RMSD minimization in ChimeraX before model pairwise RMSD values were calculated. **C)** Comparison of local resolutions for the distal section of the membrane domain (containing subunits ND4 and ND5) in the CI-out-closed maps from a consensus refinement with the same particles subtracted and refined on the distal section. In the consensus refinement the iron-sulfur cluster-containing hydrophilic domain dominates the global alignment, disguising the high-resolution information available for the distal section. The diagram shows how the distribution in liposome sizes creates the distribution in membrane curvature across the complex that causes the effect in the refinements. D) The effect of membrane curvature on the CI-out-open2 and CI-in-open2 models, where the influence of the curvature on the hydrophilic domain is greatest for the inward-curving inner bilayer. E) The areas of local differences between the closed and open2 states (red surfaces) are shown for respective inward- and outward-facing models. The hydrophilic domain is shown in wheat and the core membrane domain in grey. The direction of curvature is indicated with arrows and reference markers are used to show marginal adjustments of the hydrophilic domain in response to the curvature. The pie charts show the relative proportions of the closed, open1 and open2 states for the inward and outward populations, where inward appears to disfavour the closed state and promote the open2 state. The greatest bilayer curvature experienced at the hydrophilic–membrane interface is for the inward-facing enzyme, and this may induce selectivity during reconstitution, or add additional packing strain to the local elements that are ordered in the closed state, promoting opening. Note that the inward-facing population exhibits the same activity as the outward-facing population (Fig. S12).

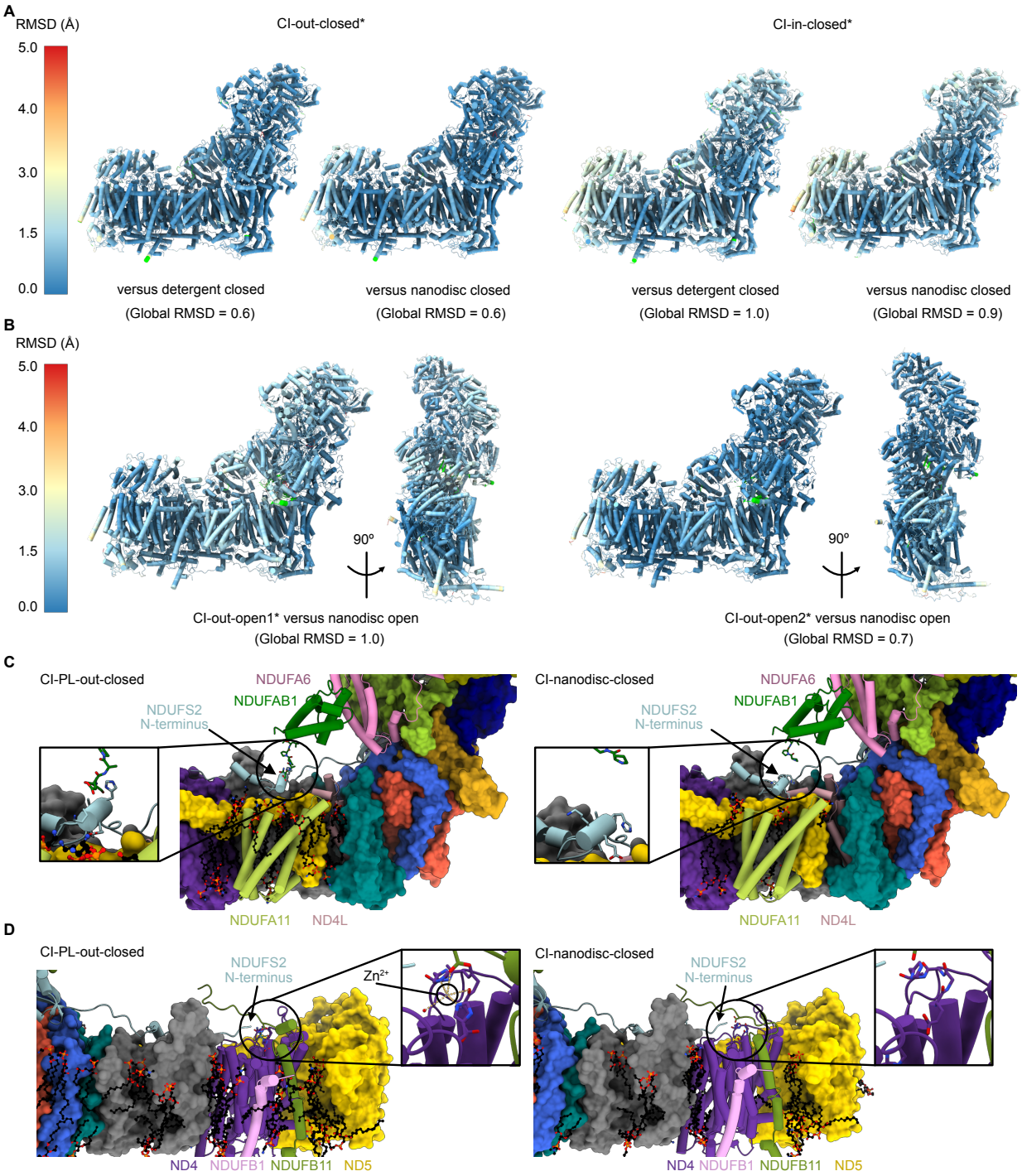


Fig. S8 | Comparisons of the closed, open1 and open2 states present in CI-PLs with equivalent structures determined in DDM micelles and nanodiscs. A) Root-mean-square deviation (RMSD) values (Å) between the outward/inward closed state models determined here and equivalent models determined in DDM micelles (PDB:7QSD) and nanodiscs (PDB:7QSK). The values reported in the panel titles are the global values; similarity is highest for the outward orientation, and very similar for the DDM and nanodisc models. Asterisks indicate the model used to display the values. Lime green indicates unmatched residues due to modelling differences. **B)** RMSD values (Å) between the outward open1 and open2 state models determined here and the equivalent 'deactive' model determined in nanodiscs (PDB:7QSN); the latter resembles open2 more than open1. **C**) The N-terminus of NDUFAB1 in complex I in CI-PLs is ordered and tethered to the membrane domain whereas in CI in nanodiscs (as well as in CI in detergent) it is disordered. **D**) The position of a Zn^{2+} modelled in the ND4 subunit in CI-PLs and the equivalent region in complex I in nanodiscs. Inset shows coordination distances of 2.3 Å for $His82^{ND4}$ and $His338^{ND4}$ in the axial positions of an approximately trigonal bipyramidal arrangement with $Glu335^{ND4}$, $Asp34^{NDUFB1}$ and a water molecule in the equatorial plane at 3.3–3.7 Å distance. For panels **C–D**, the closed state is shown in both instances, but the features shown for CI-PLs persist in the other states, with the high abundance of lipids and lateral pressure in proteoliposomes likely encouraging preservation of these features.

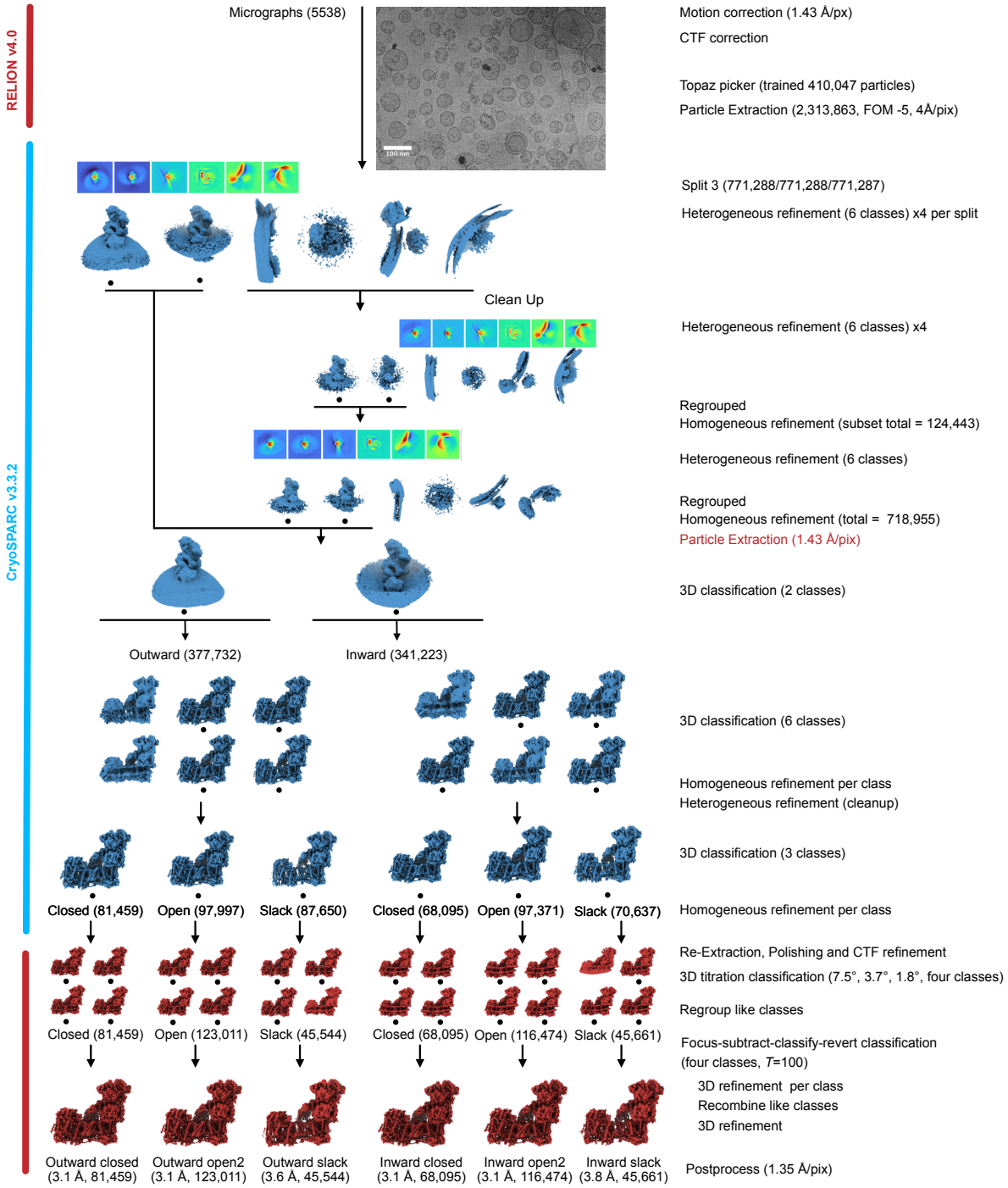


Fig. S9 | Classification scheme for the DDM-CI-PLs dataset (purified in DDM, as prepared). An example micrograph and 3D volumes are shown along with cryoEM density heatmaps for volumes in cryoSPARC heterogeneous refinements. Volumes taken forward are indicated with a black dot. The software used to perform each step is indicated by the left-hand color bar (red text indicates RELION-specific stage exceptions). The focus-subtract-classify-revert classification method is described in more detail in the methods and Fig. S3. The open state was assigned as open2 by comparison with the CI-PLs open1 and open2 states.

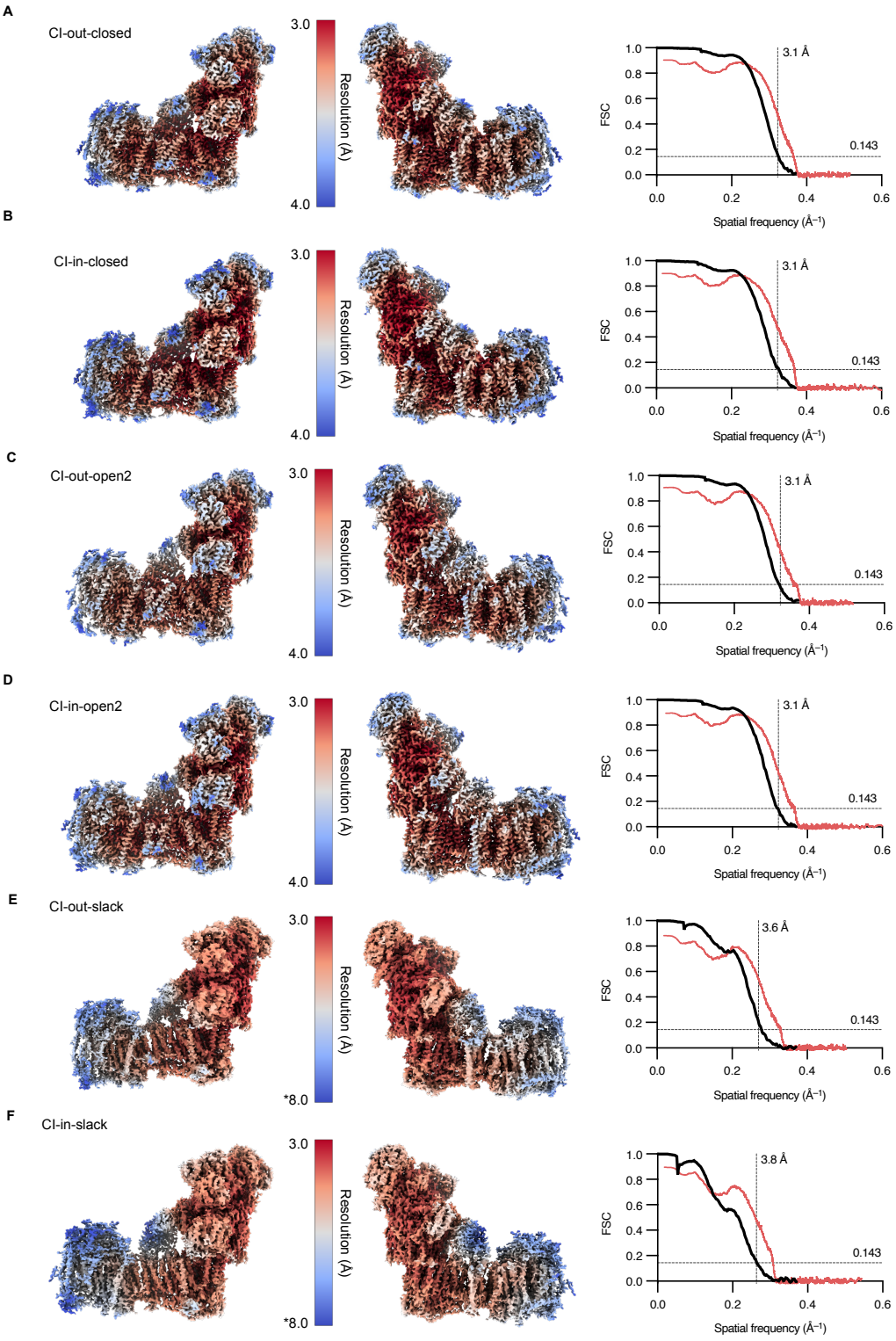


Fig. S10 | Global and local resolution of the consensus classes of the DDM-CI-PLs dataset (purified in DDM, as prepared). The final classes **A**) CI-out-closed, **B**) CI-in-closed, **C**) CI-out-open2, **D**) CI-in-open2, **E**) CI-out-slack, and **F**) CI-in-slack were analyzed for local resolution distribution using RELION v4.0-beta. Values are plotted according to the color key. (*) Note for (**E**) CI-out-slack and (**F**) CI-in-slack, the upper value is shifted to 8.0 Å to accommodate the overall lower resolution distribution. Global Fourier Shell Correlation (FSC) scores (cutoff = 0.143) calculated in RELION v4.0-beta are plotted (black) along with model–map FSCs (red), calculated using the validation suite in PHENIX v1.20.1-4487.

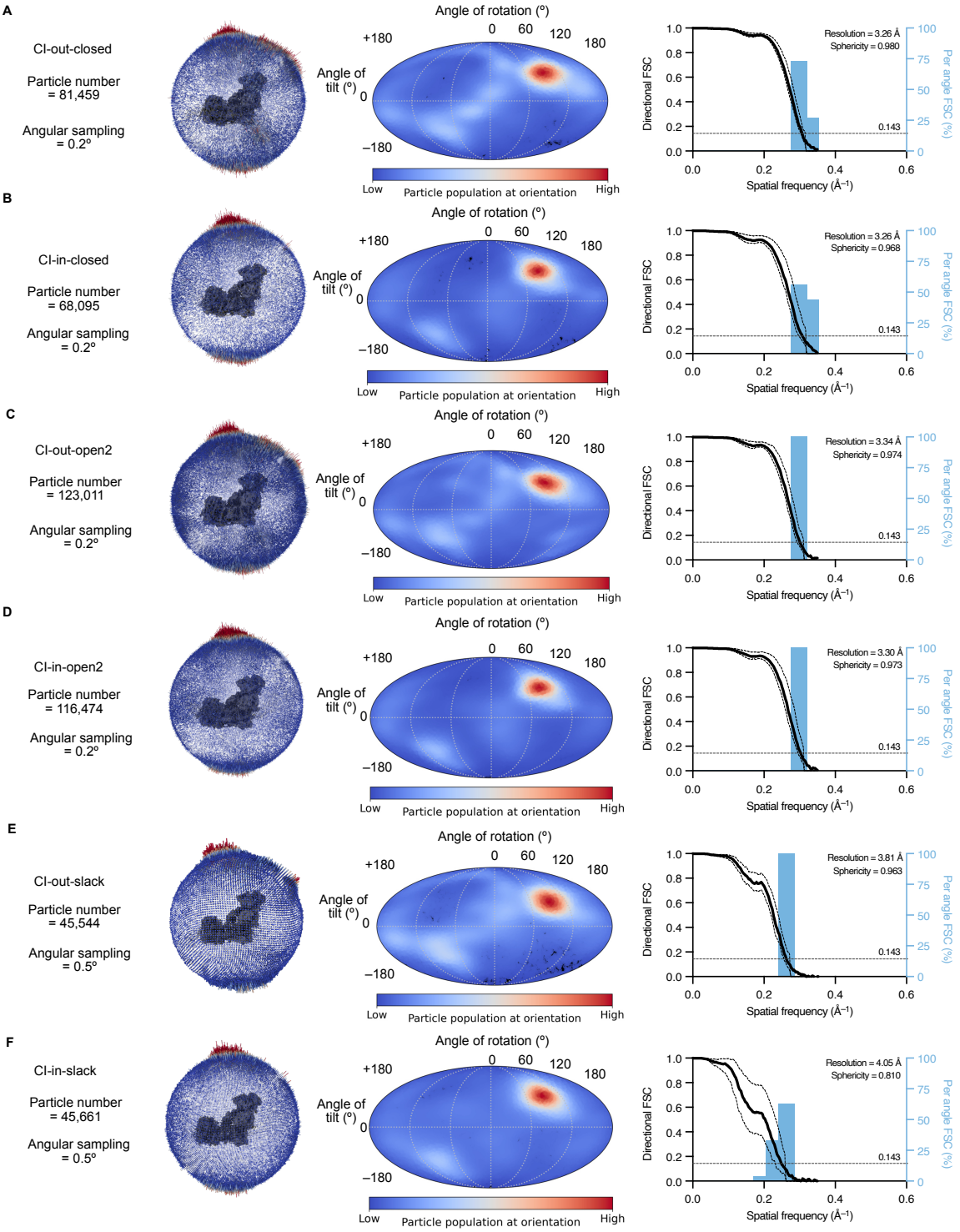


Fig. S11 | Orientation analyses of the consensus classes of the DDM-CI-PLs dataset (purified in DDM, as prepared). The final classes **A**) CI-out-closed, **B**) CI-in-closed, **C**) CI-out-open2, **D**) CI-in-open2, **E**) CI-out-slack, and **F**) CI-in-slack were inspected for the orientation distribution of the particles in the final consensus alignment using 3D angular and Mollweide plots. Equivalent data are shown in each case. The orientation distribution in the Mollweide plots is relative to the input reference volume, so the complex I 3D volumes (grey) in each case are shown in the 3D angular distribution spheres for reference. The assessment of uniformity of resolution in each direction (sphericity, where 1 is completely uniform) was performed by dividing the sphere up into 100 evenly sampled cones and calculating directional Fourier-shell correlations (FSCs) plotted as histograms, using the 3DFSC Program Suite v3.0. The 3DFSC global FSC is shown in black (± S.D. of directional FSCs).

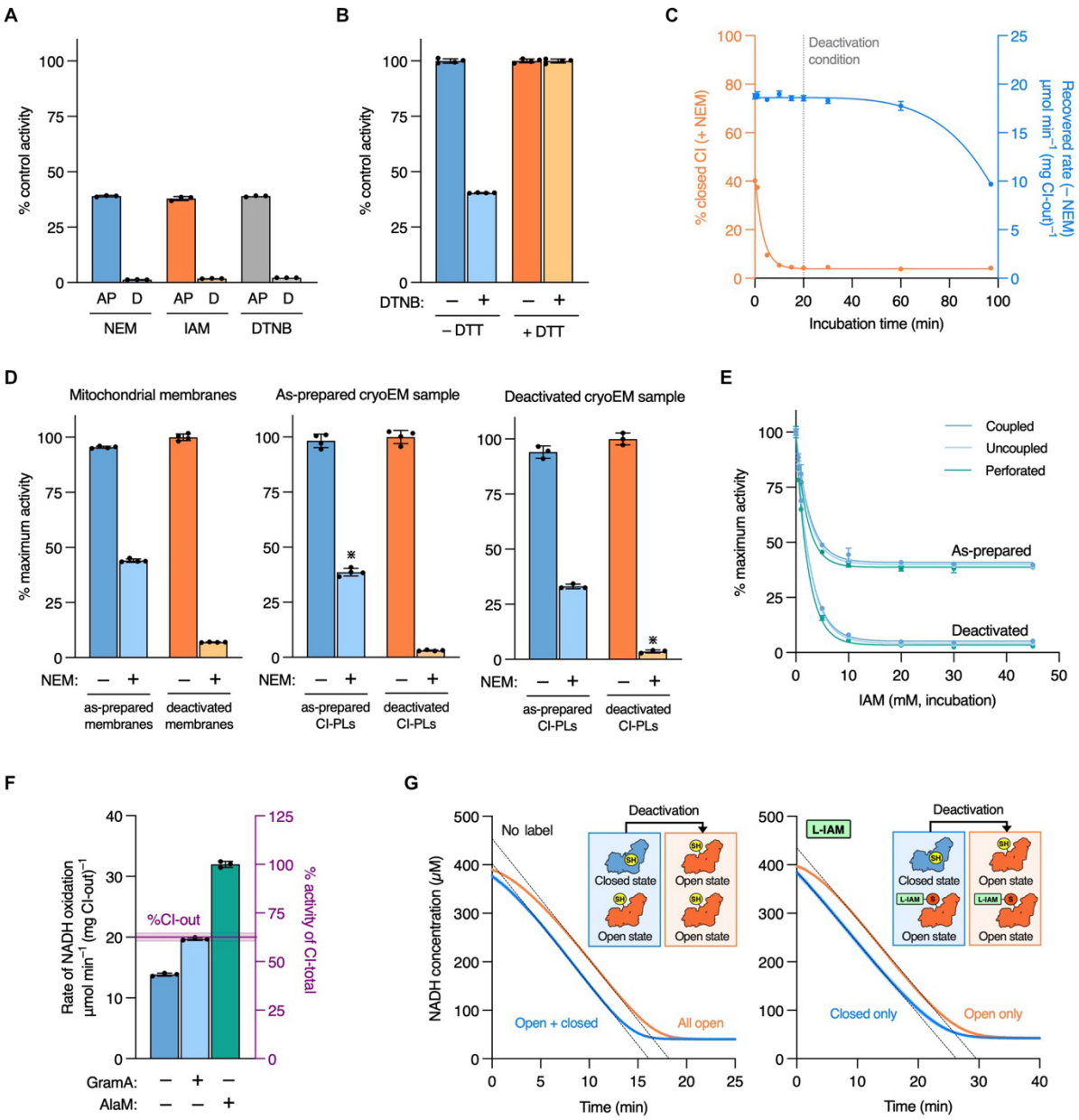


Fig. S12 | Supporting data on the biochemical characterization and deactivation of CI-PLs. A) Comparison of data from three thiol-reactive reagents, N-ethyl maleimide (NEM), iodoacetamide (IAM), and 5,5′-dithiobis-(2-nitrobenzoic acid) (DTNB), used to assess the proportion of CI-closed in as-prepared (AP) and deactivated (D) CI-PLs. The proportion of the control NADH oxidation activity (AP sample incubated without the label) is reported following incubation on ice with NEM (1 mM, 30 mins), IAM (20 mM, 30 mins), or DTNB (0.2 mM, 1 hour). **B)** Treatment with DTT (1 mM, 5 mins, 20 ºC) removes the DTNB from CI-open, returning the catalytic activity to the starting value (no DTNB treatment). **C)** Deactivation of CI-PLs during incubation at 37 ºC. Aliquots were removed and placed on ice in the presence (orange) or absence (blue) of 1 mM NEM for 20 mins before the rate of NADH:O_2 oxidoreduction was determined using AOX. The total recoverable rate is shown in blue and the proportion of CI-closed is shown as the NEM sensitivity in orange. The time chosen for preparation of deactive samples is indicated. **D)** NEM sensitivity measurements on the mitochondrial membranes (n = 4) used for cryoEM sample preparation, and on the as-prepared (n = 3) and deactivated CI-PLs used for cryoEM analyses. Activities are relative to the highest value in the set, and the proportion of CI-closed present under the conditions for cryoEM sample preparation (in the absence of NEM) are indicated with an asterisk. **E)** The effect of increasing IAM concentration on complex I activity in as-prepared and deactivated CI-PLs. Rates of NADH oxidation were measured with AOX under coupled, uncoupled (gramicidin A), or perforated (with alamethicin) conditions following IAM treatment. The data show IAM has derivatized both CI-out and CI-in in all cases. **F)** The rate of NADH oxidation by AOX-CI-PLs that were coupled, uncoupled (gramicidin A, CI-out only) or perforated (alamethicin, CI-out and CI-in) matches the proportion of CI-out determined by the NADH:APAD$^+$ oxidoreduction assay (horizontal line, 62.6 ± 2.1%). **G)** Experiment matching that in Fig. 2D except using IAM to label the open states. The assay traces from unlabeled and IAM-labelled as-prepared CI-PLs are linear for the closed-only enzyme and display an activation lag phase when the open state is present. n = 3 for all experiments unless otherwise stated.

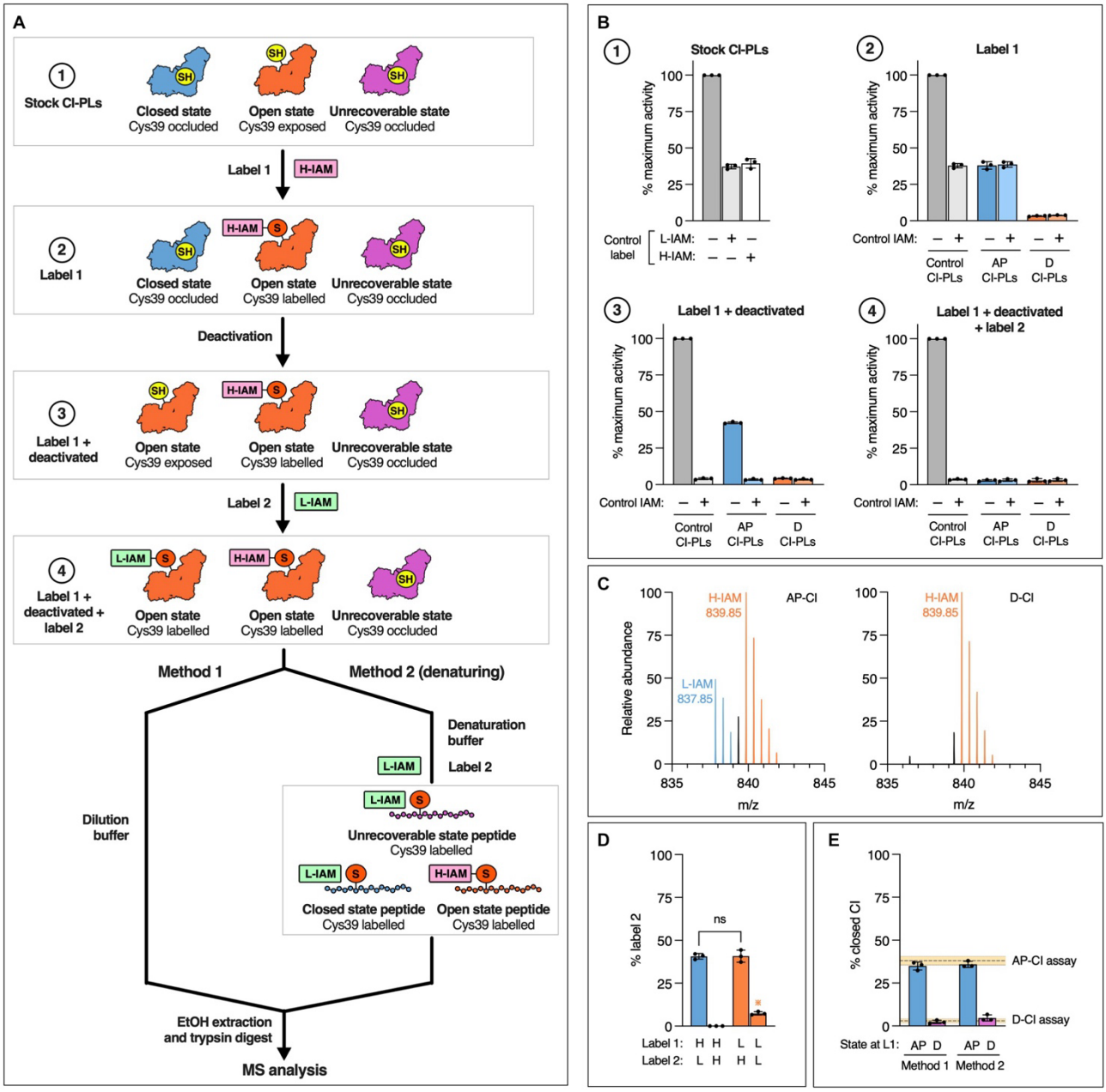


Fig. S13 | Summary of the differential isotopic labelling of CI-PLs for mass spectrometry analyses. A) The labelling scheme shown for a mixed population of CI-PLs containing CI-closed (Cys39^{ND3} occluded) and CI-open (Cys39^{ND3} exposed), plus a prospective population of catalytically inactive (unrecoverable) CI with Cys39 occluded (for example, aggregated enzyme). After treatment with Label 2 the sample is either treated for MS (method 1), or first denatured in the present of Label 2 (method 2) to capture the unrecoverable enzyme. **B)** NADH:O_2 oxidoreduction assays at each step in the labelling scheme in **A** relative to the maximal activity observed with a vehicle control sample (treated identically but without label). At stage 1 the equal effect of L-IAM and H-IAM is demonstrated for an example set of as-prepared CI-PLs. For stages 2 to 4, data are presented for Control CI-PLs (treated identically but without preceding labels), as-prepared CI-PLs (AP-CI) and deactivated CI-PLs (D-CI), with the activities are shown with and without an additional IAM labelling step (± control IAM, 20 mM L-IAM, 30 mins) to confirm completion of labelling and deactivation processes. The data are mean averages (± SD) of the three independent CI-PL reconstitutions used for MS analyses. **C)** Representative mass spectra of as-prepared and deactivated CI-PLs treated according to the scheme in **A**, method 1. Peaks from the H-IAM labelled ND3 peptide (monoisotopic peak at 839.85 Da) are in orange, and those from the L-IAM labelled peptide (monoisotopic peak at 837.85 Da) are in blue. **D)** The Label-2 monoisotopic peak intensity as a proportion of the combined Label-1 and Label-2 intensities for as-prepared CI-PLs. Reversing the H-IAM and L-IAM labels does not affect the results (the percentage of CI-closed); the signal observed at 839.85 Da when L-IAM is used for both labelling steps likely arises from the natural abundance of ^{13}C. The data are mean averages (± SD) of three ethanol extractions from a single sample for each condition, with statistical significance assessed by one-way ANOVA. **E)** The percentage of CI-closed determined using scheme **A**, method 1 and method 2 (bars) and by catalytic activity assays (horizontal lines). The data are mean averages (± SD) of three independent preparations for as-prepared and deactivated CI-PLs. $n = 3$ for all experiments.

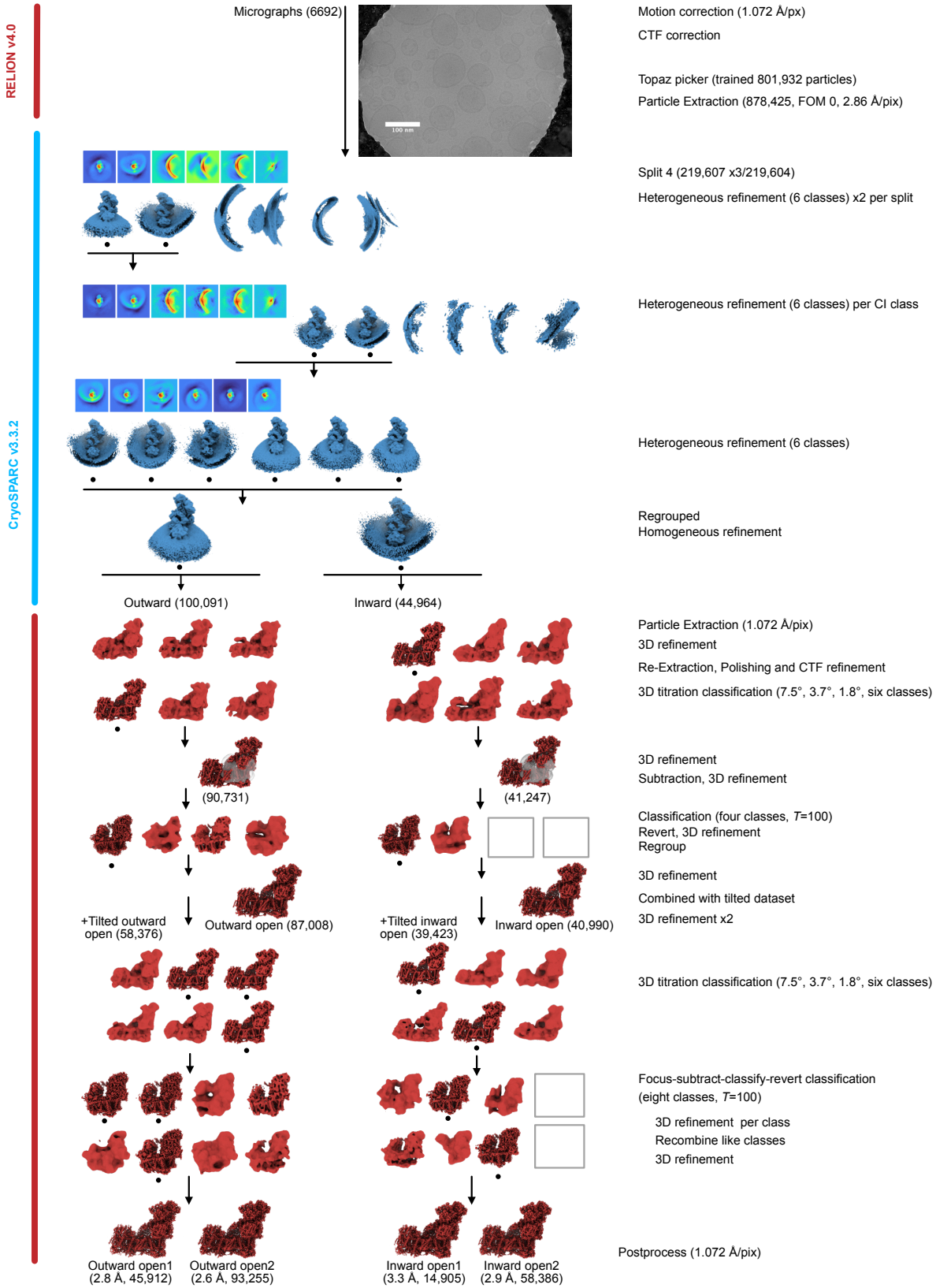


Fig. S14 | Classification scheme for the non-tilted, deactivated CI-PLs dataset. An example micrograph and 3D volumes are shown along with cryoEM electron density heatmaps for volumes in cryoSPARC heterogeneous refinements. Volumes taken forward are indicated with a black dot. The software used to perform each step is indicated by the left-hand color bar. Empty boxes indicate non-populated 3D classes. The focus-subtract-classify-revert classification method is described in more detail in the Methods and Fig. S3. See Fig. S15 for the tilted dataset.

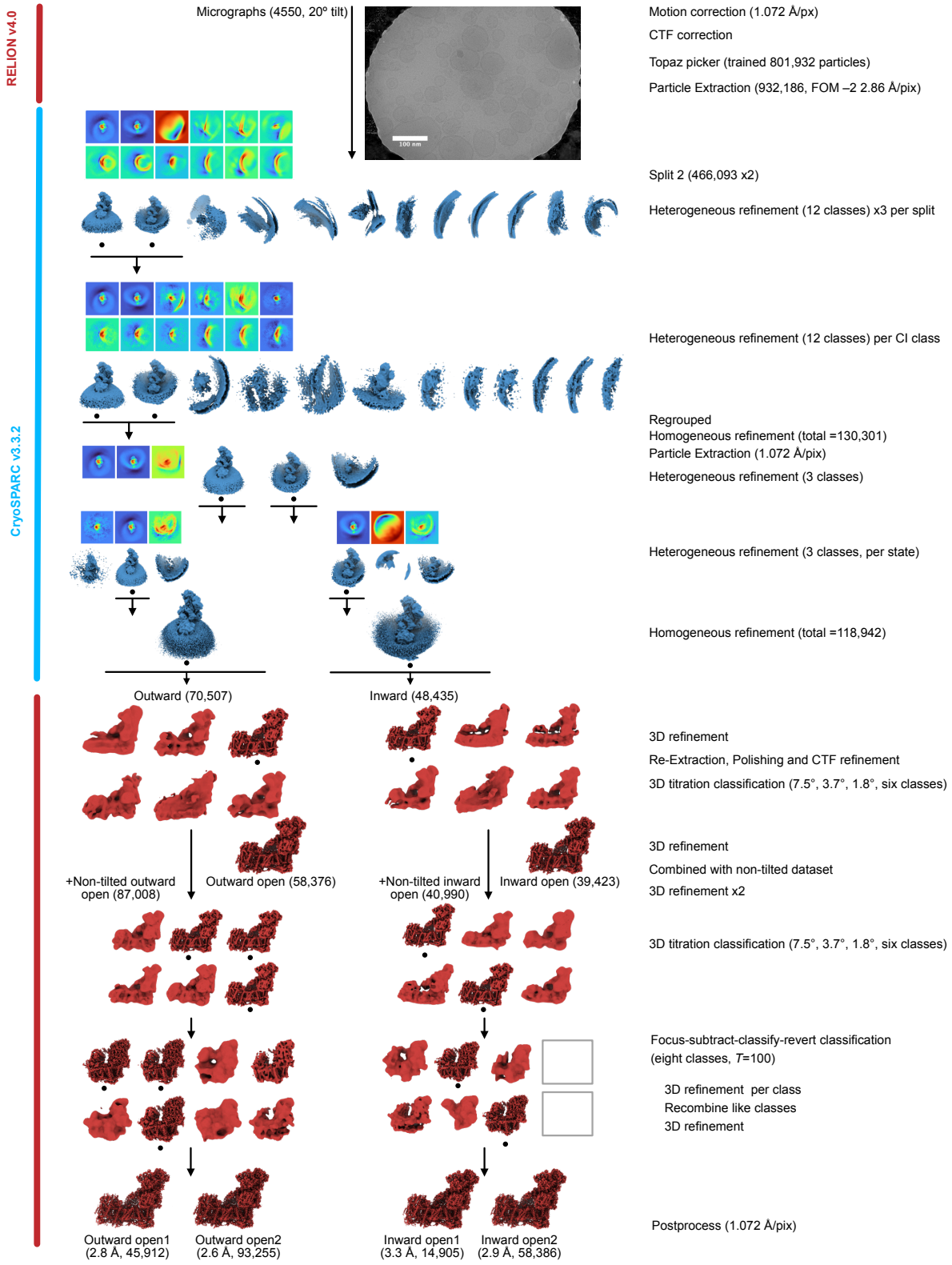


Fig. S15 | Classification scheme for the tilted, deactivated CI-PLs dataset. An example micrograph and 3D volumes are shown along with cryoEM electron density heatmaps for volumes in cryoSPARC heterogeneous refinements. Volumes taken forward are indicated with a black dot. The software used to perform each step is indicated by the left-hand color bar. Empty boxes indicate non-populated 3D classes. The focus-subtract-classify-revert classification method is described in more detail in the Methods and Fig. S3. See Fig. S14 for the non-tilted dataset.

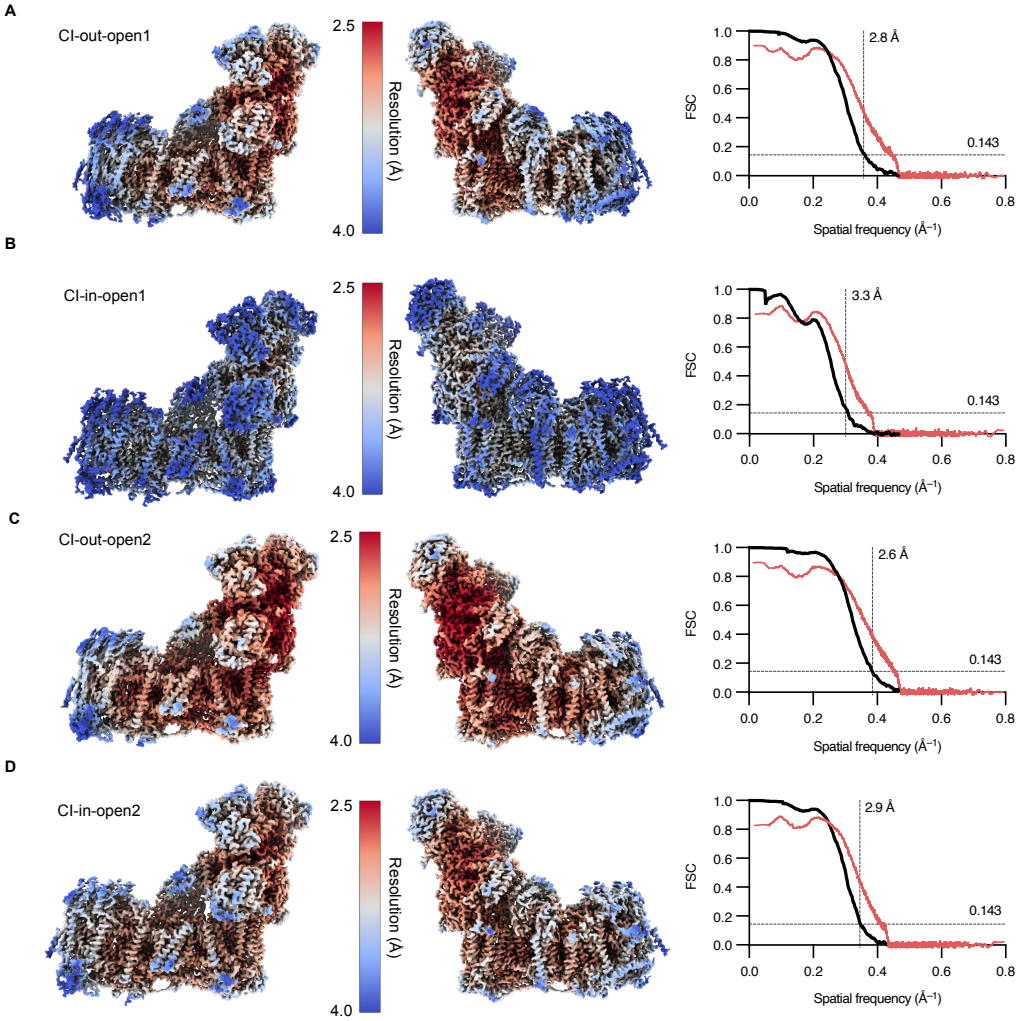


Fig. S16 | Global and local resolution of the consensus classes of the combined (non-tilted and tilted) deactivated CI-PLs dataset. The final classes **A**) CI-out-open1, **B**) CI-in-open1, **C**) CI-out-open2, and **D**) CI-in-open2 were analyzed for local resolution distribution using RELION v4.0-beta. Values are plotted according to the color key. Global Fourier Shell Correlation (FSC) scores (cutoff = 0.143) calculated in RELION v4.0-beta are plotted (black) with model–map FSCs (red), calculated using the validation suite in PHENIX v1.20.1-4487.

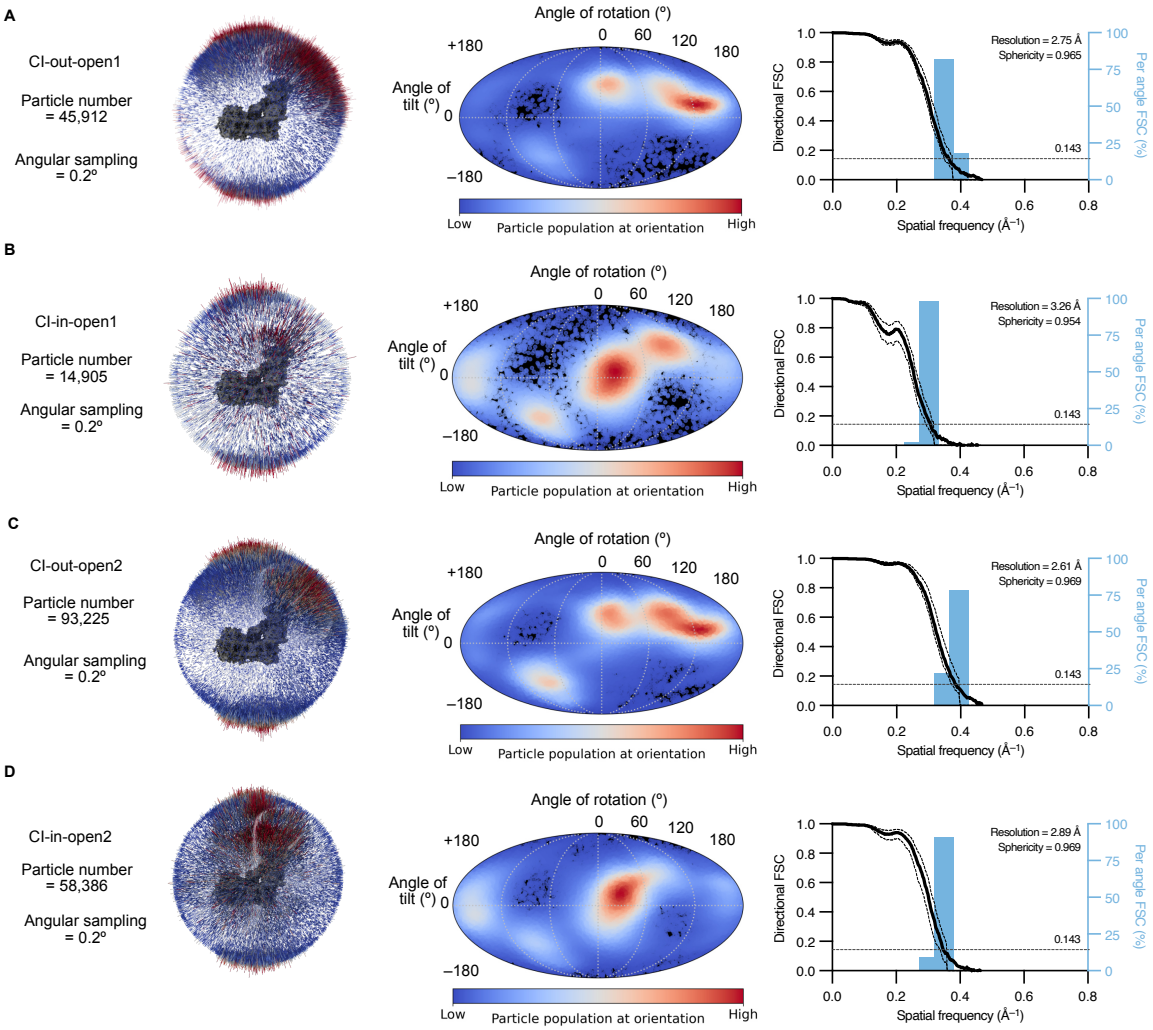


Fig. S17 | Orientation analyses of the consensus classes of the combined (non-tilted and tilted) deactivated CI-PLs dataset. The final classes **A**) CI-out-open1, **B**) CI-in-open1, **C**) CI-out-open2, and **D**) CI-in-open2 were inspected for the orientation distribution of the particles in the final consensus alignment using 3D angular and Mollweide plots. Equivalent data are shown in each case. The orientation distribution in the Mollweide plots is relative to the input reference volume, so the complex I 3D volumes (grey) in each case are shown in the 3D angular distribution spheres for reference. The assessment of uniformity of resolution in each direction (sphericity, where 1 is completely uniform) was performed by dividing the sphere up into 100 evenly sampled cones and calculating directional Fourier-shell correlations (FSCs) plotted as histograms, using the 3DFSC Program Suite v3.0. The 3DFSC global FSC curve is shown in black (± S.D. of directional FSCs).

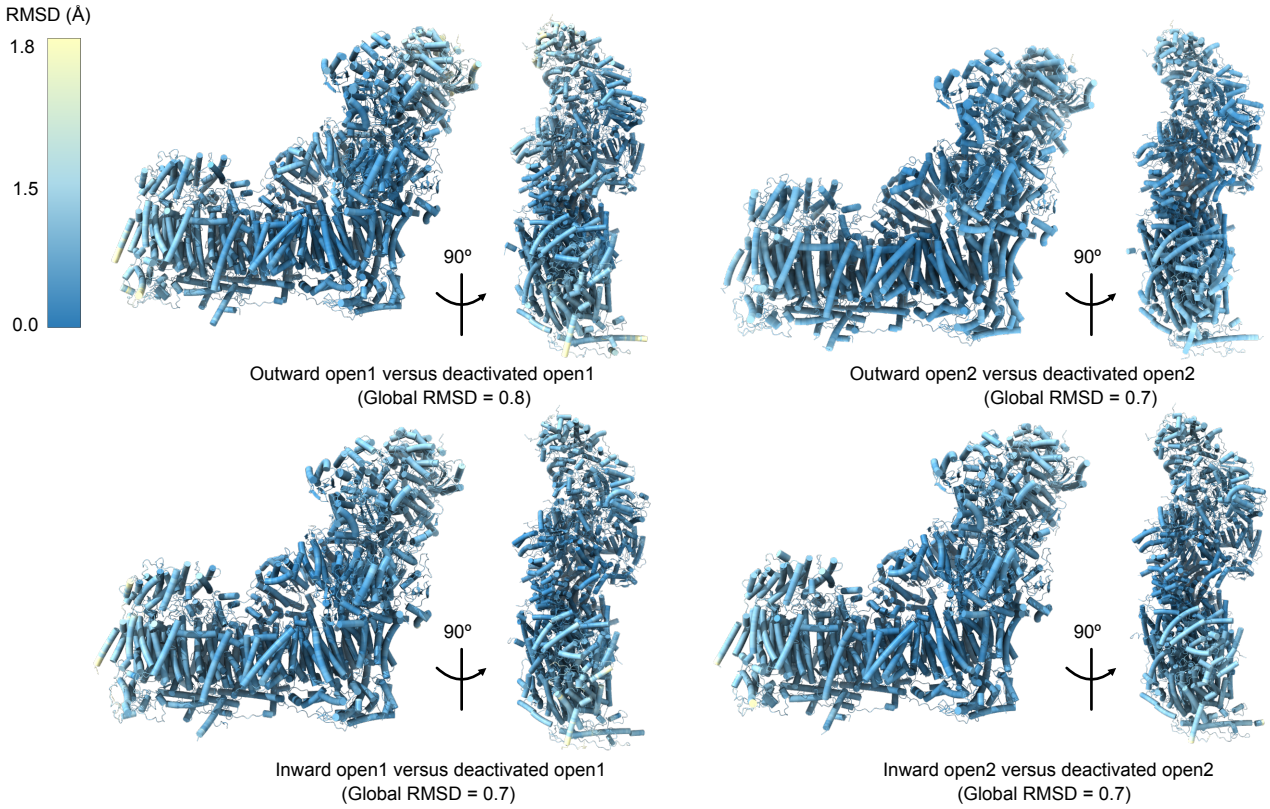


Fig. S18 | Global comparisons of the open1 and open2 states present in CI-PLs in the as-prepared and deactivated samples. Root-mean-square deviation (RMSD) values (Å) are shown for the outward- and inward-facing open1 and open2 states. The as-prepared CI-PLs models are used to display the values, according to the scale bar, and the values reported in the panel titles are the global values.

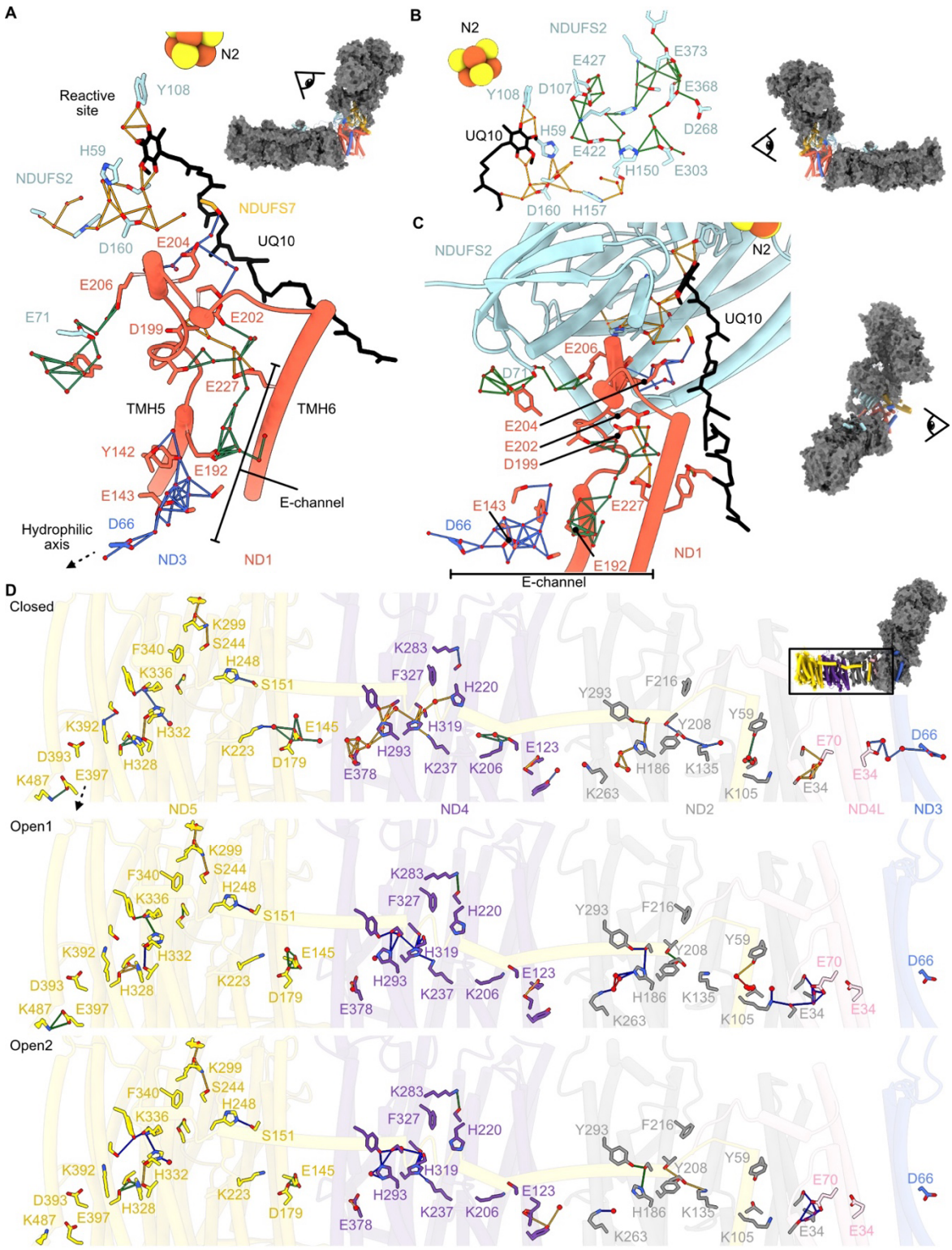


Fig. S19 | The Grotthuss networks of regions implicated in proton-transfer events. **A**) The Grotthuss networks (4 Å sidechain O/N distances) of Grotthuss-competent residues (D, E, H, K, S, Y), water molecules and the bound ubiquinone-10 (UQ10) are shown for the CI-out-closed state. Networks were detected in subunits ND1 (red), ND3 (dark blue), NDUFS2 (light blue) and NDUFS7 (gold), and colored by group with minor and distant networks discarded for clarity. TMH5–6^{ND1} are shown for context. The viewpoint is indicated by the inset complex I. **B**) Networks at the reactive site of UQ10 reduction and extending through subunit NDUFS2. **C**) An alternate view of the Grotthuss networks extending from the reaction site down to the hydrophilic axis (D66^{ND3}) via residues of the TMH5–6^{ND1} loop and E-channel. The acidic residues E206^{ND1}, E204^{ND1}, E202^{ND1}, E227^{ND1}, E192^{ND1} occupy positions where they may gate proton transfers between the observed networks. **D**) Grotthuss networks detected across the hydrophilic axis of the core transmembrane subunits ND3, ND4L, ND2, ND4 and ND5, with networks outside of the key residues shown removed for clarity. The apparent connectivity across the hydrophilic axis is likely due to the modest resolution in the membrane arm limiting the number of water molecules modelled. The output cavity in ND5 is indicated with a black arrow. The same analysis was performed for CI-out-open1and CI-out-open2 states.

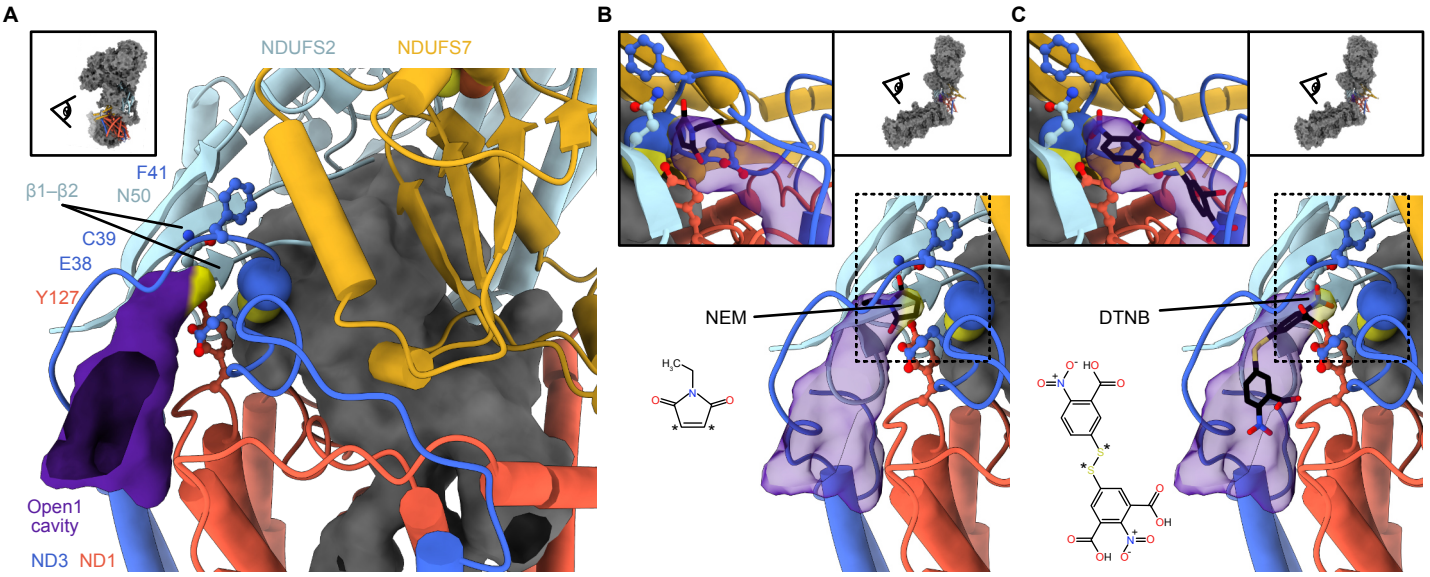


Fig. S20 | The matrix-accessible cavity in the open1 state. **A**) The transition of the closed state into the open1 state rotates the hydrophilic domain, shifting the β1–β2 hairpin loop away from the membrane domain ND3 loop and generating a matrix solvent-accessible cavity (purple surface) that has access (yellow patch) to ND3-Cys39 (spheres). The residues that constrict the solvent-accessible site (ND1-Y127, ND3-E38, C39, F41 and NDUFS2-N50) are shown as ball and stick and labelled [ND1 (red), ND3 (dark blue), NDUFS2 (light blue) and NDUFS7 (gold)]. The sealed-from-the-matrix ubiquinone-10 cavity is shown as a grey surface. Inset shows the viewpoint. **B**) *N*-ethylmaleimide (NEM) undergoes an alkylation reaction with the thiol group on cysteines to form a covalent bond with either of its reactive carbons (indicated with *). NEM is shown docked (placed using Coot and allowed to refine, with the protein conformation maintained, to minimise steric clashing) into the open1 cavity close to the ND3-C39 residue that is known to react with NEM. Upper inset shows the same docked conformation viewed from the opposite side. **C**) 5,5′-dithiobis-(2-nitrobenzoic acid) (DTNB) is reduced by thiol groups on cysteines at either of its sulfur atoms in its disulfide bridge (indicated with *) to generate a new disulfide bond (ejecting a 2-nitro-5-thiobenzoate anion), covalently linking it to the protein. DTNB is shown docked (placed using Coot and allowed to refine, with the protein conformation maintained, to minimise steric clashing) into the open1 cavity close to ND3-C39, which is known to react with DTNB. Upper inset shows the same docked conformation viewed from the opposite side. The reactive disulfide bridge of DTNB is not close enough to react directly with ND3-C39 so minor adjustments, such as the displacement of ND3-F41 on the loop, are necessary to allow the required proximity.

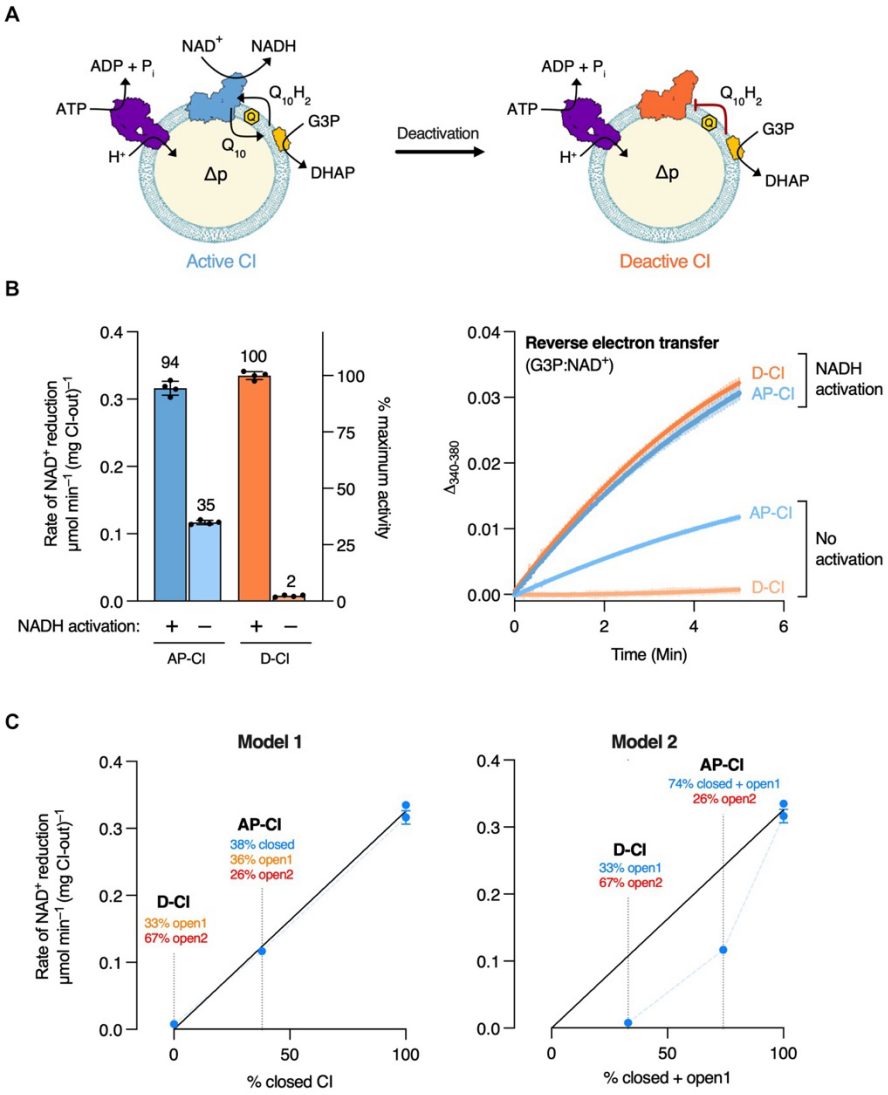


Fig. S21 | Assessment of the biochemical state of complex I in proteoliposomes by reverse electron transfer. A) Schematic representation of co-reconstituted ATPase-CI-PLs for reverse electron transfer. The PLs are supplemented with glycerol 3-phosphate dehydrogenase (GlpD) to reduce the UQ10 pool (the oxidized and reduced states are denoted Q_{10} and $Q_{10}H_2$, respectively), and the proton-motive force (Δp) is generated by ATP hydrolysis. In the active state CI catalyzes RET (observed as reduction of NAD^+ to NADH), while in the deactive state it is incapable of RET catalysis. **B)** NAD^+ reduction by as-prepared (AP) and deactivated (D) ATPase-CI-PLs. Samples pre-activated by addition of NADH are indicated (see methods for the activation procedure). The rates of catalysis, relative to the maximum observed activity, are given alongside the assay traces for NAD^+ reduction ($n = 4$). The rate of NADH oxidation for forward catalysis by the same sample of co-reconstituted proteoliposomes was 18.5 μmol min^{-1} (mg CI_{out})$^{-1}$. **C)** Correlation of the proportions of structural states observed by cryoEM to experimentally determined rates of NAD^+ reduction. Model 1 assumes that only CI-closed is able to catalyze RET; Model 2 assumes that both CI-closed and CI-open1 are able to catalyze RET.

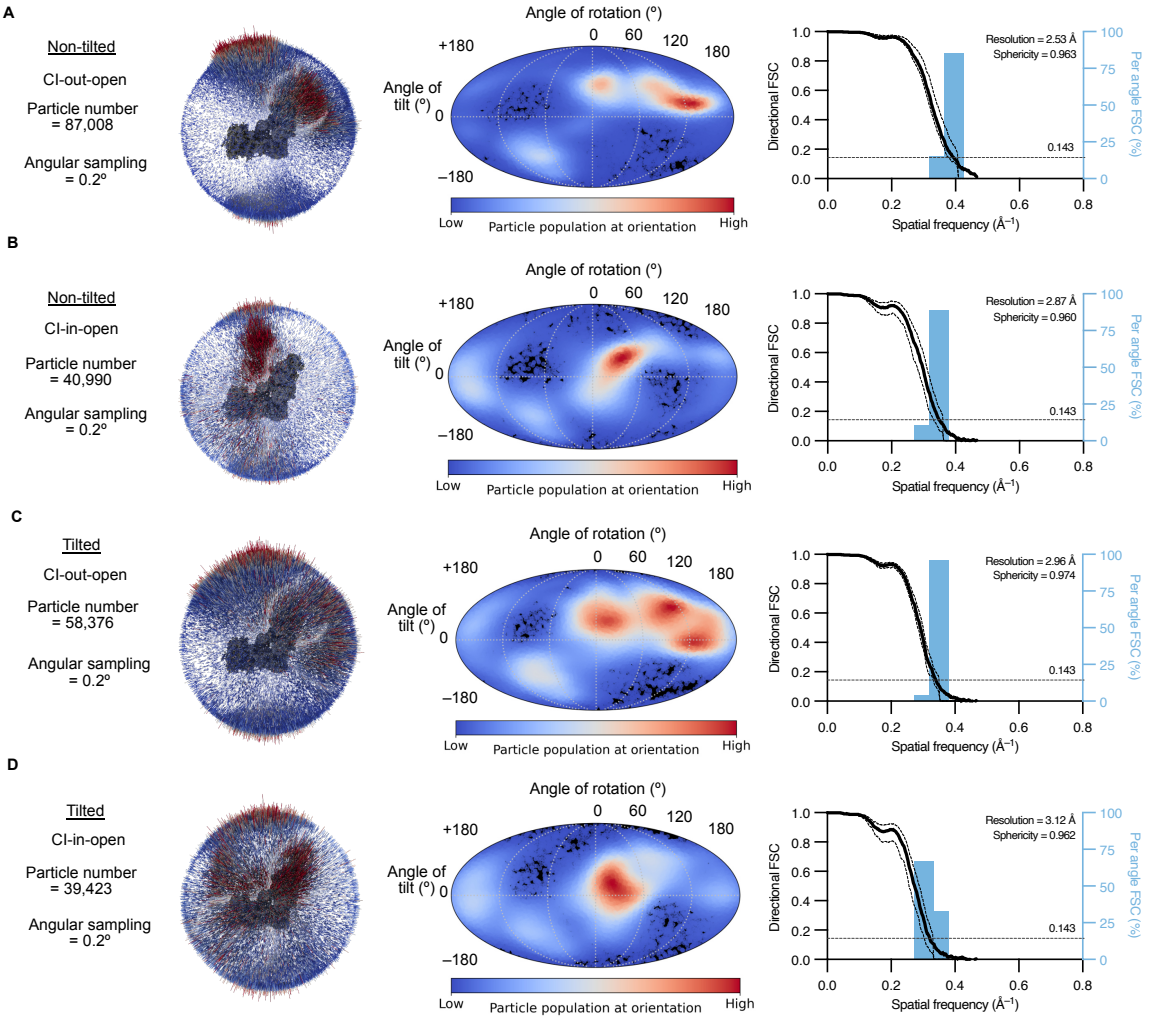


Fig. S22 | Orientation analyses of the consensus classes of the separately processed non-tilted and tilted deactivated CI-PLs datasets. The final classes for the non-tilted **A**) CI-out-open, **B**) CI-in-open classes, and the tilted **C**) CI-out-open, and **D**) CI-in-open classes were inspected for the orientation distribution of the particles in the final consensus alignment using 3D angular and Mollweide plots. Equivalent data are shown in each case. Note, at this stage the open1 and open2 states had not been separated and so are presented as a single open class here. The orientation distribution in the Mollweide plots is relative to the input reference volume, so the complex I 3D volumes (grey) in each case are shown in the 3D angular distribution spheres for reference. The assessment of uniformity of resolution in each direction (sphericity, where 1 is completely uniform) was performed by dividing the sphere up into 100 evenly sampled cones and calculating directional Fourier-shell correlations (FSCs) plotted as histograms, using the 3DFSC Program Suite v3.0. The 3DFSC global FSC is shown in black (± S.D. of directional FSCs). The tilted dataset shows increased orientation distribution relative to the non-tilted dataset, however its overall resolution suffers, likely due to the relatively thicker ice and contrast transfer function (CTF) gradient (even with per-particle CTF refinement performed across the micrographs for the tilted grid), as well as increased beam-induced motion. The data presented suggest the level of preferred orientation in the non-tilted dataset does not substantially impact the consensus map, given the number of particles obtained. However, it may negatively impact a reconstruction preformed using a lower number of micrographs/particles.

Table S1 | CryoEM data collection, refinement and validation statistics for the CI-PLs dataset.

	CI-PLs dataset (purified in LMNG, as-prepared)					
Data collection and processing						
Nominal magnification	81,000					
Voltage (kV)	300					
Electron exposure (e^{-} Å^{-2})	45					
Targeted defocus range (μm)	-0.9 to -2.3					
Calibrated pixel size (Å)	1.066					
Symmetry imposed	*C*1					
EMPIAR code	EMPIAR-11678					
Initial particle images (no.)	5,688,318					
State and model (PDB/EMDB codes)	**CI-out-closed (8Q48/18141)**	**CI-out-open1 (8Q4A/18143)**	**CI-out-open2 (8Q49/18142)**	**CI-in-closed (8Q45/18138)**	**CI-in-open1 (8Q47/18140)**	**CI-in-open2 (8Q46/18139)**
Final particle images (no.)	183,021	175,986	127,085	63,569	30,701	133,884
Map resolution (Å) (FSC 0.143)	2.5	2.6	2.6	2.7	2.9	2.6
Map resolution range (Å)	2.3–5.5	2.3–5.6	2.4–6.6	2.5–5.8	2.6–6.6	2.3–5.3
Map sharpening (RELION) *B* factor (Å^2)	−27	−33	−33	−28	−28	−31
Refinement						
Initial model used	7QSK	7QSN	7QSN	7QSK	7QSN	7QSN
Model resolution (Å) (FSC 0.5)	2.6	2.7	2.8	2.7	2.9	2.7
Model composition						
Nonhydrogen atoms	71,834	70,996	70,056	71,363	70,199	68,995
Protein residues	8286	8272	8243	8293	8274	8243
Ligands	91	83	81	86	74	71
Waters	1122	953	732	n/a	n/a	n/a
B factors mean (Å^2)						
Protein	49.10	52.81	47.08	46.96	50.13	48.53
Ligand	48.65	52.44	50.51	48.77	51.10	49.69
Water	35.38	39.19	39.33	n/a	n/a	n/a
RMS deviations						
Bond lengths (Å)	0.003	0.004	0.003	0.002	0.004	0.004
Bond angles (°)	0.511	0.503	0.474	0.502	0.493	0.514
Validation						
MolProbity score	1.29	1.57	1.68	1.53	1.77	1.58
Clashscore	3.72	3.68	3.92	3.17	4.32	3.41
Rotamer outliers (%)	1.12	1.85	2.30	2.63	2.75	2.56
Cß outliers (%)	0.00	0.00	0.00	0.00	0.00	0.00
Ramachandran plot						
Favored (%)	97.57	96.73	96.50	97.47	96.54	97.24
Allowed (%)	2.42	3.26	3.47	2.53	3.42	2.72
Outliers (%)	0.01	0.01	0.02	0.00	0.04	0.04
Rama-Z (Ramachandran plot Z-score, RMSD)						
Whole	0.18 (0.09)	0.08 (0.10)	0.06 (0.10)	0.05 (0.10)	-0.35 (0.10)	-0.23 (0.09)
Helix	0.36 (0.08)	0.38 (0.08)	0.50 (0.08)	0.30 (0.08)	0.10 (0.08)	0.06 (0.08)
Sheet	0.03 (0.25)	-0.06 (0.25)	-0.29 (0.27)	-0.14 (0.26)	-0.33 (0.26)	-0.36 (0.26)
Loop	0.02 (0.11)	-0.18 (0.11)	-0.34 (0.11)	-0.10 (0.11)	-0.46 (0.11)	-0.20 (0.11)

Table S2 | Summary of modifications and cofactors of the model for CI-out-closed (PDB: 8Q48).

Subunit	Alternative names	Chain	Total residues	N-terminal modification	Modelled residues (%)	Modelled cofactors and modifications
NDUFV1	51 kDa, Nqo1, NuoF	F	444	Δ 1–20	7–438 (97.3)	FMN, 4Fe4S
NDUFV2	24 kDa, Nqo2, NuoE	E	217	Δ 1–32	4–217 (98.6)	2Fe2S
NDUFS1	75 kDa, Nqo3, NuoG	G	704	Δ 1–23	6–693 (97.7)	2Fe2S, 2 x 4Fe4S
NDUFS2	49 kDa, Nqo4, NuoC	D	430	Δ 1–33	1–430 (100)	Dimethyl-Arg85
NDUFS3	30 kDa, Nqo5, NuoC	C	228	Δ 1–38	6–214 (91.6)	
NDUFS7	PSST, Nqo6, NuoB	B	179	Δ 1–37	25–179 (86.6)	4Fe4S
NDUFS8	TYKY, Nqo9, NuoI	I	176	Δ 1–36	1–176 (100)	2 x 4Fe4S
ND1	Nqo8, NuoH	H	318	N-formyl	1–318 (100)	N-formyl
ND2	Nqo14, NuoN	N	347	N-formyl	1–347 (100)	N-formyl
ND3	Nqo7, NuoA	A	115	N-formyl	1–115 (100)	N-formyl
ND4	Nqo13, NuoM	M	459	N-formyl	1–459 (100)	N-formyl
ND4L	Nqo11, NuoK	K	98	N-formyl	1–98 (100)	N-formyl
ND5	Nqo12, NuoL	L	606	N-formyl	1–606 (100)	N-formyl
ND6	Nqo10, NuoJ	J	175	N-formyl	1–175 (100)	N-formyl
NDUFV3	10 kDa	s	75	Δ 1–34	31–75 (60.0)	
NDUFS4	18 kDa	Q	133	Δ 1–42	5–133 (97.0)	
NDUFS5	15 kDa	e	105	–Met	1–99 (94.3)	2 x Cys–Cys
NDUFS6	13 kDa	R	96	Δ 1–28	1–96 (100)	Zn^{2+}
NDUFA1	MWFE	a	70	–	1–70 (100)	
NDUFA2	B8	S	98	–Met +Ac	12–98 (88.8)	
NDUFA3	B9	b	83	–Met +Ac	1–83 (100)	N-acetyl
NDUFA5	B13	V	115	–Met +Ac	1–115 (99.1)	
NDUFA6	B14	W	127	–Met +Ac	13–127 (90.6)	
NDUFA7	B14.5a	r	112	–Met +Ac	1–72, 90–112 (84.8)	N-acetyl
NDUFA8	PGIV	X	171	–Met	1–171 (100)	
NDUFA9	39 kDa	P	345	Δ 1–35	1–342 (99.1)	NADPH
NDUFA10	42 kDa	O	320	Δ 1–23	1–320 (100)	Mg^{2+}–dGTP
NDUFA11	B14.7	Y	140	–Met +Ac	1–140 (100)	2 x Cys–Cys, N-acetyl
NDUFA12	B17.2	q	145	+Ac	1–145 (100)	N-acetyl
NDUFA13	B16.6	Z	143	–Met +Ac	3–143 (98.6)	
NDUFAB1α	SDAPα	T	88	Δ 1–46	1–88 (100)	4'-phosphopantethine + 3-hydroxytetradecanoate
NDUFAB1β	SDAPβ	U				
NDUFB1	MNLL	f	57	–Met	1–57 (100)	
NDUFB2	AGGG	j	72	Δ 1–36	1–71 (98.6)	
NDUFB3	B12	k	97	–Met +Ac partial	1–81 (83.5)	
NDUFB4	B15	m	128	–Met +Ac	1–128 (100)	N-acetyl
NDUFB5	SGDH	h	143	Δ 1–46	6–143 (96.5)	
NDUFB6	B17	i	127	–Met +Ac	1–127 (100)	N-acetyl
NDUFB7	B18	o	136	–Met +Myr	1–122 (89.7)	N-myristoyl
NDUFB8	ASHI	l	158	Δ 1–28	3–158 (98.7)	
NDUFB9	B22	n	178	–Met +Ac	8–178 (96.1)	
NDUFB10	PDSW	p	175	–Met	2–175 (99.4)	
NDUFB11	ESSS	g	125	Δ 1–29	22–122 (80.8)	
NDUFC1	KFYI	c	49	Δ 1–27	1–49 (100)	
NDUFC2	B14.5b	d	120	+Ac partial	1–120 (100)	N-acetyl

Table S3 | CryoEM data collection, refinement and validation statistics for the DDM-CI-PLs dataset.

	DDM-CI-PLs dataset (purified in DDM, as-prepared)					
Data collection and processing						
Nominal magnification	81,000					
Voltage (kV)	300					
Electron exposure (e^{-} Å^{-2})	40					
Targeted defocus range (μm)	-1.0 to -3.0					
Calibrated pixel size (Å)	1.35					
Symmetry imposed	*C*1					
EMPIAR code	EMPIAR-11638					
Initial particle images (no.)	2,313,863					
State and model (PDB/EMDB codes)	**CI-out-closed (8Q0M/18055)**	**CI-out-open2 (8Q0O/18057)**	**CI-out-slack (8Q0Q/18059)**	**CI-in-closed (8Q0A/18051)**	**CI-in-open2 (8Q0F/18052)**	**CI-in-slack (8Q0J/18054)**
Final particle images (no.)	81,459	123,011	45,544	68,095	116,474	45,661
Map resolution (Å) (FSC 0.143)	3.1	3.1	3.6	3.1	3.1	3.8
Map resolution range (Å)	2.9–6.6	2.9–6.4	3.2–9.3	2.8–6.6	2.9–6.6	3.4–9.8
Map sharpening (RELION) *B* factor (Å^2)	−41	−49	−53	−35	−49	−52
Refinement						
Initial model used	8Q48	8Q49	7QSO	8Q45	8Q46	7QSO
Model resolution (Å) (FSC 0.5)	3.1	3.2	3.6	3.1	3.2	3.8
Model composition						
Nonhydrogen atoms	71,676	70,323	65,867	70,959	70,023	65,999
Protein residues	8286	8243	8004	8286	8243	8004
Ligands	88	77	37	80	68	37
Waters	n/a	n/a	n/a	n/a	n/a	n/a
B factors mean (Å^2)						
Protein	54.80	48.26	83.22	52.04	56.43	93.64
Ligand	55.45	46.54	80.27	52.81	55.50	87.57
Water	n/a	n/a	n/a	n/a	n/a	n/a
RMS deviations						
Bond lengths (Å)	0.003	0.004	0.005	0.005	0.003	0.004
Bond angles (°)	0.491	0.505	0.528	0.517	0.486	0.496
Validation						
MolProbity score	1.41	1.83	2.15	1.70	1.76	2.20
Clashscore	3.46	4.43	8.21	3.64	4.18	8.58
Rotamer outliers (%)	1.50	2.60	2.28	2.41	2.69	2.49
Cß outliers (%)	0.00	0.00	0.00	0.00	0.00	0.00
Ramachandran plot						
Favored (%)	97.27	95.72	93.37	96.23	96.42	93.30
Allowed (%)	2.71	4.25	6.62	3.75	3.53	6.64
Outliers (%)	0.01	0.04	0.01	0.01	0.05	0.05
Rama-Z (Ramachandran plot Z-score, RMSD)						
Whole	0.44 (0.10)	-0.43 (0.09)	-0.93 (0.09)	-0.11 (0.09)	-0.03 (0.10)	-0.75 (0.10)
Helix	0.69 (0.08)	0.12 (0.08)	-0.23 (0.08)	0.26 (0.08)	0.38 (0.08)	0.01 (0.09)
Sheet	-0.10 (0.26)	-0.67 (0.27)	-0.92 (0.29)	-0.53 (0.25)	-0.70 (0.27)	-1.29 (0.27)
Loop	0.00 (0.11)	-0.61 (0.11)	-0.89 (0.10)	-0.26 (0.11)	-0.28 (0.11)	-0.84 (0.10)

Table S4 | CryoEM data collection for the deactivated tilted and non-tilted CI-PLs datasets, and the refinement and validation statistics for the four states from the combined deactivated CI-PLs dataset.

	Deactivated CI-PLs dataset (non-tilted)		Deactivated CI-PLs dataset (tilted 20°)	
Data collection and processing				
Nominal magnification	81,000		81,000	
Voltage (kV)	300		300	
Electron exposure (e^{-} Å^{-2})	40		40	
Targeted defocus range (μm)	-0.9 to -2.3		-0.8 to -2.0	
Calibrated pixel size (Å)	1.072		1.072	
Symmetry imposed	*C*1		*C*1	
EMPIAR code	EMPIAR-11637		EMPIAR-11636	
Initial particle images (no.)	932,186		878,425	
	CI-out-open1	**CI-out-open2**	**CI-in-open1**	**CI-in-open2**
PDB/EMDB codes (combined datasets)	**8Q25/18069**	**8Q1Y/18068**	**8Q1U/18067**	**8Q1P/18066**
Final particle images (no.)	45,912	93,255	14,905	58,386
Map resolution (Å) (FSC 0.143)	2.8	2.6	3.3	2.9
Map resolution range (Å)	2.4–7.2	2.3–6.7	2.9–8.2	2.5–6.5
Map sharpening (RELION) *B* factor (Å^2)	−26	−25	−36	−33
Refinement				
Initial model used	8Q4A	8Q49	8Q47	8Q46
Model resolution (Å) (FSC 0.5)	2.8	2.7	3.2	2.9
Model composition				
Nonhydrogen atoms	70,996	70,571	70,058	70,162
Protein residues	8272	8243	8274	8243
Ligands	83	81	72	71
Waters	n/a	n/a	n/a	n/a
B factors mean (Å^2)				
Protein	56.54	45.47	48.11	50.13
Ligand	55.07	50.32	51.69	53.24
Water	n/a	n/a	n/a	n/a
RMS deviations				
Bond lengths (Å)	0.003	0.004	0.004	0.003
Bond angles (°)	0.507	0.477	0.500	0.475
Validation				
MolProbity score	1.54	1.58	1.84	1.54
Clashscore	3.40	3.11	4.31	3.06
Rotamer outliers (%)	2.01	2.52	2.61	2.55
Cß outliers (%)	0.00	0.00	0.00	0.00
Ramachandran plot				
Favored (%)	97.00	97.00	95.51	97.32
Allowed (%)	2.99	2.99	4.45	2.66
Outliers (%)	0.01	0.01	0.04	0.02
Rama-Z (Ramachandran plot Z-score, RMSD)				
Whole	-0.48 (0.09)	-0.16 (0.09)	-0.58 (0.09)	-0.10 (0.09)
Helix	-0.09 (0.08)	0.26 (0.08)	0.04 (0.08)	0.20 (0.08)
Sheet	-0.67 (0.25)	-0.18 (0.27)	-0.69 (0.27)	-0.08 (0.27)
Loop	-0.36 (0.11)	-0.40 (0.11)	-0.73 (0.10)	-0.23 (0.11)

Table S5. The status of structural features that differ between the closed and open states in mammalian complex I presented for models of complex I from *Bos taurus* determined here. The 'active' (A) and 'deactive' (D) indicators used are related to those described for the resting active (PDB 7QSK) and deactive (PDB 7QSN) states of bovine complex I in nanodiscs. The nanodisc slack state (7QSO) is included for reference. **ND6-TMH3:** A, α-helical or D, π-bulge at F68/Y70. **ND3 TMH1–2**, **ND1 TMH5–6 and NDUFS2 β1–β2 loops:** A, ordered in active nanodisc conformation; A-like, A with only minor differences; Alt, ordered but in a noticeably alternate backbone conformation; D-like, β-strands in NDUFS2 ordered but loop disordered; D, disordered. **ND1 TMH4:** A, bent helix with Y127-Cα in the A position; D, straight helix with Y127-Cα in the deactive nanodisc position. **NDUFS7 Arg77 loop:** A, Arg pointing away from NDUFS2 and an adjacent loop; Mixed, Arg pointing away from NDUFS2 but an adjacent β-strand; D, Arg pointing towards NDUFS2 and an adjacent β-strand.

Preparation and state name	PDB/ EMDB	Resolution	NDUFA5/10 interface (Å^2) [residues buried]	ND6 TMH3	ND3 TMH1–2 loop	ND1 TMH 5–6 loop	ND1 TMH4	NDUFS2 β1–β2 loop	NDUFS7 Arg77 loop
CI-out-closed	8Q48/ 18141	2.5	361 [20]	A	A	A	A	A	A
CI-in-closed	8Q45/ 18138	2.7	393 [20]	A	A	A	A	A	A
CI-out-open1	8Q4A/ 18143	2.6	127 [14]	D	Alt	A-like	D	D-like	D
CI-in-open1	8Q47/ 18140	2.9	163 [15]	D	Alt	A-like	D	D-like	D
CI-out-open2	8Q49/ 18142	2.6	126 [9]	D	D	A-like	D	D-like	D
CI-in-open2	8Q46/ 18139	2.6	158 [15]	D	D	A-like	D	D-like	D
DDM CI-out-closed	8Q0M/ 18055	3.1	301 [18]	A	A	A	A	A	A
DDM CI-in-closed	8Q0A/ 18051	3.1	338 [17]	A	A	A	A	A	A
DDM CI-out-open2	8Q0O/ 18057	3.1	119 [8]	D	D	A-like	D	D-like	D
DDM CI-in-open2	8Q0F/ 18052	3.1	156 [14]	D	D	A-like	D	D-like	D
DDM CI-out-slack	8Q0Q/ 18059	3.6	76 [8]	D	D	Alt	D	Alt	Mixed
DDM CI-in-slack	8Q0J/ 18054	3.8	96 [7]	D	D	Alt	D	Alt	Mixed
Deactivated CI-out-open1	8Q25/ 18069	2.8	80 [7]	D	Alt	A-like	D	D-like	D
Deactivated CI-in-open1	8Q1U/ 18067	3.3	168 [15]	D	Alt	A-like	D	D-like	D
Deactivated CI-out-open2	8Q1Y/ 18068	2.6	124 [9]	D	D	A-like	D	D-like	D
Deactivated CI-in-open2	8Q1P/ 18066	2.9	154 [15]	D	D	A-like	D	D-like	D
Nanodisc CI-closed	7QSK/ 14132	2.8	354 [19]	A	A	A	A	A	A
Nanodisc CI-open	7QSN/ 14139	2.8	129 [9]	D	D	D	D	D	D
Nanodisc CI-slack	7QSO/ 14140	3.0	99 [10]	D	D	Alt	D	Alt	Mixed

References

57. G. Daum, Lipids of mitochondria. *Biochim. Biophys. Acta* **822**, 1–42 (1985).

58. M. S. Sharpley, R. J. Shannon, F. Draghi, J. Hirst, Interactions between phospholipids and NADH:ubiquinone oxidoreductase (complex I) from bovine mitochondria. *Biochemistry* **45**, 241–8 (2006).

59. K. Naydenova, C. J. Russo, Measuring the effects of particle orientation to improve the efficiency of electron cryomicroscopy. *Nat. Commun.* **8**, 8–12 (2017).

60. D. Kimanius, L. Dong, G. Sharov, T. Nakane, S. H. W. Scheres, New tools for automated cryo-EM single-particle analysis in RELION-4.0. *Biochem. J.* **478**, 4169–4185 (2021).

61. A. Punjani, J. L. Rubinstein, D. J. Fleet, M. A. Brubaker, CryoSPARC: Algorithms for rapid unsupervised cryo-EM structure determination. *Nat. Methods* **14**, 290–296 (2017).

62. J. Zivanov, T. Nakane, S. H. W. Scheres, A Bayesian approach to beam-induced motion correction in cryo-EM single-particle analysis. *IUCrJ* **6**, 5–17 (2019).

63. S. Q. Zheng, E. Palovcak, J. P. Armache, K. A. Verba, Y. Cheng, D. A. Agard, MotionCor2: Anisotropic correction of beam-induced motion for improved cryo-electron microscopy. *Nat. Methods* **14**, 331–332 (2017).

64. A. Rohou, N. Grigorieff, CTFFIND4: Fast and accurate defocus estimation from electron micrographs. *J. Struct. Biol.* **192**, 216–221 (2015).

65. D. Tegunov, P. Cramer, Real-time cryo-electron microscopy data preprocessing with Warp. *Nat. Methods* **16**, 1146–1152 (2019).

66. T. Bepler, A. Morin, M. Rapp, J. Brasch, L. Shapiro, A. J. Noble, B. Berger, Positive-unlabeled convolutional neural networks for particle picking in cryo-electron micrographs. *Nat. Methods* **16**, 1153–1160 (2019).

67. D. Asarnow, E. Palovcak, Y. Cheng, asarnow/pyem: UCSF pyem v0.5. Zenodo (2019). https://doi.org/https://doi.org/10.5281/zenodo.3576630.

68. T. D. Goddard, C. C. Huang, E. C. Meng, E. F. Pettersen, G. S. Couch, J. H. Morris, T. E. Ferrin, UCSF ChimeraX: Meeting modern challenges in visualization and analysis. *Protein Sci.* **27**, 14–25 (2018).

69. P. B. Rosenthal, R. Henderson, Optimal determination of particle orientation, absolute hand, and contrast loss in single-particle electron cryomicroscopy. *J. Mol. Biol.* **333**, 721–745 (2003).

70. J. L. Vilas, J. Gómez-Blanco, P. Conesa, R. Melero, J. Miguel de la Rosa-Trevín, J. Otón, J. Cuenca, R. Marabini, J. M. Carazo, J. Vargas, C. O. S. Sorzano, MonoRes: Automatic and Accurate Estimation of Local Resolution for Electron Microscopy Maps. *Structure* **26**, 337-344.e4 (2018).

71. E. Ramírez-Aportela, J. L. Vilas, A. Glukhova, R. Melero, P. Conesa, M. Martínez, D. Maluenda, J. Mota, A. Jiménez, J. Vargas, R. Marabini, P. M. Sexton, J. M. Carazo, C. O. S. Sorzano, Automatic local resolution-based sharpening of cryo-EM maps. *Bioinformatics* **36**, 765–772 (2020).

72. J. M. de la Rosa-Trevín, A. Quintana, L. del Cano, A. Zaldívar, I. Foche, J. Gutiérrez, J. Gómez-Blanco, J. Burguet-Castell, J. Cuenca-Alba, V. Abrishami, J. Vargas, J. Otón, G. Sharov, J. L. Vilas, J. Navas, P. Conesa, M. Kazemi, R. Marabini, C. O. S. Sorzano, J. M. Carazo, Scipion: A software framework toward integration, reproducibility and validation in 3D electron microscopy. *J. Struct. Biol.* **195**, 93–99 (2016).

73. D. Liebschner, P. V. Afonine, M. L. Baker, G. Bunkoczi, V. B. Chen, T. I. Croll, B. Hintze, L. W. Hung, S. Jain, A. J. McCoy, N. W. Moriarty, R. D. Oeffner, B. K. Poon, M. G. Prisant, R. J. Read, J. S. Richardson, D. C. Richardson, M. D. Sammito, O. V. Sobolev, D. H. Stockwell, T. C. Terwilliger, A. G.

Urzhumtsev, L. L. Videau, C. J. Williams, P. D. Adams, Macromolecular structure determination using X-rays, neutrons and electrons: Recent developments in Phenix. *Acta Crystallogr. Sect. D Struct. Biol.* **75**, 861–877 (2019).

74. Y. Z. Tan, P. R. Baldwin, J. H. Davis, J. R. Williamson, C. S. Potter, B. Carragher, D. Lyumkis, Addressing preferred specimen orientation in single-particle cryo-EM through tilting. *Nat. Methods* **14**, 793–796 (2017).

75. J. Hirst, J. Carroll, I. M. Fearnley, R. J. Shannon, J. E. Walker, The nuclear encoded subunits of complex I from bovine heart mitochondria. *Biochim. Biophys. Acta Bioenerg.* **1604**, 135–150 (2003).

76. I. M. Fearnley, M. Finel, J. M. Skehel, J. E. Walker, NADH:ubiquinone oxidoreductase from bovine heart mitochondria. cDNA sequences of the import precursors of the nuclear-encoded 39 kDa and 42 kDa subunits. *Biochem. J.* **278**, 821–829 (1991).

77. J. Carroll, I. M. Fearnley, R. J. Shannon, J. Hirst, J. E. Walker, Analysis of the subunit composition of complex I from bovine heart mitochondria. *Mol. Cell Proteomics* **2**, 117–26 (2003).

78. D. Molina-Granada, E. González-Vioque, M. G. Dibley, R. Cabrera-Pérez, A. Vallbona-Garcia, J. Torres-Torronteras, L. A. Sazanov, M. T. Ryan, Y. Cámara, R. Martí, Most mitochondrial dGTP is tightly bound to respiratory complex I through the NDUFA10 subunit. *Commun. Biol.* **5** (2022).

79. P. Emsley, B. Lohkamp, W. G. Scott, K. Cowtan, Features and development of Coot. *Acta Crystallogr. Sect. D Struct. Biol.* **66**, 486–501 (2010).

80. C. J. Williams, J. J. Headd, N. W. Moriarty, M. G. Prisant, L. L. Videau, L. N. Deis, V. Verma, D. A. Keedy, B. J. Hintze, V. B. Chen, S. Jain, S. M. Lewis, W. B. Arendall, J. Snoeyink, P. D. Adams, S. C. Lovell, J. S. Richardson, D. C. Richardson, MolProbity: More and better reference data for improved all-atom structure validation. *Protein Sci.* **27**, 293–315 (2018).

Movie S1 | The structural transitions between the active/closed and deactive/open resting states. The 3D models for the closed, open1 and open2 states are used to describe the global and local transitions that occur as complex I deactivates. See also Fig. 4.